AN EXPERIMENTAL INVESTIGATION OF HYPERSONIC FLOW OVER BLUNT-NOSED BODIES AT A MACH NUMBER OF 5.8

Thesis by

Donald G. Fraasa

Lieutenant, U. S. Navy

In Partial Fulfillment of the Requirements

For the Degree of

Aeronautical Engineer

California Institute of Technology

Pasadena, California

1957

ACKNOWLEDGMENTS

The author wishes to express his sincere appreciation to Professor Lester Lees for his encouragement, guidance, and counsel as advisor during the course of this investigation.

The author also wishes to express his gratitude to the U. S. Navy (and will with six years of obligated duty) whose interest and support made this graduate study possible.

The many helpful suggestions and criticisms of Mr. James M. Kendall and Mr. Robert E. Oliver are gratefully acknowledged.

Sincere thanks are extended to Mr. C. A. Bartsch and the skillful staff of the GALCIT machine shop, particularly, Mr. George Carlson, who in constructing some of the models accomplished what the author thought impossible. Thanks, too, to Mr. Paul Baloga, Mr. Sam Roman, and the staff for their help and cooperation in operating the GALCIT hypersonic wind tunnel. The contributions of Mrs. G. Van Gieson to the preparation and completion of the manuscript are greatly appreciated.

Finally, the author thanks his dear, understanding wife for her patience, encouragement, and inspiration and for her attempt, though ofttimes in vain, to keep the children quiet.

ABSTRACT

An experimental investigation to obtain schlieren photographs of the flow over several blunt-nosed bodies and to determine the surface static pressure distribution on certain of these models was conducted in the GALCIT hypersonic wind tunnel, leg no. 1, at a nominal Mach number of 5.8 and a free stream Reynolds number per inch of 2.22×10^5.

Schlieren photographs were made of the following blunt-nosed models, all with cylindrical afterbodies, at angles of yaw of 0, 4, and 8 degrees: a family of nine round-nosed bodies with nose radii of curvature varying from the radius of the afterbody cylinder (hemispherical nose) to infinity (flat nose), two concave-nosed bodies having nose radii of curvature equal to 0.8 and 1.6 times the afterbody diameter, and three flat-nosed cylinders with rounded shoulders whose radii of curvature were .083, .125, and .208 times the afterbody diameter.

Static pressure distributions at angles of yaw of 0, 4, and 8 degrees were determined for three of the blunt bodies: (1) the flat-nosed cylinder with infinite nose radius of curvature, (2) the flat-nosed cylinder with a rounded shoulder of radius equal to .208 of the afterbody diameter, and (3) a round-nosed cylinder with nose radius of curvature equal to 1.3 times the afterbody diameter.

The schlieren photographs were analyzed on a contour projector to measure shock standoff distances, to determine the sonic point on the shock, and to observe shock shape. Data derived from these studies and the pressure distributions are presented in graphical form. Comparisons are made between the experimental results and appropriate theoretical approximations for hypersonic flow.

TABLE OF CONTENTS

LIST OF FIGURES

LIST OF SYMBOLS

C_p	pressure coefficient, dimensionless, $(p-p_\infty)/(\frac{1}{2} \rho_\infty U_\infty^2)$
D	diameter of cylindrical afterbody, inches
h	rise, or maximum height, of nose spherical segment on model measured perpendicular to flat side of spherical segment
k	density ratio across normal shock, dimensionless, ρ_1/ρ_2
M	Mach number, dimensionless
p	pressure, lb./sq. in.
R	radius of curvature of rounded nose, inches
r	shoulder radius, inches
S	distance measured along the surface of a body from the longitudinal axis outward to the shoulder then aft, inches
S*	distance measured outward along the surface of a body from the longitudinal axis to the sonic point, inches
U_∞	free stream velocity, ft./sec.
y	coordinate distance from longitudinal axis, inches
α	angle of attack or angle of yaw, degrees
δ_1	shock standoff distance at the longitudinal axis, inches
δ_2	distance from the sonic point on the shock (at which the velocity behind the shock is just sonic) to the nearest point on the body
η	angle between the free stream flow direction and the normal to the body surface
θ_*	inclination of the shock at the sonic point
ρ	density, slugs/ft.^{3}
ϕ	angle whose sine is the radius of the afterbody cylinder divided by the radius of curvature of the nose

Subscripts

$( )_1$ static conditions in front of shock wave

$( )_2$ static conditions behind shock wave

$( )_\infty$ free stream conditions

$( )_*$ related to sonic point

$( )_{max}$ maximum value of quantity

Superscripts

$( )'$ measured on schlieren photograph

I. INTRODUCTION

Flight at hypersonic speeds results in high recovery temperatures with deleterious effects on conventional structural materials. The aerodynamic heating problem is particularly critical in the case of the slender, sharp-nosed, streamlined body in high speed flight inasmuch as for this configuration the heat transfer rate at the pointed nose is high and there is insufficient nose volume for rapid conduction of heat away from the critical nose region or for heat removal apparatus. Thus the "thermal barrier" dictates a different configuration than the sharp nosed body for flight at hypersonic speed. The blunt-nosed body is the answer. At first this choice might seem illogical because of the sacrifice in aerodynamic performance caused by the increased drag on such a body. However, Eggers, Resnikoff, and Dennis (Ref. 1) show that for a fixed body length or body volume, the blunt-nosed shape produces minimum pressure foredrag.

Many theoretical analyses of hypersonic flow over blunt-nosed bodies appear in the literature but there seems to be a limited amount of experimental data with which to compare the theories. This investigation was initiated to provide such experimental data in the form of schlieren photographs showing shock shapes on blunt-nosed bodies, plots of shock parameters mensurable on the schlieren photographs, and detailed plots of pressure distribution on the nose portion of blunt-nosed bodies. In this study the experimental results are compared with theoretical results for shock wave geometry, and the experimental pressure distributions are compared with the appropriate hypersonic approximations.

The tests were conducted at a nominal Mach number of 5.8 in the GALCIT hypersonic wind tunnel, leg no. 1. The experimental phase of the investigation was carried out jointly with Eugene M. Wisenbaker, Lieutenant, U. S. Navy.

II. EQUIPMENT AND PROCEDURE

A. Description of the Wind Tunnel and Instrumentation

The tests were conducted in the GALCIT 5 x 5 inch hypersonic wind tunnel, which is a closed-return, continuously operating tunnel with achievable ranges of stagnation pressure from 14.7 to 95 psia and stagnation temperature from 70° to 300°F. The actual tests were made at a fixed reservoir temperature of 225°F and a fixed stagnation pressure of 74 psi gauge, giving a nominal test section Mach number of 5.8 and a Reynolds number per inch of 2.22×10^{5}. A silica-gel dryer is used for water removal whereas Cyclone separators and fiber glass filters are used for oil removal in the tunnel. Thirteen rotary vane-type positive displacement compressors and three reciprocating piston type compressors drive the tunnel. The tunnel is equipped with a schlieren system and a facility for photographing the observed phenomenon. Two 32-tube vacuum-referenced manometers were used to measure static pressures on the models, one manometer using mercury, and the other using silicone fluid. A schematic diagram of the wind tunnel and the compressor plant is shown in Figure 1, and the test section, with a side plate removed, is shown in Figure 2. The wind tunnel installation and the associated instrumentation are described in detail in Reference 2.

B. Description of the Models

The family of fourteen brass "dummy" models used in the schlieren study are shown in Figure 3. Nine of the models (A through J) were designed with standard cylindrical afterbodies (D = 1.5 inches)

and with convex blunt noses whose radii of curvature varied from $R/D = \infty$ for the flat-nosed body to $R/D = 0.5$ for the spherical-nosed body. Two dummy models (M and N) with concave blunt noses were constructed for the schlieren study. It was necessary to reduce the diameter of the cylindrical afterbodies of these concave-nosed models to 1.25 inches in order to establish flow with either of the models installed in the test section of the tunnel. The remaining three "dummy" models (J, K, and L) used in the schlieren study were flat-nosed with standard cylindrical afterbodies and varying shoulder radii of curvature of 0.083, 0.125, and 0.208 times the afterbody diameter. The general dimensions of all these dummy schlieren models are given in Figures 4 and 5.

For the second phase of the investigation three brass pressure models were constructed; the flat-nosed, the flat-nosed with shoulder radius of curvature equal to 0.208D, and the rounded nose with nose radius of curvature equal to 1.3D. All of the pressure models had the standard cylindrical afterbody. Figure 6 is a photograph of the pressure models and the general dimensions of the pressure models are given in Figure 7.

Static pressure orifices were located on the face and on the cylindrical afterbody just beyond the shoulder of the pressure bodies on rays separated by 60° as shown in Figure 7. The .016" diameter orifices were drilled normal to the surface to intersect larger channels drilled through from the rear of the cylindrical afterbody. Figure 8 is a cutaway view of the model showing these internal passages. Into each hole in the rear of the model was brazed a short length of stainless steel tubing to which was attached a length of flexible saran

plastic tubing to connect to the manometers.

C. Mounting of Models

The method of mounting the models in the wind tunnel is shown in Figure 2. The models were mounted on a short sting which was supported by two vertical struts extending through the top of the test section. Differential movement of the two vertical struts by means of external controls permitted precise control and variation of the angle of yaw of the model while maintaining the nose of the model at the tunnel centerline. Since all the models are axially symmetric, the terms angle of yaw and angle of attack are used interchangeably in this discussion. The nose of each "dummy" schlieren model was located $22\frac{1}{2}$ inches downstream of the tunnel throat. To allow the pressure models to be rotated about their axes, these models were attached to the sting by means of an intermediate shaft and sleeve with a set screw to lock the models in any desired rotational position (Figure 8). The nose of each pressure model was located $21\frac{1}{2}$ inches downstream of the tunnel throat owing to the added length of the sleeve. In either location the models were within the region of most uniform flow conditions as determined by a previously conducted pressure calibration survey. The plastic pressure leads were bound closely to the sting and closely together for some distance downstream before being led out of the tunnel to the manometers through "O" ring seals in a side port.

D. Test Procedure

Schlieren photographs were made of all the dummy models at angles of attack of 0, 4, and 8 degrees and of models E and I also at angles of attack of 12 and 16 degrees (Figures 9 - 53). All schlieren photographs were taken with knife edge vertical on Kodak Panatomic-X film using an aperture of f 11.0 and a shutter speed of 1/25th second. Each model was first positioned accurately on the tunnel axis at zero yaw. The tunnel was operated long enough to stabilize tunnel conditions before any photographs were taken. After the initial photograph at zero yaw, the angle of yaw was altered by the external controls and the photographs at an angle of attack were made in rapid succession without any need for shutting down the tunnel.

Static pressure measurements were made on pressure models of E, I, and L at angles of yaw of 0, 4, and 8 degrees at a reservoir pressure of 74 psi (gauge) and a reservoir temperature of 225°F corresponding to a free stream Mach number of 5.8. After each of the pressure models was positioned in the tunnel at zero yaw the pressure leads were connected to the manometers and the system checked for leaks. Before taking any pressure data the tunnel was operated for at least one hour to allow equilibrium temperatures to be reached throughout the wind tunnel and the compressor plant. It was desired to obtain pressure measurements for vertical and horizontal meridional planes, and also for diagonal planes designated as the 030° - 210° or 330° - 150° planes and the 060° - 240° or 300° - 120° planes. Since rotating the models required opening up the tunnel, and changing the angle of attack could be done externally, it was most efficient to

obtain the required pressure data by rotating the pressure bodies through 180° in 30° increments, each time taking readings with the model yawed first above and then below the free stream direction at the desired angles of attack.

The precise measurements required in analyzing the schlieren photographs were made on a Kodak contour projector at a magnification of ten. With the comparator it was possible to measure lengths to the nearest .0001 inch and angles to the nearest 0.1 minute. The following parameters were measured from the photographs: δ_1', the shock standoff distance; δ_2', the distance from the sonic point on the shock to the nearest point on the body; and D', the diameter of the cylindrical afterbody. The cylindrical afterbody diameter was measured to establish the scale ratio between the schlieren photographs and the actual models. The angle corresponding to the slope of the shock at the sonic point, θ^*, has a value of $66^{\circ}25'$ for a Mach number of 5.8.

The effect of Reynolds number variation was not investigated inasmuch as O'Bryant and Machell in Reference 3 found that under similar conditions there was no noticeable effect of Reynolds number on the pressure distributions over the range of Reynolds number per inch from $.97 \times 10^5$ to 2.38×10^5.

Throughout this investigation, in order to produce non-dimensional plots, all lengths have been divided by D or S* and pressure coefficients have been divided by $C_{p_{max}}$.

All numerical values used in the computations were obtained from Equations, Tables, and Charts for Compressible Flow, Report 1135 (Ref. 4).

III. RESULTS AND DISCUSSION

A. Schlieren Study

The schlieren photographs of the flow over each of the fourteen dummy models at 0, 4, and 8 degrees angle of attack and, in the case of Models E and I, also at 12 and 16 degrees angle of yaw, are shown in Figures 9 through 53. The free stream conditions for all these observations corresponded to a Mach number of 5.8 and a Reynolds number per inch of 2.22×10^5. A detached shock wave was produced on all the models. The flow behind the shock wave consists of subsonic, sonic, and supersonic flow regions. As is typical of hypersonic flow, the shock waves lie close to the body surface along the blunt noses. Comparing the shock shapes in Figures 9 through 17, it is observed that for the more flat-nosed bodies the horizontal distance between the shock and the body decreases with increase in the radial distance from the axis of symmetry, whereas for the more spherical-nosed bodies the horizontal distance between the shock and the body increases with increase in the radial distance from the axis of symmetry. For some intermediate nose radius of curvature the shock is concentric with the rounded nose of the body. Judging by Figure 3 this point is reached somewhere in the vicinity of $R/D = 1.3$. It is interesting to note that the shock shapes in Figures 9 through 12 are identical.

The schlieren photographs of the dummy models at angles of attack (Figures 20 - 44 and Figures 48 - 53) have not been analyzed in detail but are included to show how the shock shapes on the various bodies distort as the angle of yaw is changed. There is nothing extraordinary or unexpected in the distortion of the shock shape except

that the "axis" of the shock surface is yawed by a much smaller angle than the body axis.

Shock standoff distance, δ_1, as measured from the schlieren photographs of models A through I, is plotted versus nose radius of curvature in Figure 54. A correlation of the phenomena observed on the schlieren photographs with the behavior of this curve indicates that the curve can be logically divided into three regions.

For the more spherical-nosed bodies (R/D = 0.5 to R/D = 0.7) the shock standoff distance is linearly proportional to the nose radius of curvature, the shock standoff distance being approximately one-sixth of the nose radius of curvature. The actual equation for the straight line segment of the curve is

$$\delta_1/D = 0.003 + 0.154\,(R/D) \quad \text{for} \quad .500 \leqslant R/D \leqslant \sim 0.7$$

In Reference 5 Oliver found that the sonic point on a hemispherical nose at M = 5.8 occurs approximately 44° from the axis. In Figure 3 the included angle ϕ for R/D = 0.727 is approximately 44°. Thus the upper limit of Region I, the nearly spherical-nosed bodies, is the nose radius of curvature for which the included angle ϕ coincides with the angle at which the sonic point is found on a hemispherical nose.

Inasmuch as the nose portion of each of the models considered here is a segment of a hemisphere, it is conceivable that the curve of Figure 54 could have been derived by turning down the cylindrical afterbody of the hemispherical-nosed model in steps, and after each step measuring the standoff distance from a schlieren photograph obtained in a tunnel test. If this were done Region I would consist of those bodies for which the sonic point remains on the surface of the

spherical nosed segment, the upper limit being where the cut goes through the sonic point of the original hemispherical nose segment and the sonic point appears at the shoulder.

As the nose radius of curvature is increased in Region I the sonic point on the shock and the sonic point on the body surface move outward from the axis as shown in Figures 14 through 17.

In Figure 55 shock standoff distance has been plotted versus the reciprocal of the nose radius of curvature. The obvious linearity of this curve over the range $(R/D)^{-1} = 0.4$ to $(R/D)^{-1} = 1.4$ indicates a hyperbolic relationship between shock standoff distance and nose radius of curvature over the range $R/D = 0.7$ to $R/D = 2.5$, which shall be referred to as Region II. The equation for this segment of the curve is

$$\delta_1/D = 0.265 - \frac{0.1095}{(R/D)} \quad \text{for} \quad \sim 0.7 \leqslant R/D \leqslant \sim 2.5$$

With only slight error involved this same equation could be used to describe the curve on out to $R/D = \infty$ inasmuch as the measured value of δ_1/D at $R/D = \infty$ is 0.269.

The schlieren photographs of bodies included in this range (Figures 12 and 13) show that as the nose radius of curvature increases the sonic point on the shock moves outward from the axis while the sonic point on the body remains fixed at the shoulder.

The fact that there is no discernible difference in the shock shape or δ_2 for models having large nose radii of curvature implies that in the region of large nose radii of curvature the shock standoff distance of a particular body is equal to the shock standoff distance corresponding to the flat-nosed body, minus the rise of the spherical nose segment of that body, or

$$\delta_1 = \delta_{1_\infty} - h \quad \text{for} \quad R/D \geq \sim 2.5$$

But the rise of the spherical nose segment, h, is a geometric function of the nose radius of curvature

$$h/D = R/D - \sqrt{(R/D)^2 - 0.25}$$

so that

$$\delta_1/D = (\delta_{1_\infty}/D) - (R/D) + \sqrt{(R/D)^2 - 0.25} \quad .$$

In Figure 56 curves of δ_1/D and h/D versus R/D have been added together. It can be seen that in Region III for any value of R/D greater than R/D = 2.5 the following relation is appropriate

$$\delta_1/D \doteq 0.269 - R/D + \sqrt{(R/D)^2 - 0.25} \quad \text{for} \quad R/D \geq \sim 2.5$$

Varying the nose radius of curvature in Region III does not alter the position of the shock or body sonic points. The sonic point on the body surface remains at the shoulder and the sonic point on the shock remains at a fixed position opposite the body sonic point.

The quantity δ_2 is well and consistently defined. In effect it is the minimum height of an annular "throat" through which the mass flow is equal to the mass flow through the shock wave within the sonic ring. In Figure 54 the quantity δ_2 is plotted versus nose radius of curvature. For values of $R/D \geq \sim 1.3$, δ_2 is a measure of the distance from the sonic point on the shock to the sonic point on the body and its value appears to be a constant equal to the value of δ_2 for the flat nosed body. As the nose segment approaches hemispherical shape, $R/D \leq \sim 1.3$, δ_2 decreases rapidly and linearly. In this region δ_2 is not a measure of the distance between the shock and body sonic

points. It is interesting to note that the transition point, or knee, of the δ_2 curve occurs at R/D = 1.3 which corresponds to the nose radius of curvature for which the shock is concentric with the rounded nose of the body.

The parameter δ_2 seems to have substantial meaning in the case of the more flat-nosed bodies where the sonic point on the body surface occurs at the shoulder. In Reference 6 Moeckel points out the analogy between the flow around such a body, for which the location of the maximum constriction and the sonic point coincide at the shoulder, and the flow past the throat section of a supersonic nozzle.

A calculation of the mass balance indicated above in the definition of δ_2 and suggested by the above analogy has been carried out in the Appendix for the case of the flat-nosed body. Since the shape of the sonic line and the velocity direction relative to such a line are not known in advance, it was assumed that the sonic line is a straight line joining the sonic points on the shock and the body surface, and that the velocity vector is perpendicular to the sonic line. To simplify the calculation the density ratio across the shock at each point on the shock was assumed to be the same as for a normal shock. In a more rigorous calculation this assumption was found to be justified, inasmuch as the integration of a variable density ratio along the shock resulted in only a very slight difference in the answer obtained. It is interesting to note how closely the value of δ_2 obtained from the mass balance equation approximates the actual measured value, even with these assumptions. The calculation gives $\delta_2/D = .1978$ whereas the actual measured value was $\delta_2/D = .186$, an error of about six per cent.

In Reference 7 Hayes has developed a theoretical equation to describe the shock shape corresponding to a flat-nosed cylinder in a hypersonic flow. Hayes' equation is

$$\delta^2 = \delta_1^2 - \tfrac{1}{2} k y^2$$

where k is the density ratio across the shock. In Figure 57 the actual shape of the shock on a flat-nosed cylinder has been reproduced for comparison with Hayes' theoretical shock shape. The shock shape appears to correspond quite closely. In the Appendix the value of δ_1/D corresponding to the measured δ_2/D is computed using Hayes' equation. The value of δ_1/D so computed differs by only 5.2 per cent from the measured δ_1/D.

Schlieren photographs of the concave-nosed models, M and N, are shown in Figures 18, 19, 29, 30, and 40. It can be seen that the shock shapes are identical on each of the models. When blown up to the same scale and superimposed on the flat-nosed model, the shock shapes were found to coincide. As far as shock shape is concerned, it appears that concave-nosed bodies in hypersonic flow behave just as though they were flat-nosed bodies.

For the rounded shoulder models, shock standoff distance, δ_1, as measured from the schlieren photographs of models A, I, J, K, and L, is plotted versus shoulder radius in Figure 58. The limiting cases of the rounded shoulder bodies are the hemispherical nose and the flat nose. There appears to be a linear relationship between the shock standoff distance, δ_1, and the radius of the rounded shoulder, r. The equation of the line is

$$\delta_1/D = 0.269 - 0.38\,(r/D) \quad \text{for} \quad 0 \leq r/D \leq 0.5$$

This curve emphasizes the importance of the body shape in the region of the sonic point in determining the shock shape and the corresponding shock standoff distance.

B. Surface Static Pressure Distributions

1. General

The pressure distributions at a Mach number of 5.8 and a Reynolds number per inch of 2.22×10^5 for each of the three pressure models at 0, 4, and 8 degrees angle of yaw are plotted in Figures 59 through 73 in the form $C_p/C_{p_{max}}$ versus S/D. To represent the three-dimensional character of the pressure distributions, particularly on the yawed bodies, the pressure distributions have been plotted for six meridian planes. The uniformity of the test section flow was apparent in that as the pressure models were rotated at zero angle of yaw the variation in the value of the pressure coefficient at any particular orifice position was never more than two per cent. The values of $C_p/C_{p_{max}}$ at zero angle of yaw given in the graphs correspond to the average of the pressure coefficients at a particular orifice position. At angles of attack pressure coefficients at a particular orifice position in planes symmetrical with respect to the vertical plane varied less than two per cent. The values of $C_p/C_{p_{max}}$ at angle of attack for symmetrical diagonal planes and the horizontal plane given in the graphs represent the average of the pressure coefficients measured in the symmetrical planes. The curves determined by the experimental points have been extended on the pressure plots of the sharp shouldered

models to a point at the shoulder where $C_p/C_{p_{max}} = .517$ which is the ratio of the pressure coefficient at the sonic point to the maximum pressure coefficient.

In the graphical representation of the pressures at angle of attack, the pressures corresponding to positive values of S/D refer to the bottom half of the model when it is at a positive angle of pitch.

At angles of attack the horizontal and diagonal meridian planes have maximum values of $C_p/C_{p_{max}}$ less than one, since these planes containing the orifices do not pass through the stagnation point.

2. Flat Nosed Cylinder

In Figures 59, 60, and 61 the surface static pressure distributions on the flat-nosed cylinder are shown for the vertical, 030° - 210°, and horizontal planes, respectively, at angles of yaw of 0, 4, and 8 degrees. At zero yaw angle the pressure remains within 10 per cent of the stagnation pressure out to about nine-tenths of the radius of the cylinder. At the shoulder there appears to be a sudden overexpansion and recompression. Apparently the mechanism is a weak oblique shock in the vicinity of the shoulder. No such shocks are visible on the schlieren photographs, probably because of the low tunnel densities. In the vertical plane the ratio of the pressure coefficient on the lower surface of the cylindrical afterbody with the model at positive angle of attack to the maximum pressure coefficient on the body as predicted by modified Newtonian theory (Ref. 8) is 0 for $\alpha = 0$, .0049 for $\alpha = 4^\circ$, and .0194 for $\alpha = 8^\circ$. These values are asymptotic values on the cylindrical afterbody "far" from the nose. A Prandtl-Meyer expansion through an angle $\Delta\nu = 90^\circ$ at the shoulder would give a pressure near the

shoulder on the cylindrical afterbody corresponding to a pressure ratio of $C_p/C_{p_{max}} = -.0231$. The assumption of a Prandtl-Meyer expansion through 90^o at the shoulder is the same as assuming that the direction of the sonic velocity vector is tangential to the nose surface at the shoulder. Thus the value of $C_p/C_{p_{max}}$ obtained in this way is actually a minimum value.

The experimental surface pressure distribution on the flat-nosed cylinder at zero angle of yaw is compared with the surface pressure distribution on a flat-nosed cylinder as predicted by Probstein (Ref. 9) in Figure 62. Modified Newtonian theory would predict a constant pressure over the flat nose of the cylinder equal to the stagnation pressure. Out to about 4/5 of the radius the experimental pressure distribution lies midway between these two approximations, dropping off rapidly thereafter and falling far below the approximation curves at the shoulder.

3. Round Nosed Cylinder, R/D = 1.30

In Figures 63, 64, 65, and 66 the surface static pressure distributions on the round-nosed cylinder, R/D = 1.30, are shown for the vertical, 030^o - 210^o, 060^o - 240^o, and horizontal planes, respectively, at angles of yaw of 0, 4, and 8 degrees. As in the case of the flat-nosed cylinder there appears to be an overexpansion and recompression at the shoulder. In the vertical plane the ratio of the pressure coefficient on the lower surface of the cylindrical afterbody with the model at positive angle of attack to the maximum pressure coefficient on the body as predicted by modified Newtonian theory is the same as indicated above for the flat-nosed cylinder. Assuming

the direction of the sonic velocity vector tangential to the nose surface at the shoulder, a Prandtl-Meyer expansion through an angle $\Delta\nu = 67.4^{\circ}$ at the shoulder would give a pressure near the shoulder on the cylindrical afterbody corresponding to a minimum value of $C_p/C_{p_{max}} = -.0176$.

A comparison of the experimental surface pressure distribution on the round-nosed cylinder at zero angle of yaw and the surface pressure distribution as predicted by modified Newtonian theory is shown in Figure 67. With the Busemann correction for centrifugal force added to the modified Newtonian curve, the approximation of the theoretical curve to the experimental is reasonably accurate, but the experimental points depart radically from the approximate curve near the shoulder. It is perhaps justifiable to use the Busemann correction here since the shock is almost concentric with the body shape.

4. Flat Nosed Cylinder with Rounded Shoulder, r/D = 0.208

In Figures 68, 69, and 70 the surface static pressure distributions on the flat-nosed cylinder with rounded shoulder, r/D = 0.208, are shown for the vertical, 030° - 210°, and horizontal planes, respectively, at angles of yaw of 0, 4, and 8 degrees. Over the flat portion of the nose the pressure remains within 5 per cent of the stagnation pressure, then sharply drops off at the rounded shoulder. However, the expansion around the shoulder is smooth and apparently there is no overexpansion. Again the ratio of the pressure coefficient on the cylindrical afterbody in the vertical plane to the maximum pressure coefficient on the body as predicted by modified Newtonian theory is 0 for $\alpha = 0$, .0049 for $\alpha = 4^{\circ}$, and .0194 for $\alpha = 8^{\circ}$. The experimental surface pressure

distribution on the flat-nosed cylinder with a rounded shoulder at zero angle of yaw is compared with the surface pressure distribution predicted by modified Newtonian theory in Figure 71. The general nature of the experimental pressure distribution is approximated by the modified Newtonian theory prediction but the actual pressures predicted by Newtonian theory are too high.

Figure 72 is a comparison of the surface pressure distributions at zero yaw angle on the flat-nosed cylinder, the round-nosed cylinder (R/D = 1.3), and a hemispherical-nosed cylinder (previously determined by R. E. Oliver in Reference 5). This plot differs from the others in that $C_p/C_{p_{max}}$ is plotted versus S/S*, where S* is the distance to the sonic point on the surface of the body. This representation purports to show the way in which the pressure decreases from the stagnation pressure to the pressure corresponding to the sonic point and brings out the effect of nose shape more clearly. The sonic points on both models I and E occur at the shoulder; on model A (hemisphere) the sonic point is approximately 44° from the axis. The influence of both the local body shape and the shape of the body in the sonic region on the pressure distribution is apparent.

The surface pressure distributions at zero angle of yaw on the flat-nosed cylinder and the flat-nosed cylinder with rounded shoulder (r/D = 0.208) are compared in Figure 73. Here again $C_p/C_{p_{max}}$ is plotted versus S/S*. The sonic point on the rounded shoulder model occurs after 36.7° of turn around the shoulder. In the vicinity of the shoulders the surface pressure distributions differ markedly as might be expected. Here again can be seen the important effect on the pressure distribution of both the shape of the body locally and the shape of the body in the sonic region.

IV. CONCLUSIONS

A correlation of the phenomena observed on the schlieren photographs with the behavior of a curve resulting from a plot of shock standoff distance, δ_1, versus nose radius of curvature, R, indicates that this curve can be divided into three regions.

For the nearly spherical-nosed bodies of Region I ($.500 \leq R/D \leq \sim 0.7$) the shock standoff distance is linearly proportional to the nose radius of curvature, and the value of the shock standoff distance at M = 5.8 is given by the equation

$$\delta_1/D = 0.003 + 0.154\,(R/D)$$

As the nose radius of curvature is increased in this region the sonic point on the shock and the sonic point on the body surface both move outward from the axis.

In the transitional range of Region II ($\sim .07 \leq R/D \leq \sim 2.5$) the shock standoff distance is related hyperbolically to the nose radius of curvature, the value of the shock standoff distance at M = 5.8 being given by the equation

$$\delta_1/D = 0.265 - \frac{0.1095}{(R/D)}$$

As nose radius of curvature is increased in this region the sonic point on the shock moves outward from the axis while the sonic point on the body remains fixed at the shoulder.

For nearly flat-nosed bodies of Region III ($R/D \geq \sim 2.5$) the shock standoff distance of a particular body is equal to the shock standoff distance corresponding to the flat-nosed body minus the rise of the

spherical nose segment of that body, the value of the shock standoff distance at M = 5.8 being given by the equation

$$\delta_1/D = 0.269 - R/D + \sqrt{(R/D)^2 - 0.25}$$

Varying the nose radius of curvature in this region does not alter the position of the shock or body sonic points. The sonic point on the body surface remains at the shoulder and the sonic point on the shock remains at a fixed position opposite the body sonic point. In this region there is no discernible difference in shock shape.

By employing a simple and crude mass balance calculation relating the mass flow through the shock wave within the sonic ring to the mass flow through an annular "throat" of height δ_2 at the shoulder, a calculated value of δ_2 was obtained which varied by only six percent from the actual measured value.

The shape of the body in the region of the shock is of great importance in determining shock shape and the corresponding shock standoff distance.

Insofar as shock shape is concerned, concave-nosed bodies behave in hypersonic flow just as though they were flat-nosed bodies.

In appropriate applications the surface static pressure distribution given by modified Newtonian theory in conjunction with the Busemann correction is a reasonably accurate hypersonic approximation. Pressure values predicted by this method are particularly good near the axis.

Surface pressure distribution is dependent not only upon the local body shape but also upon the shape of the body in the region of the shock.

REFERENCES

1. Eggers, A. J., Resnikoff, M. M., and Dennis, D. H.: Bodies of Revolution Having Minimum Drag at High Supersonic Airspeeds. NACA TN 3666, February, 1956.

2. Baloga, P. E. and Nagamatsu, H. T.: Instrumentation of GALCIT Hypersonic Wind Tunnels. GALCIT Memorandum No. 29, July, 1955.

3. O'Bryant, W. T. and Machell, R. M.: An Experimental Investigation of the Flow over Blunt-Nosed Cones at a Mach Number of 5.8. GALCIT Hypersonic Research Project, Memorandum No. 32, June 15, 1956. Also, Readers' Forum, Journal of the Aeronautical Sciences, Vol. 23, No. 11, pp. 1054-1055, November, 1956.

4. Ames Aeronautical Laboratory Research Staff: Equations, Tables, and Charts for Compressible Flow. NACA TR 1135, 1953.

5. Oliver, Robert E.: An Experimental Investigation of Flow over Simple Blunt Bodies at a Nominal Mach Number of 5.8. GALCIT Hypersonic Wind Tunnel Memorandum No. 26, June 1, 1955. Also, Journal of the Aeronautical Sciences, Vol. 23, No. 2, February, 1956.

6. Moeckel, W. E.: Approximate Method for Predicting Form and Location of Detached Shock Waves. NACA TN 1921, July, 1949.

7. Hayes, W. D.: Some Aspects of Hypersonic Flow. Ramo-Wooldridge Corporation, January, 1955.

8. Lees, Lester: Hypersonic Flow. Institute of the Aeronautical Sciences, Preprint No. 554, June, 1955.

9. Probstein, Ronald F.: Inviscid Flow in the Stagnation Point Region of Very Blunt-Nosed Bodies at Hypersonic Flight Speeds. (Brown University). WADC TN 52-395, (ASTIA Document No. AD 97273), ARDC, USAF, Wright-Patterson Air Force Base, Ohio.

APPENDIX

CALCULATION OF δ_2/D BY MASS BALANCE ($R/D = \infty$)

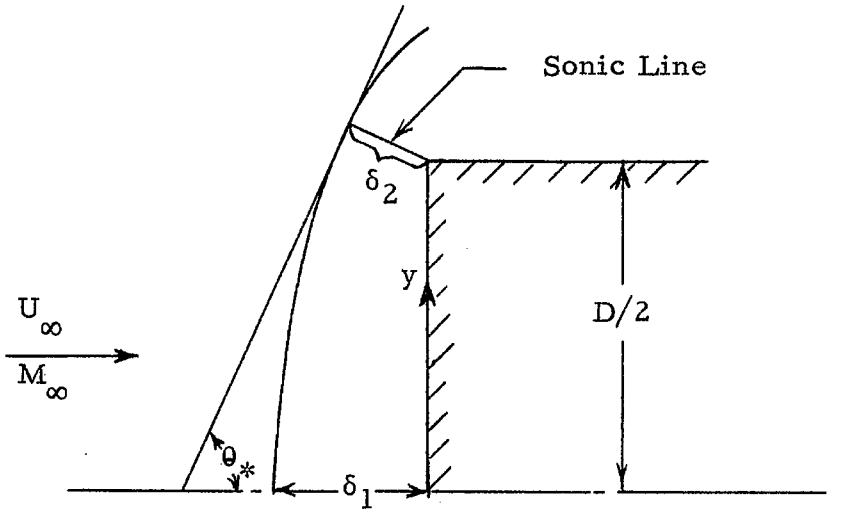

Let A_∞ = area within sonic ring

A_* = area of annular throat of height δ_2

Then, $\rho_\infty U_\infty A_\infty = \rho_* U_* A_*$

$$A_*/A_\infty = (\rho_\infty/\rho_*)(U_\infty/U_*)$$

$$A_*/A_\infty = (\rho_\infty/\rho_{\infty_t})(\rho_{\infty_t}/\rho_{*_t})(\rho_{*_t}/\rho_*)(U_\infty/M_* a_*) \qquad (M_* = 1)$$

In this form A_*/A_∞ can be calculated using Reference 4. Assuming $M_\infty = 5.8$,

$$\frac{A_*}{A_\infty} = \frac{(0.006023)(2.28552)}{(0.6339)(0.03412)} = 0.63646$$

Referring to the figure above, it is apparent that

$A_* = \delta_2 \pi(D + \delta_2 \cos \theta_*)$ and

$A_\infty = \pi(D/2 + \delta_2 \cos \theta_*)^2$

where θ_* is determined from the equation

$$\sin^2 \theta_* = (1/7\, M_\infty^2) \left[3\, M_\infty^2 - 2 + \sqrt{3(3M_\infty^4 - 4M_\infty^2 + 13)} \right] \text{ for } \quad = 1.40$$

For $M_\infty = 5.8$, $\theta_* = 66^\circ 25'$.

Therefore

$$\frac{\delta_2 D + \delta_2^2 \cos \theta_*}{(D/2)^2 + \delta_2 D \cos \theta_* + \delta_2^2 \cos^2 \theta_*} = 0.63646$$

Dividing through by D^2 and rearranging

$$0.2500 + (\delta_2/D) \cos \theta_* + (\delta_2/D)^2 \cos^2 \theta_* = \frac{1}{0.63646} \left[(\delta_2/D) + (\delta_2/D)^2 \cos \theta_* \right]$$

$$\delta_2/D = \frac{-1.17111 + \sqrt{1.37150 + 0.46854}}{0.93708}$$

$$\delta_2/D = 0.1978$$

The measured value of δ_2/D is 0.186. The error is 6.3 per cent.

Hayes' theoretical shock shape equation is

$$\delta^2 = \delta_1^2 - \tfrac{1}{2} k y^2$$

at $y = D/2 + \delta_2 \cos \theta_*$, $\quad \delta = \delta_2 \sin \theta_*$

Therefore,

$$\delta_1^2 = (\delta_2 \sin \theta_*)^2 + \tfrac{1}{2}(1/5.224)(D/2 + \delta_2 \cos \theta_*)^2$$

$$(\delta_1/D)^2 = (\delta_2/D)^2 \sin^2 \theta_* + (0.09571) \left[0.2500 + \delta_2/D \cos \theta_* + (\delta_2/D)^2 \cos^2 \theta_* \right]$$

Substituting the measured value of δ_2/D (= 0.1978) into the above equation, the result is

$$\delta_1/D = 0.255$$

The measured value of δ_1/D is 0.269. The error is 5.2 per cent.

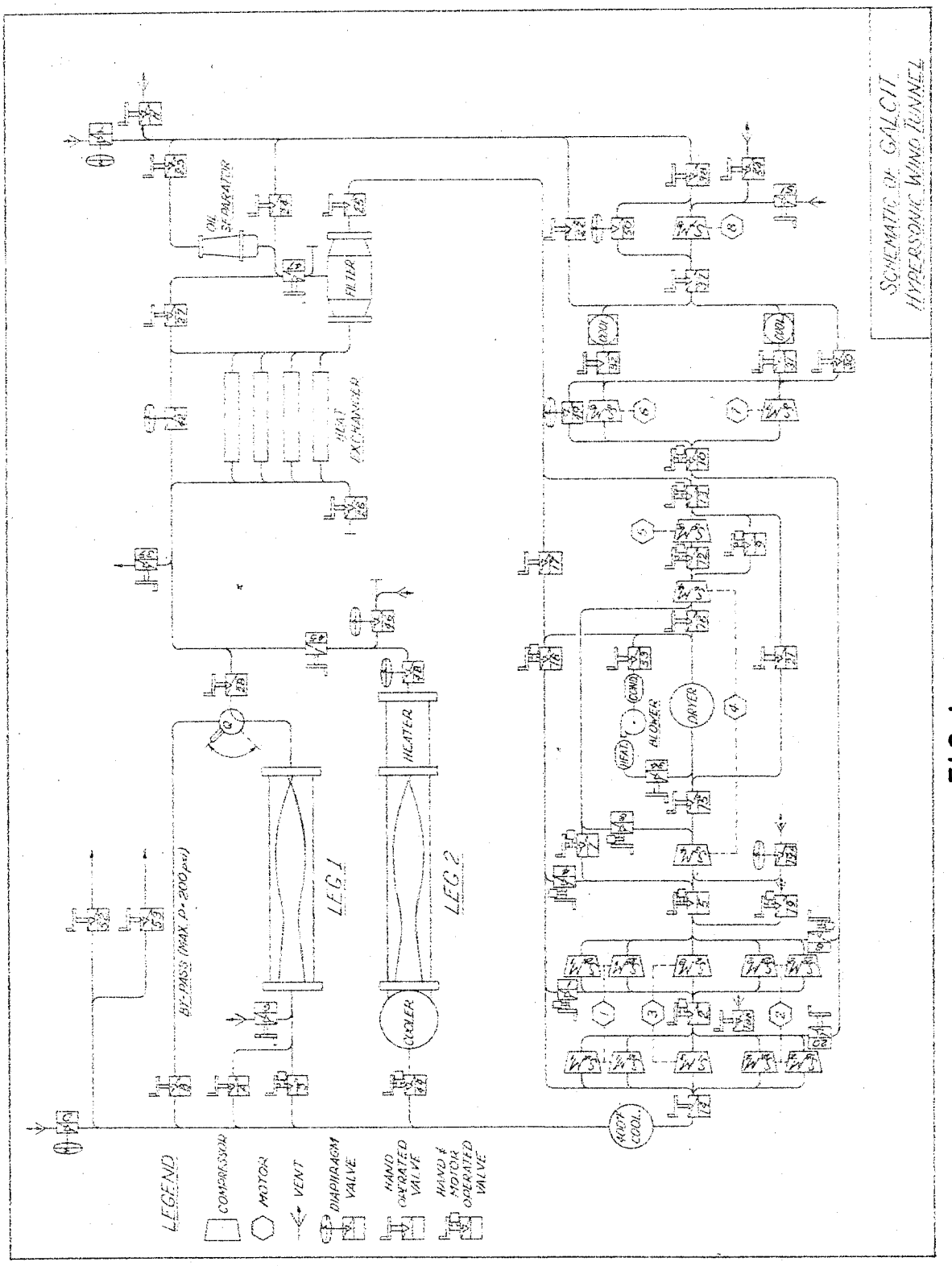
SCHEMATIC OF CALCIT
HYPERSONIC WIND TUNNEL
LEGEND
COMPRESSOR
MOTOR
VENT
DIAPHRAGM VALVE
HAND OPERATED VALVE
HAND & MOTOR OPERATED VALVE
LEG 1
LEG 2
HEATER
COOLER
HEAT EXCHANGER
FILTER
OIL SEPARATOR
BY-PASS (MAX. P = 200 psi)
DRIER
BLOWER
AFTER COOL.

FIG. 1

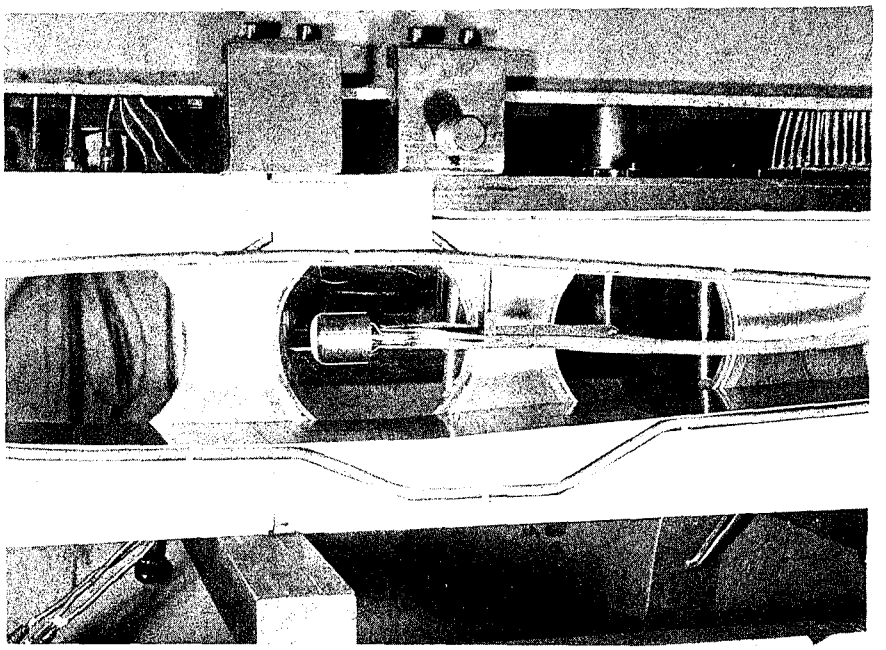

(A)

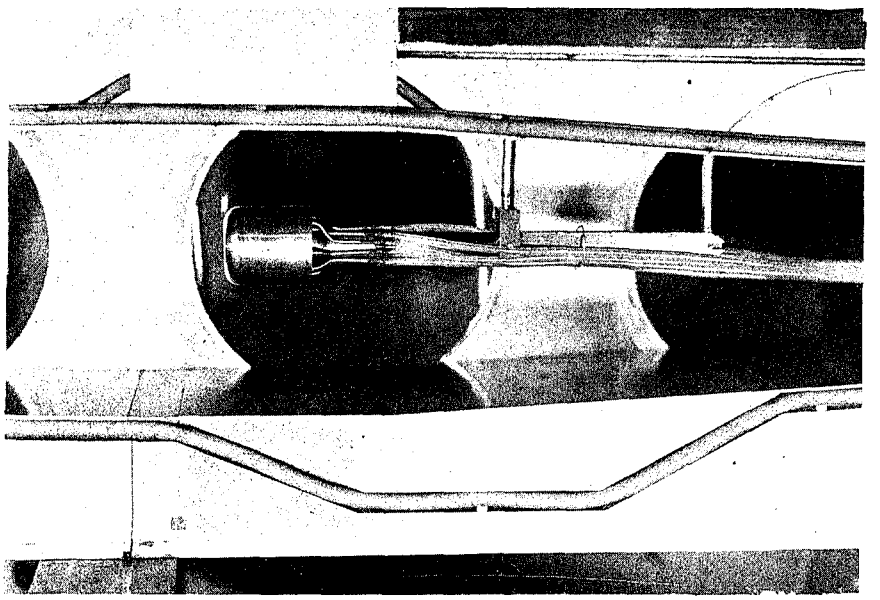

(B)

FIG. 2

TEST SECTION OF HYPERSONIC TUNNEL SHOWING METHOD OF MOUNTING MODELS

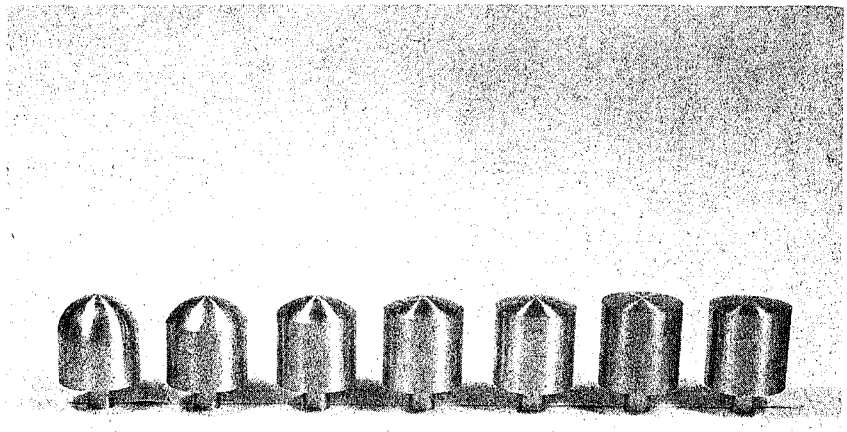

(A)

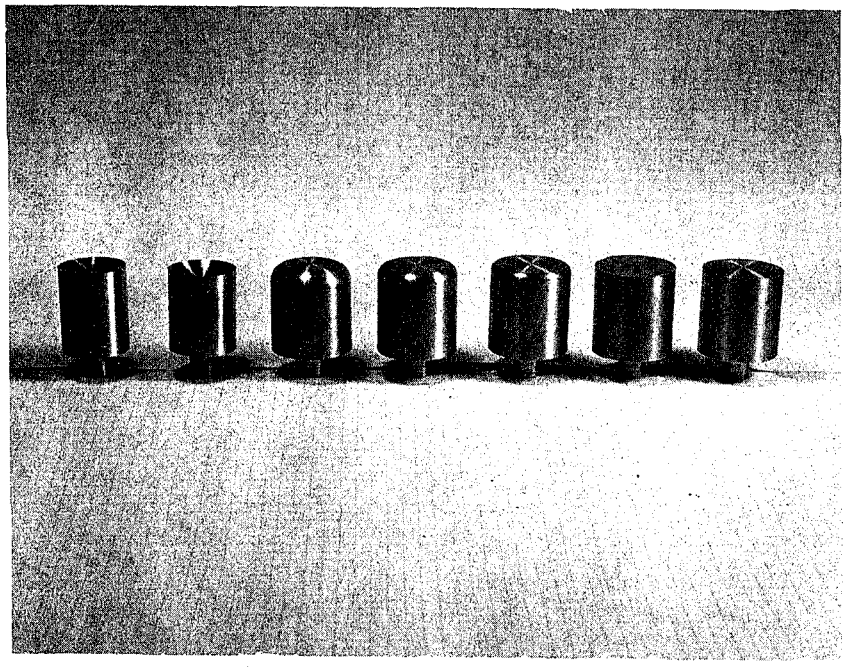

(B)

FIG. 3

PHOTOGRAPHS OF DUMMY MODELS USED IN SCHLIEREN STUDIES

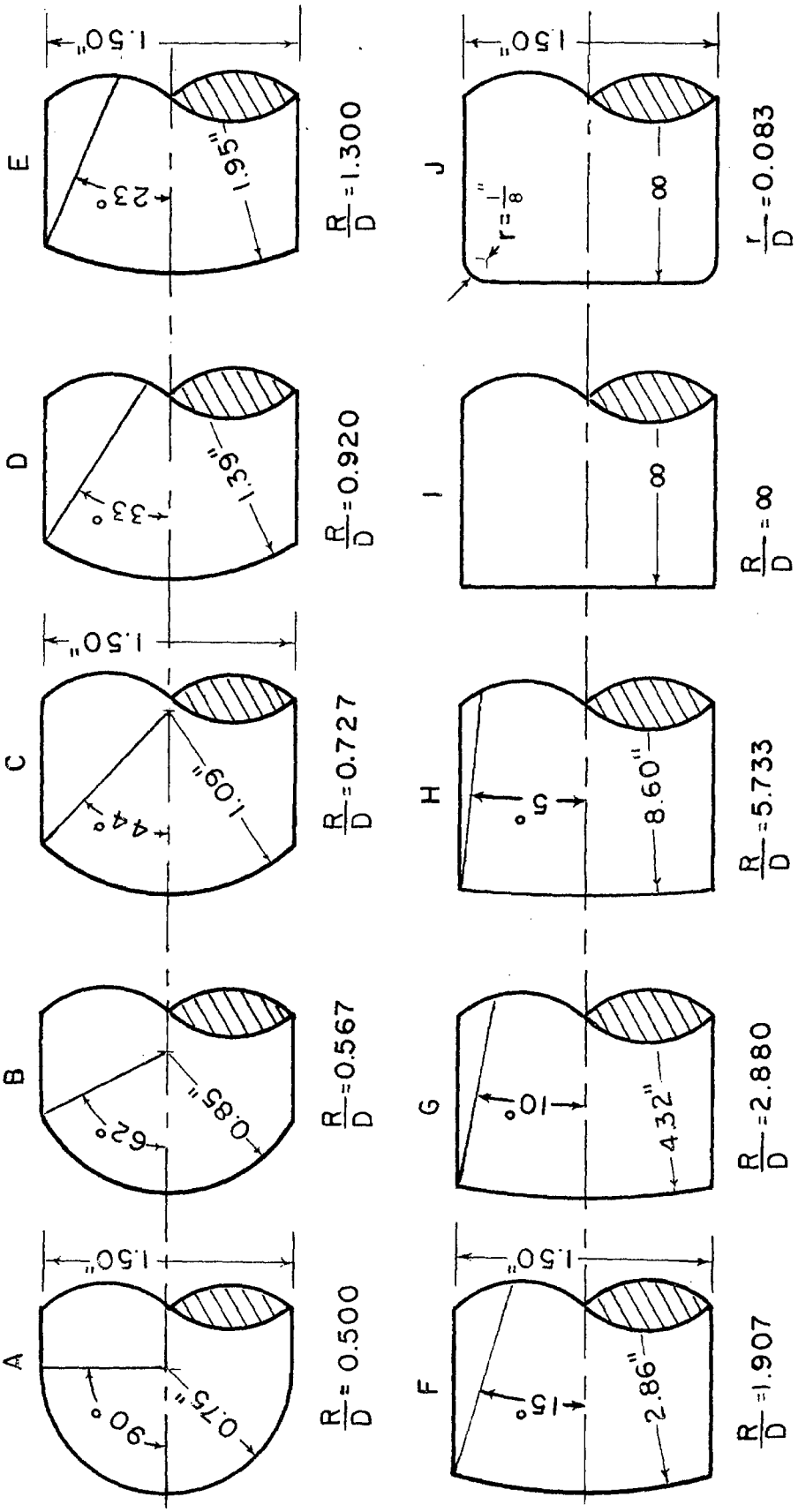

FIG. 4. NOSE CONFIGURATION OF DUMMY MODELS

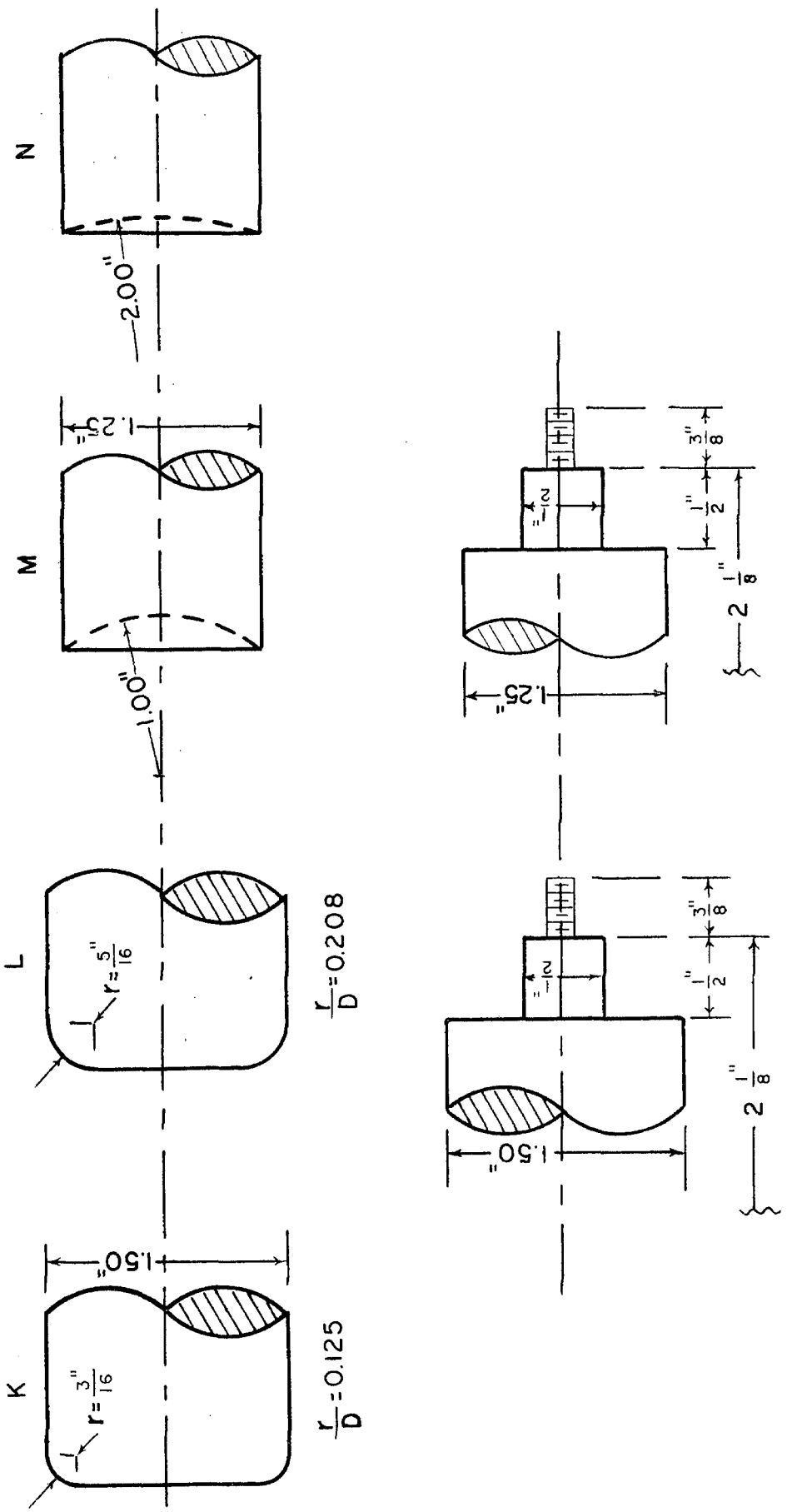

FIG. 5. NOSE AND AFTERBODY CONFIGURATION OF DUMMY MODELS

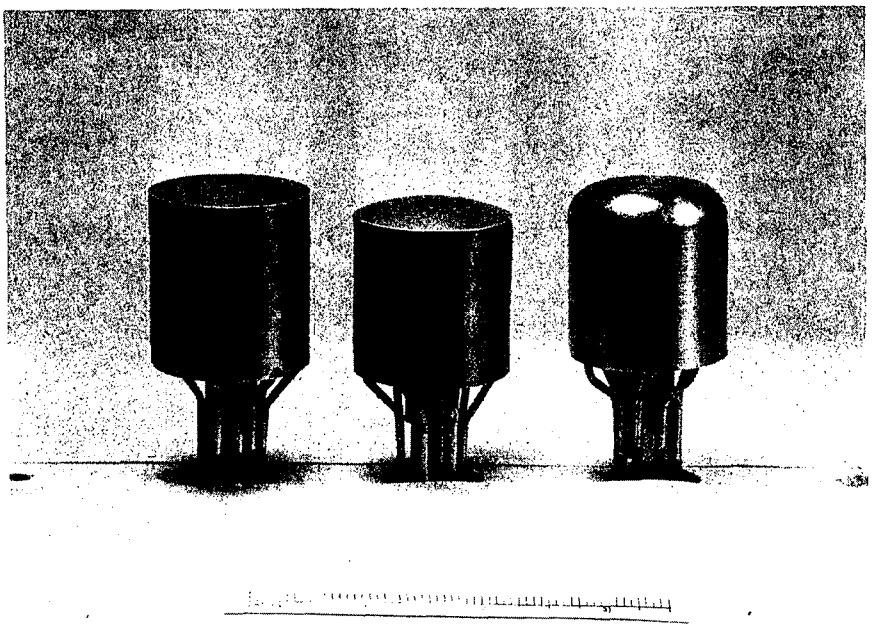

FIG. 6

PHOTOGRAPH OF STATIC PRESSURE MODELS

Orifice	S(in)
1	0.000
2	0.100
3	0.200
4	0.350
5	0.500
6	0.650
7	0.700
8	0.800
9	0.850

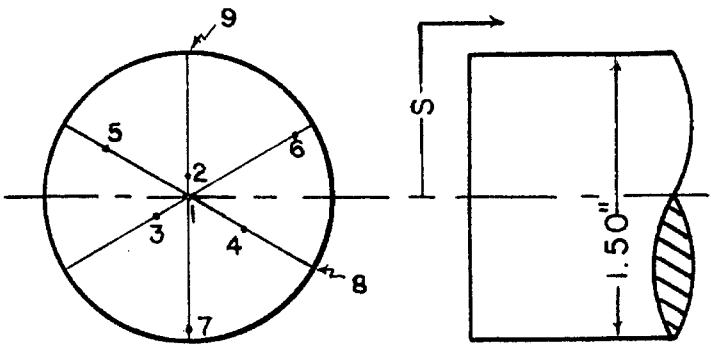

(A) FLAT NOSE MODEL

Orifice	S(in)
1	0.000
2	0.100
3	0.200
4	0.350
5	0.510
6	0.665
7	0.720
8	0.820
9	0.870

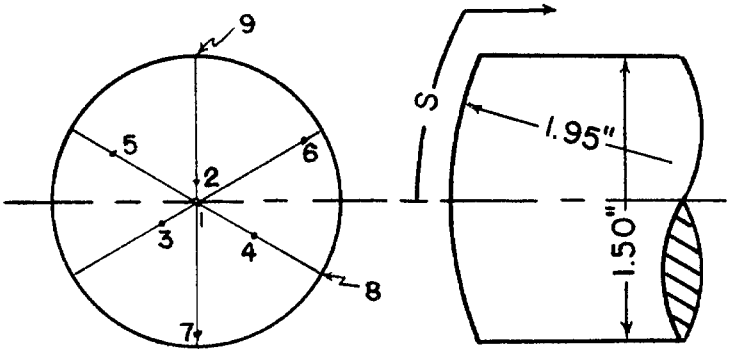

(B) 1.95" NOSE RADIUS MODEL

Orifice	S(in)
1	0.000
2	0.100
3	0.200
4	0.350
5	0.425
6	0.500
7	0.580
8	0.671
9	0.928
10	1.028

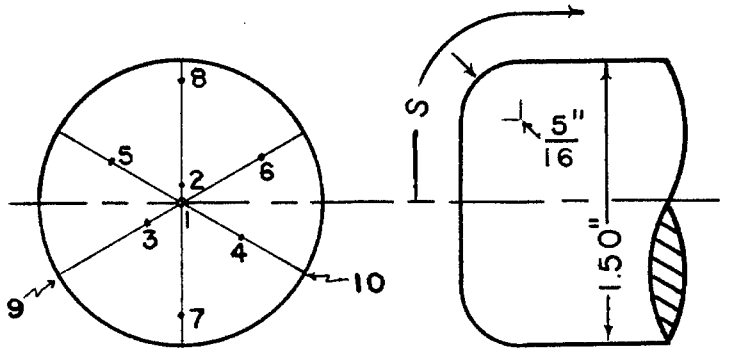

(C) $\frac{5}{16}$" ROUNDED SHOULDER MODEL

FIG. 7. PRESSURE MODEL ORIFICE LOCATION

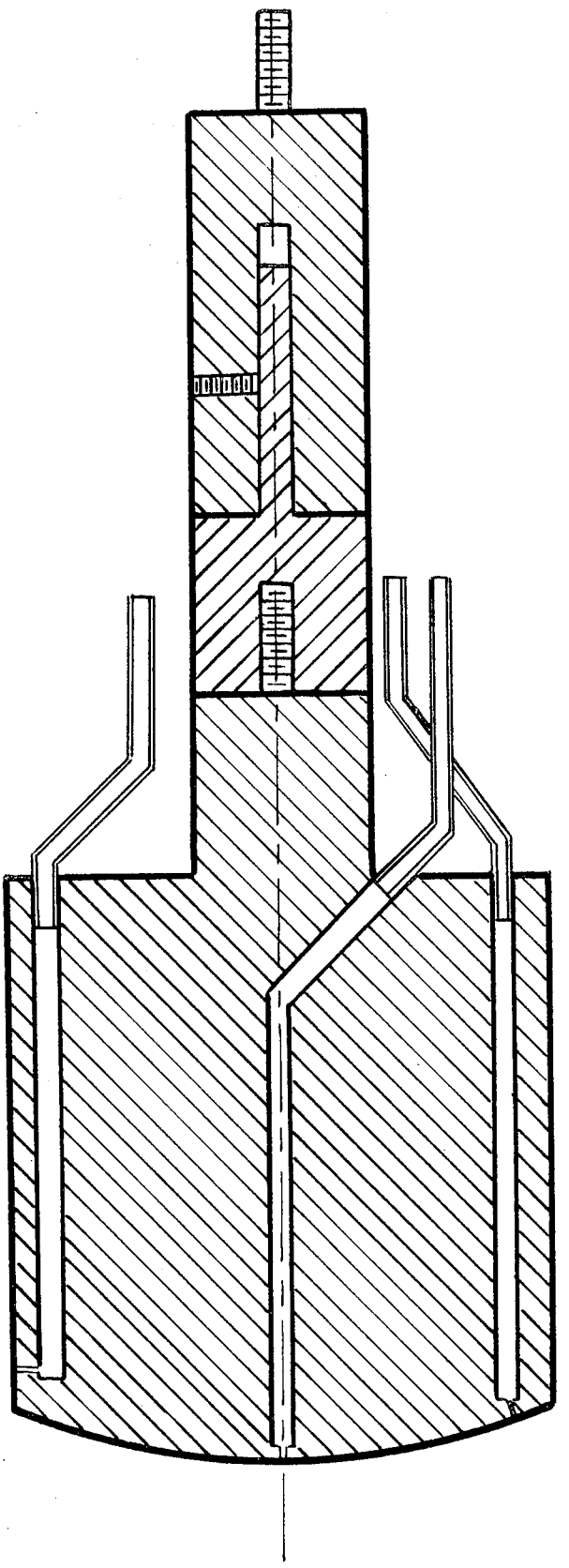

FIG. 8. CUTAWAY VIEW OF TYPICAL PRESSURE MODEL

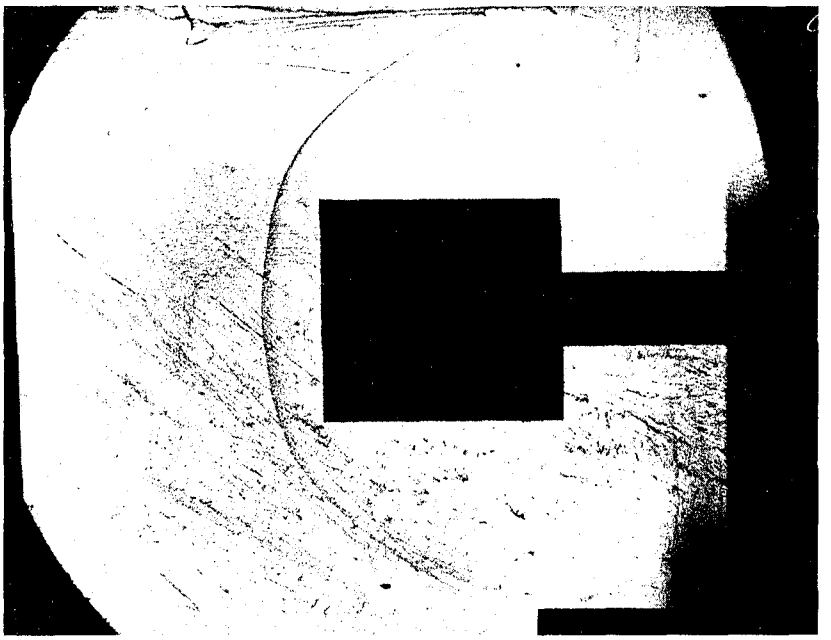

FIG. 9

SCHLIEREN PHOTOGRAPH OF FLAT FACED BLUNT BODY ($R/D = \infty$) AT ZERO DEGREES ANGLE OF YAW, $M = 5.8$.

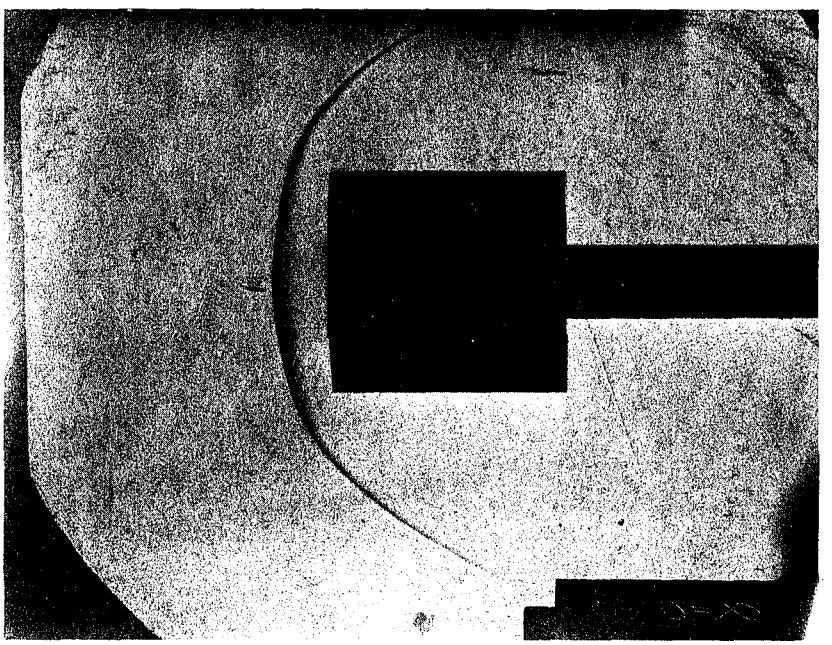

FIG. 10

SCHLIEREN PHOTOGRAPH OF ROUND NOSED BLUNT BODY ($R/D = 5.733$) AT ZERO DEGREES ANGLE OF YAW, $M = 5.8$.

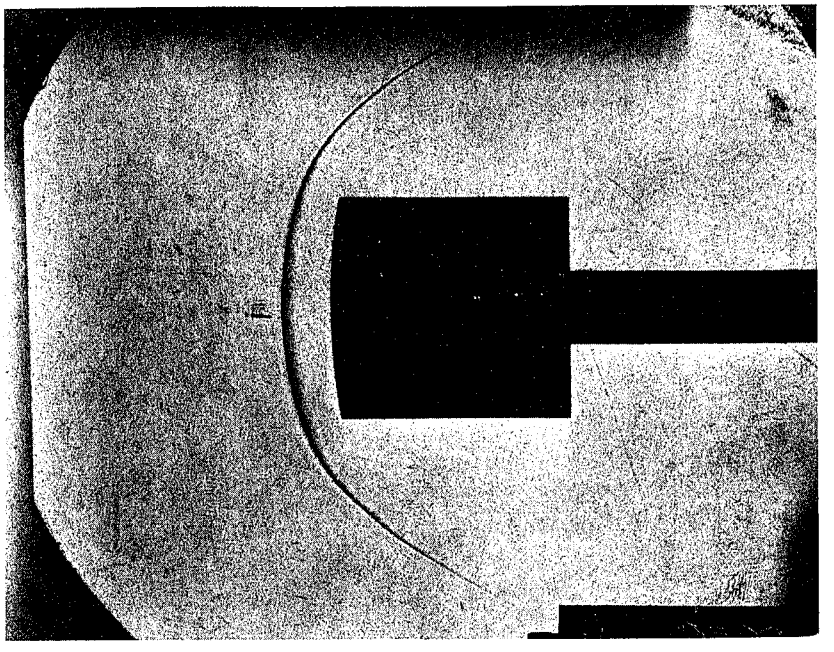

FIG. 11

SCHLIEREN PHOTOGRAPH OF ROUND NOSED BLUNT BODY (R/D = 2.880) AT ZERO DEGREES ANGLE OF YAW, M = 5.8.

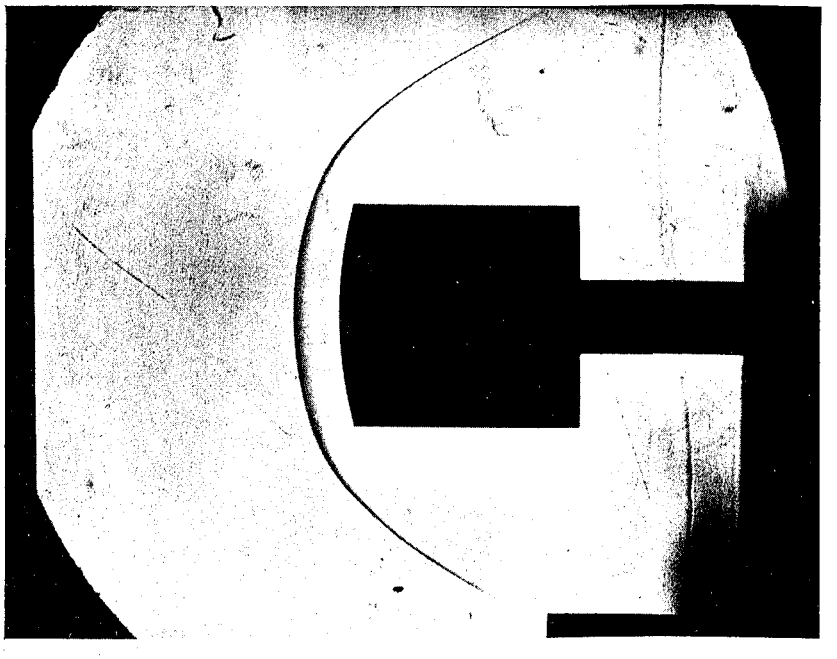

FIG. 12

SCHLIEREN PHOTOGRAPH OF ROUND NOSED BLUNT BODY (R/D = 1.907) AT ZERO DEGREES ANGLE OF YAW, M = 5.8.

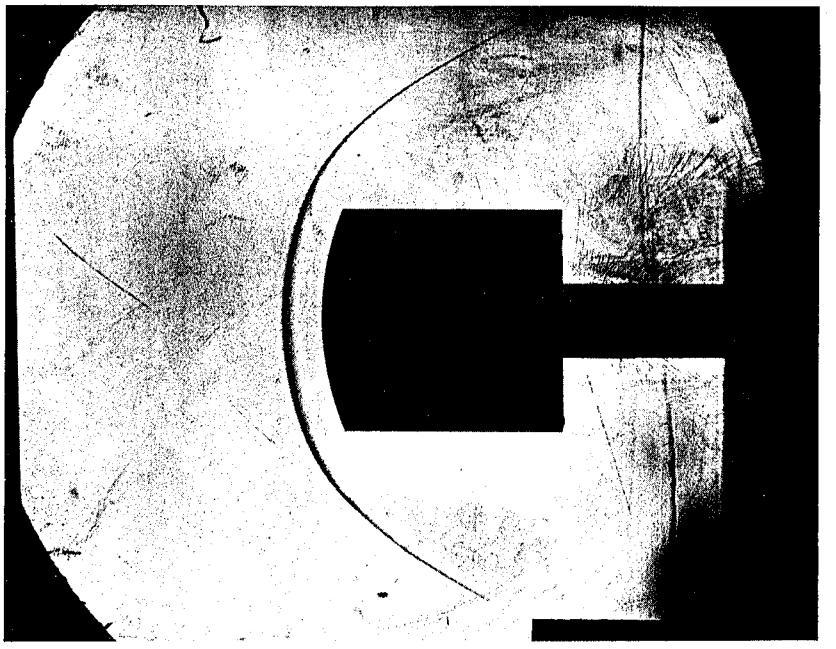

FIG. 13

SCHLIEREN PHOTOGRAPH OF ROUND NOSED BLUNT BODY (R/D = 1.300) AT ZERO DEGREES ANGLE OF YAW, M = 5.8.

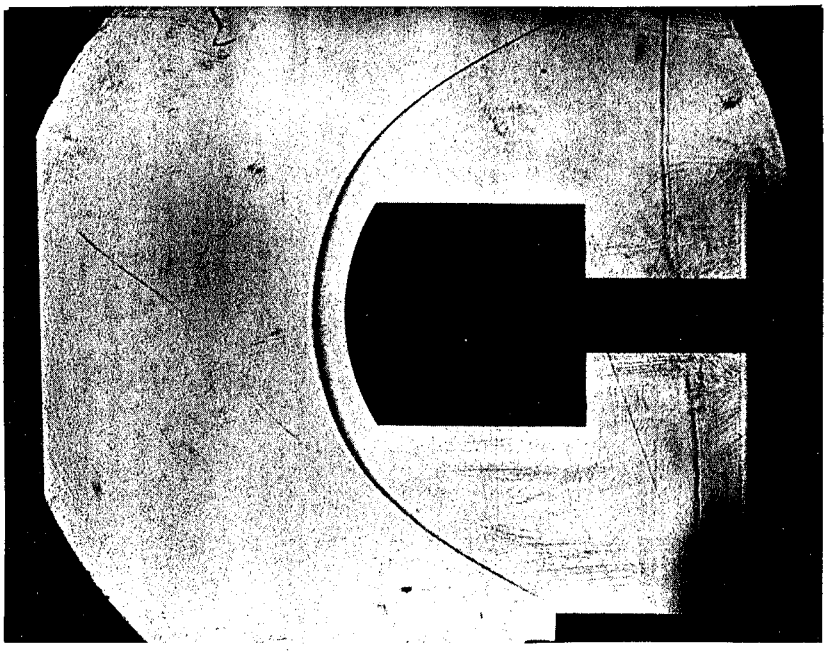

FIG. 14

SCHLIEREN PHOTOGRAPH OF ROUND NOSED BLUNT BODY (R/D = 0.920) AT ZERO DEGREES ANGLE OF YAW, M = 5.8.

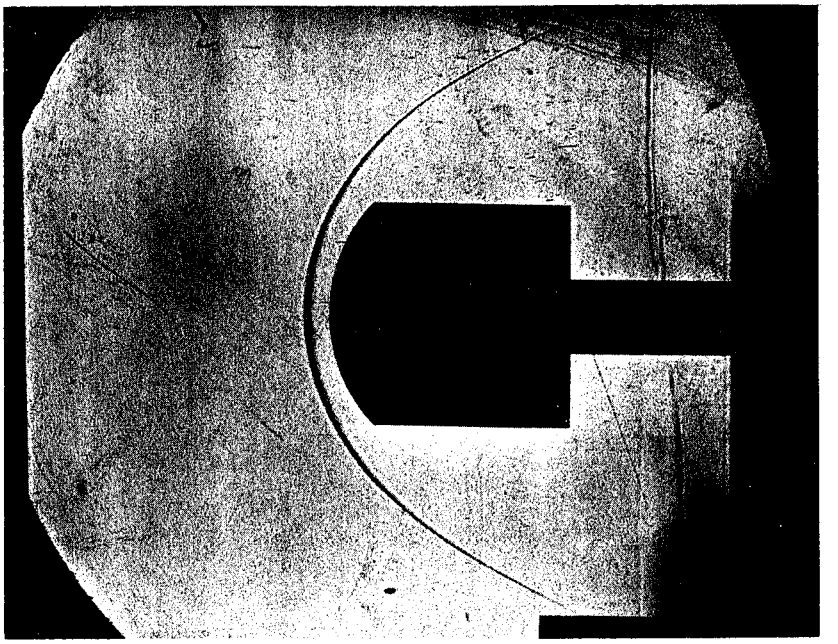

FIG. 15

SCHLIEREN PHOTOGRAPH OF ROUND NOSED BLUNT BODY (R/D = 0.727) AT ZERO DEGREES ANGLE OF YAW, M = 5.8.

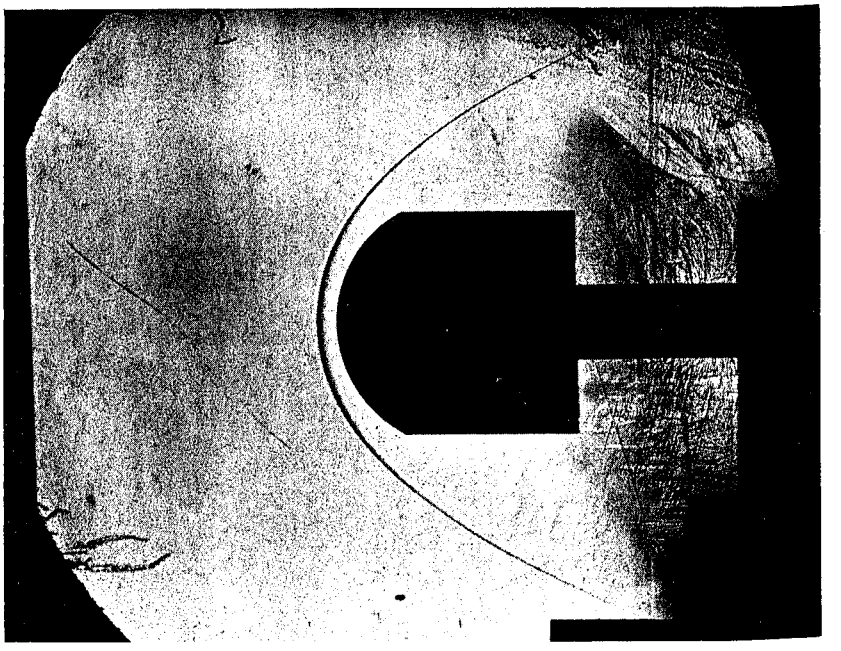

FIG. 16

SCHLIEREN PHOTOGRAPH OF ROUND NOSED BLUNT BODY (R/D = 0.567) AT ZERO DEGREES ANGLE OF YAW, M = 5.8.

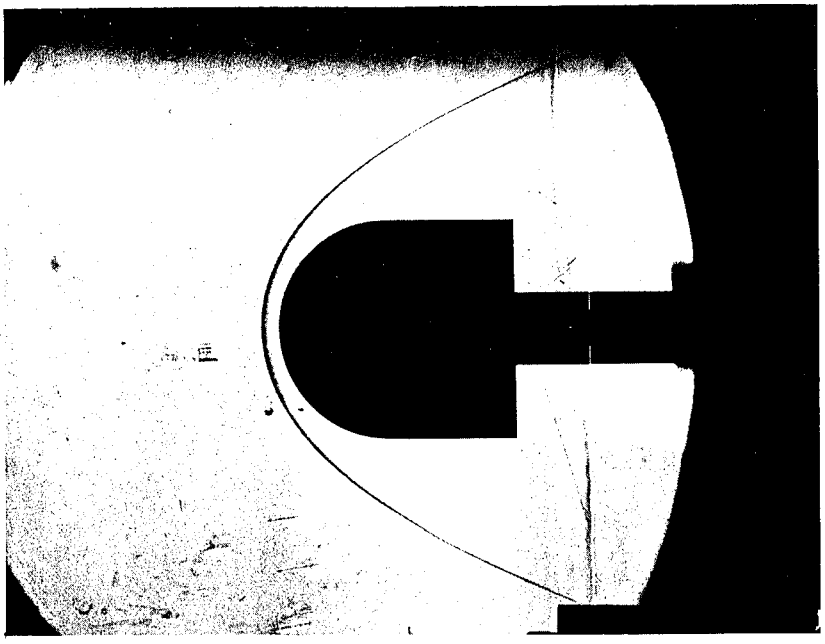

FIG. 17

SCHLIEREN PHOTOGRAPH OF ROUND NOSED BLUNT BODY (R/D = 0.500) (HEMISPHERE) AT ZERO DEGREES ANGLE OF YAW, M = 5.8.

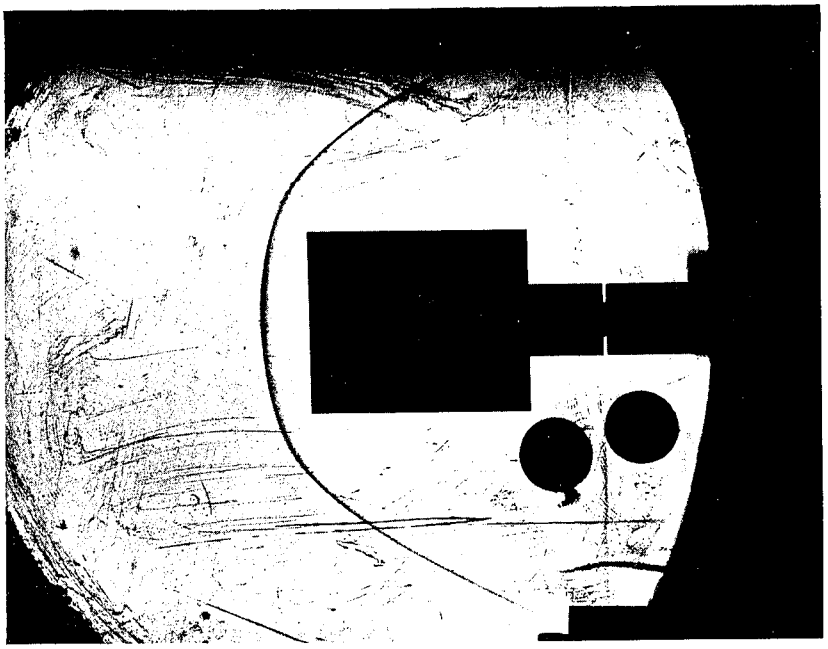

FIG. 18

SCHLIEREN PHOTOGRAPH OF CONCAVE NOSED BLUNT BODY (R/D = 0.800) AT ZERO DEGREES ANGLE OF YAW, M = 5.8.

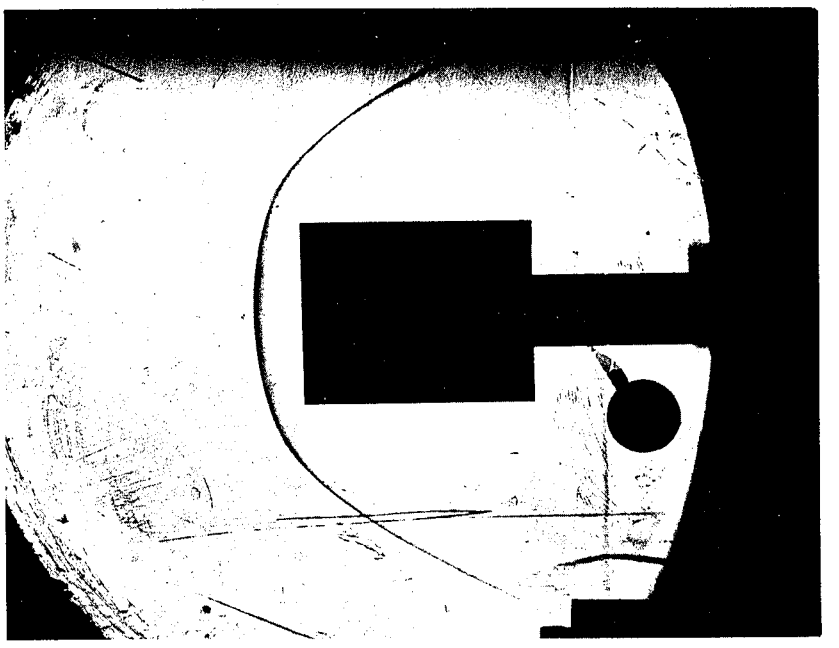

FIG. 19

SCHLIEREN PHOTOGRAPH OF CONCAVE NOSED BLUNT BODY (R/D = 1.600) AT 0 DEGREES ANGLE OF YAW, M = 5.8.

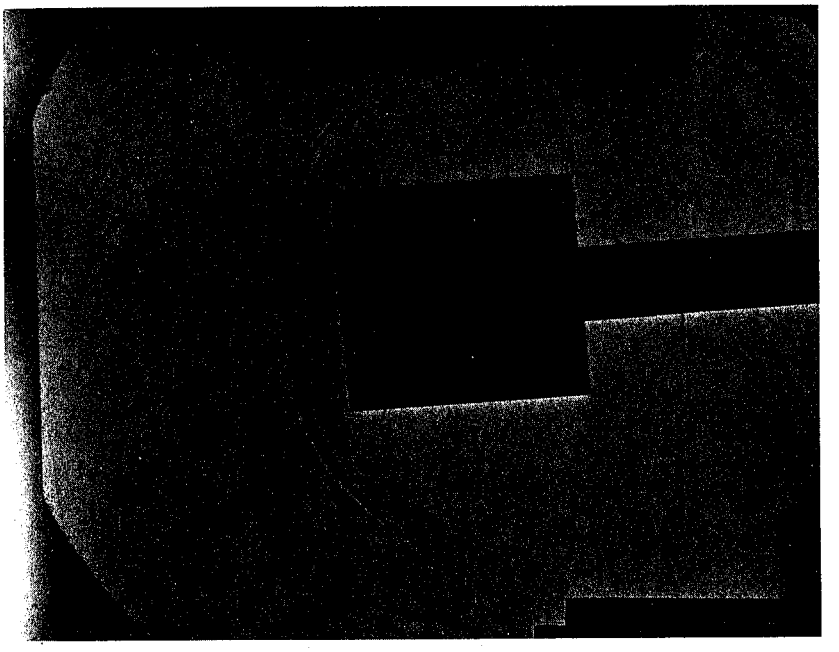

FIG. 20

SCHLIEREN PHOTOGRAPH OF FLAT FACED BLUNT BODY (R/D = ∞) AT 4 DEGREES ANGLE OF YAW, M = 5.8.

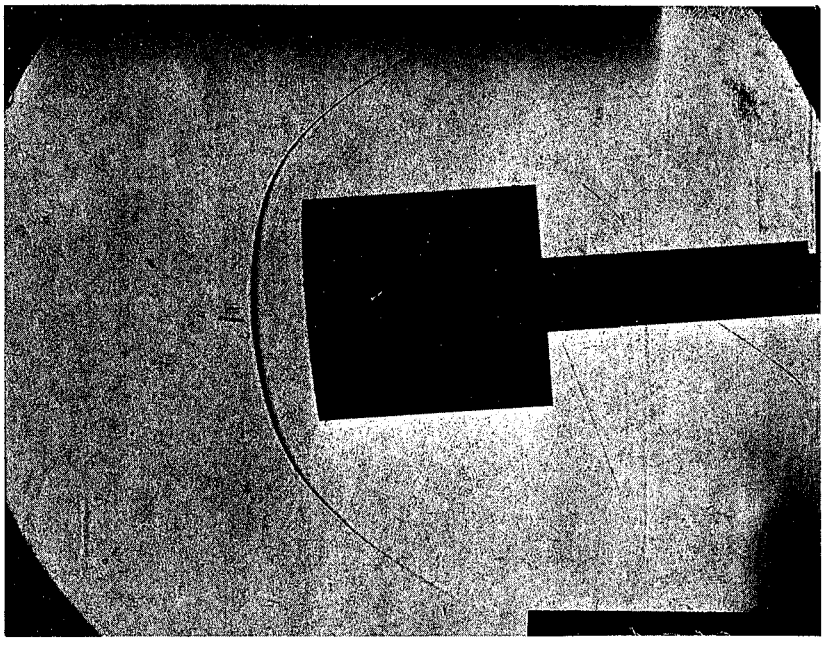

FIG. 21

SCHLIEREN PHOTOGRAPH OF ROUND NOSED BLUNT BODY (R/D = 5.733) AT 4 DEGREES ANGLE OF YAW, M = 5.8.

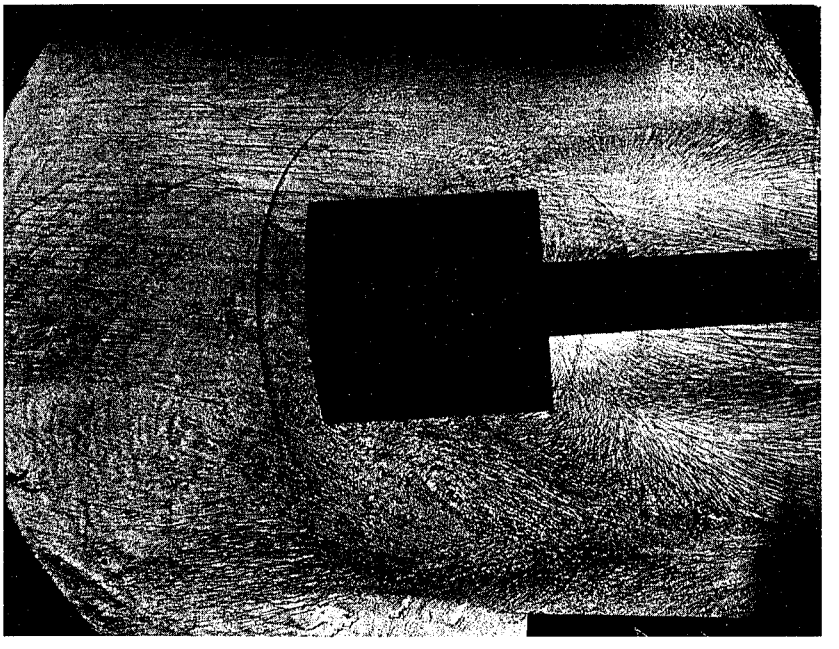

FIG. 22

SCHLIEREN PHOTOGRAPH OF ROUND NOSED BLUNT BODY (R/D = 2.880) AT 4 DEGREES ANGLE OF YAW, M = 5.8.

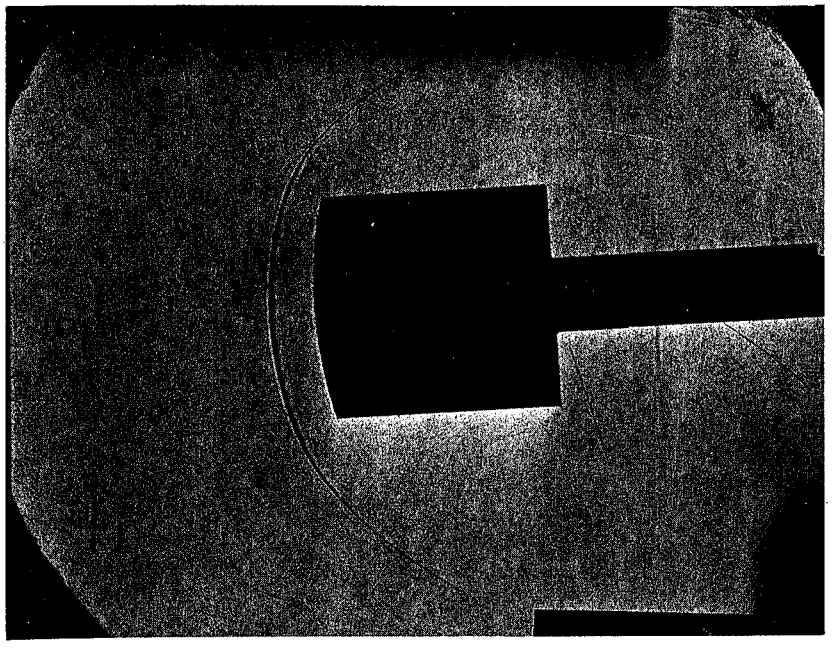

FIG. 23

SCHLIEREN PHOTOGRAPH OF ROUND NOSED BLUNT BODY (R/D = 1.907) AT 4 DEGREES ANGLE OF YAW, M = 5.8.

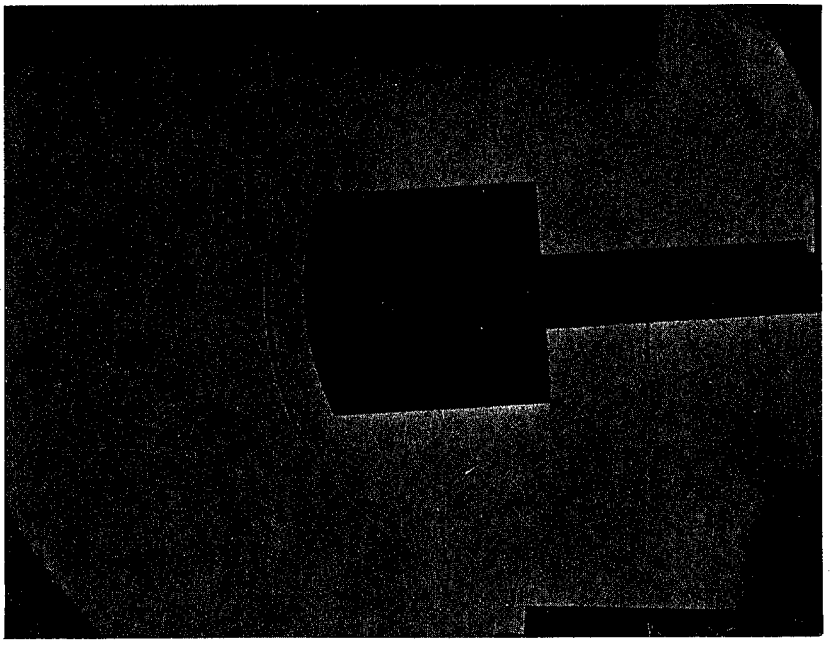

FIG. 24

SCHLIEREN PHOTOGRAPH OF ROUND NOSED BLUNT BODY (R/D = 1.300) AT 4 DEGREES ANGLE OF YAW, M = 5.8.

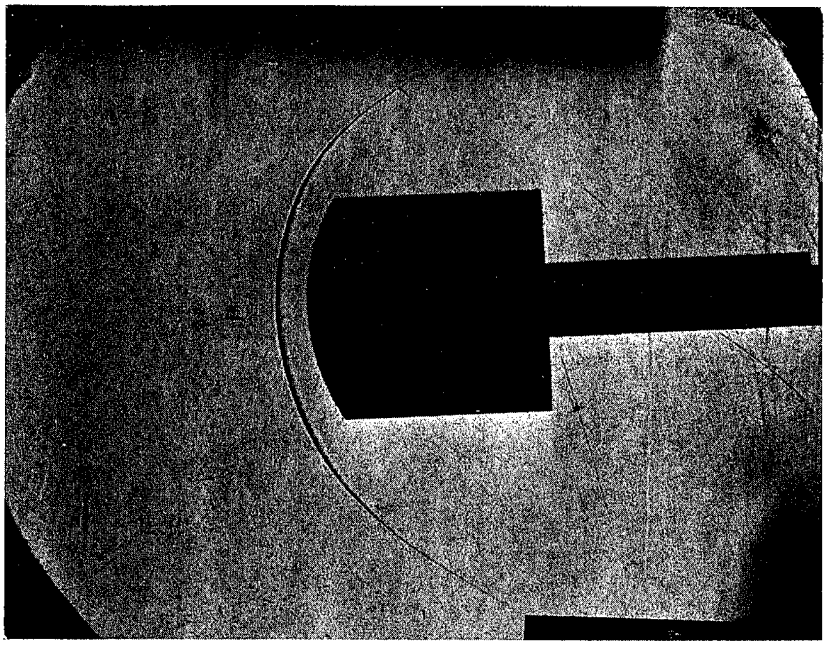

FIG. 25

SCHLIEREN PHOTOGRAPH OF ROUND NOSED BLUNT BODY (R/D = 0.920) AT 4 DEGREES ANGLE OF YAW, M = 5.8.

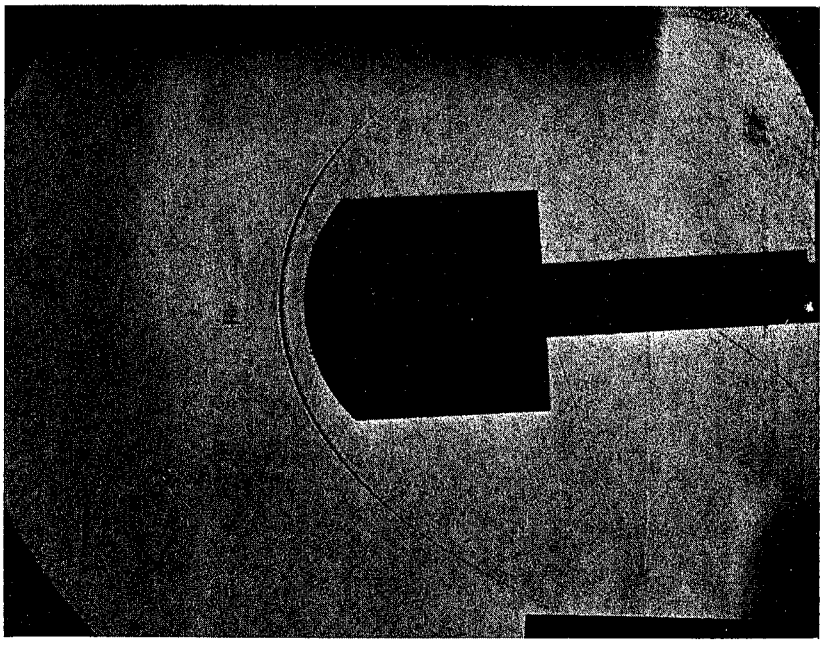

FIG. 26

SCHLIEREN PHOTOGRAPH OF ROUND NOSED BLUNT BODY (R/D = 0.727) AT 4 DEGREES ANGLE OF YAW, M = 5.8.

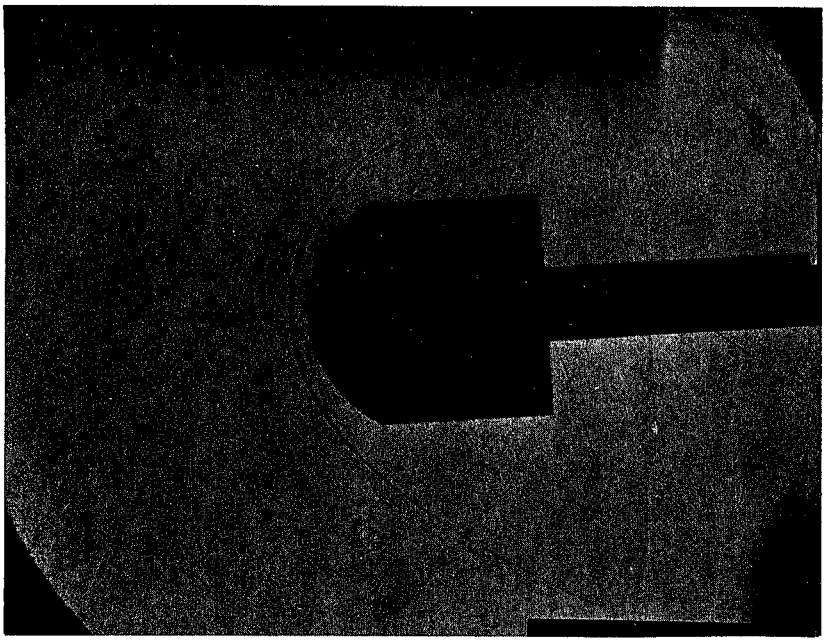

FIG. 27

SCHLIEREN PHOTOGRAPH OF ROUND NOSED BLUNT BODY (R/D = 0.567) AT 4 DEGREES ANGLE OF YAW, M = 5.8.

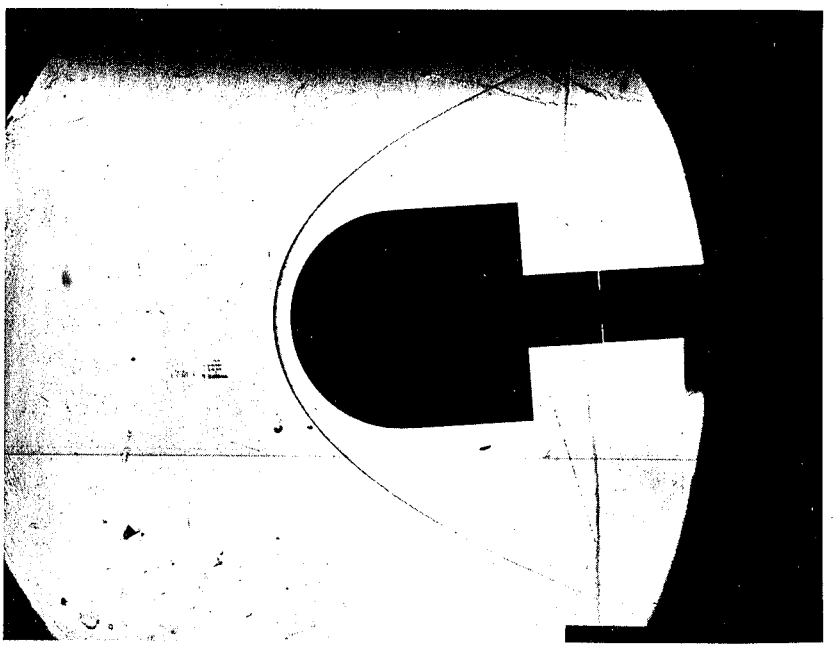

FIG. 28

SCHLIEREN PHOTOGRAPH OF ROUND NOSED BLUNT BODY (R/D = 0.500) (HEMISPHERE) AT 4 DEGREES ANGLE OF YA M = 5.8.

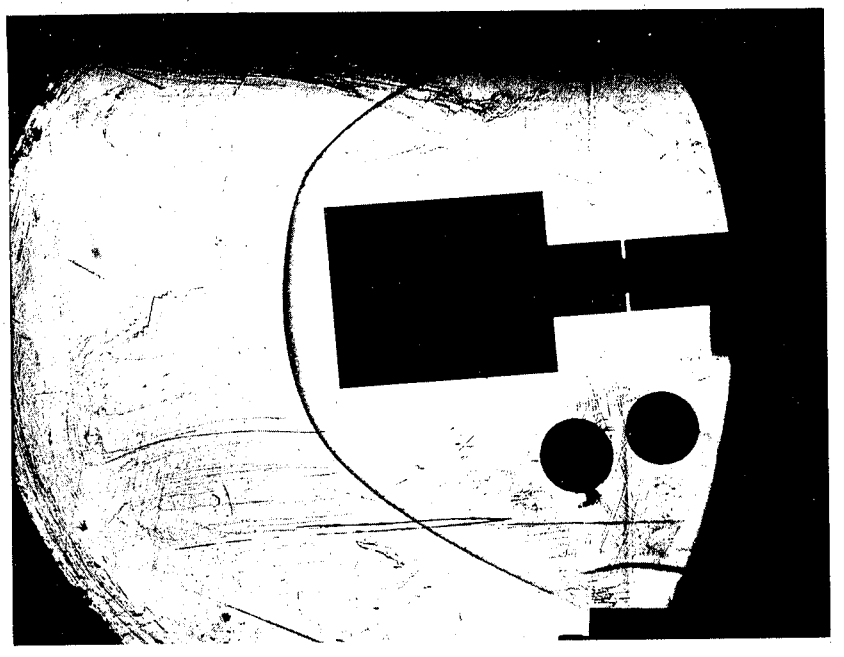

FIG. 29

SCHLIEREN PHOTOGRAPH OF CONCAVE NOSED BLUNT BODY (R/D = 0.800) AT 4 DEGREES ANGLE OF YAW, M = 5.8.

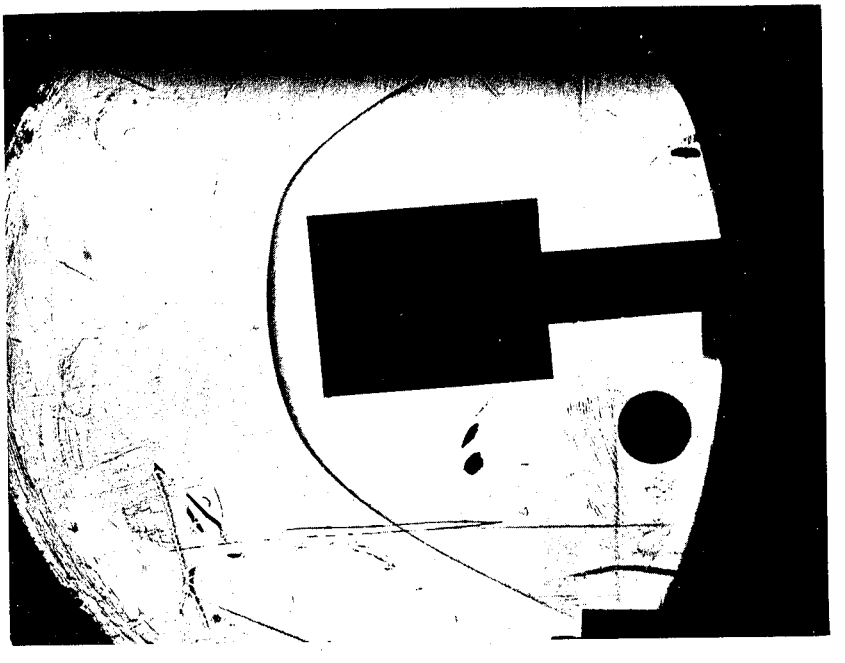

FIG. 30

SCHLIEREN PHOTOGRAPH OF CONCAVE NOSED BLUNT BODY (R/D = 1.600) AT 4 DEGREES ANGLE OF YAW, M = 5.8.

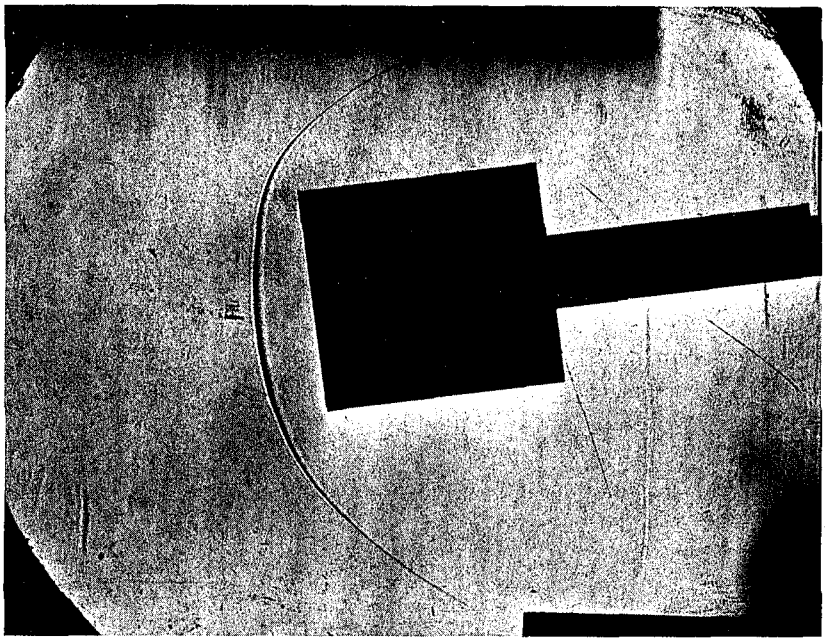

FIG. 31

SCHLIEREN PHOTOGRAPH OF FLAT FACED BLUNT BODY ($R/D = \infty$) AT 8 DEGREES ANGLE OF YAW, $M = 5.8$.

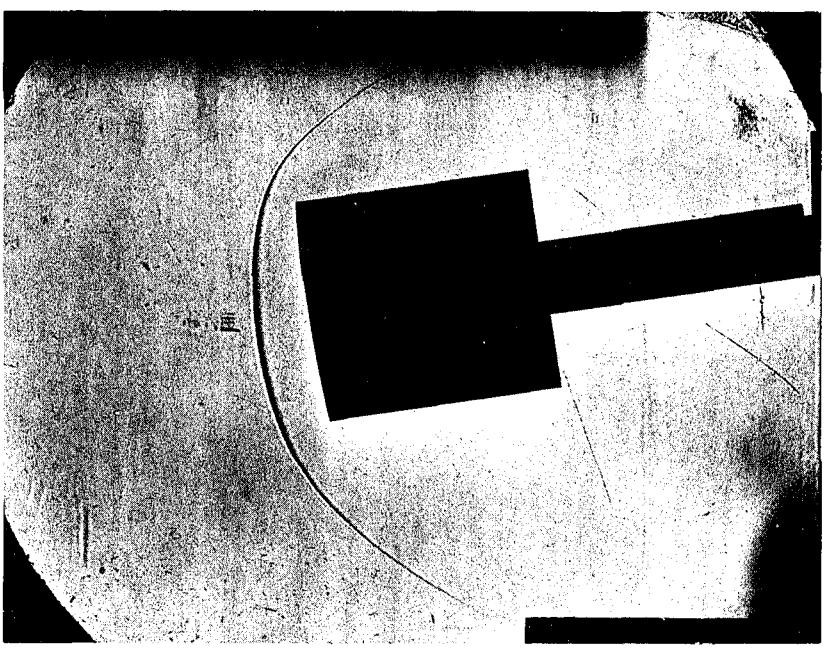

FIG. 32

SCHLIEREN PHOTOGRAPH OF ROUND NOSED BLUNT BODY ($R/D = 5.733$) AT 8 DEGREES ANGLE OF YAW, $M = 5.8$.

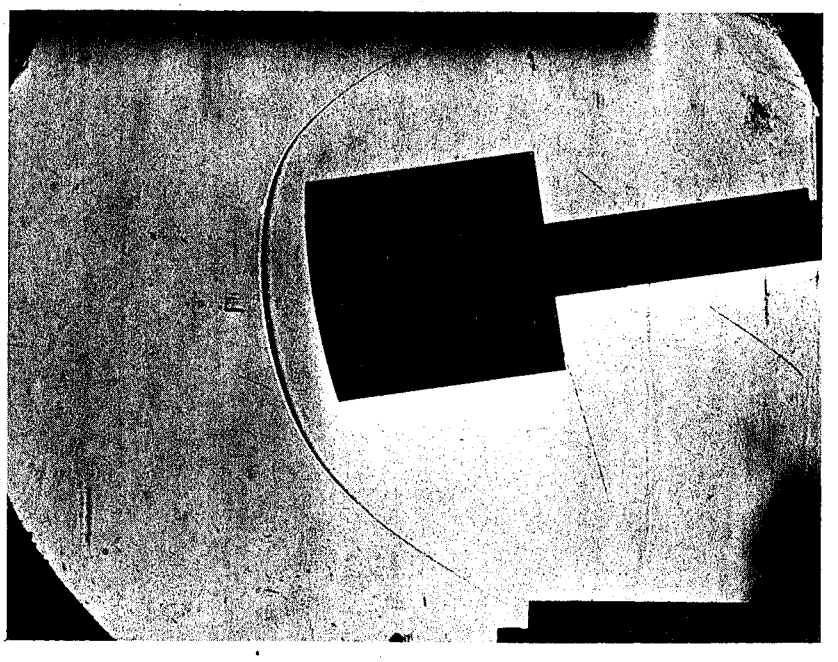

FIG. 33

SCHLIEREN PHOTOGRAPH OF ROUND NOSED BLUNT BODY (R/D = 2.880) AT 8 DEGREES ANGLE OF YAW, M = 5.8.

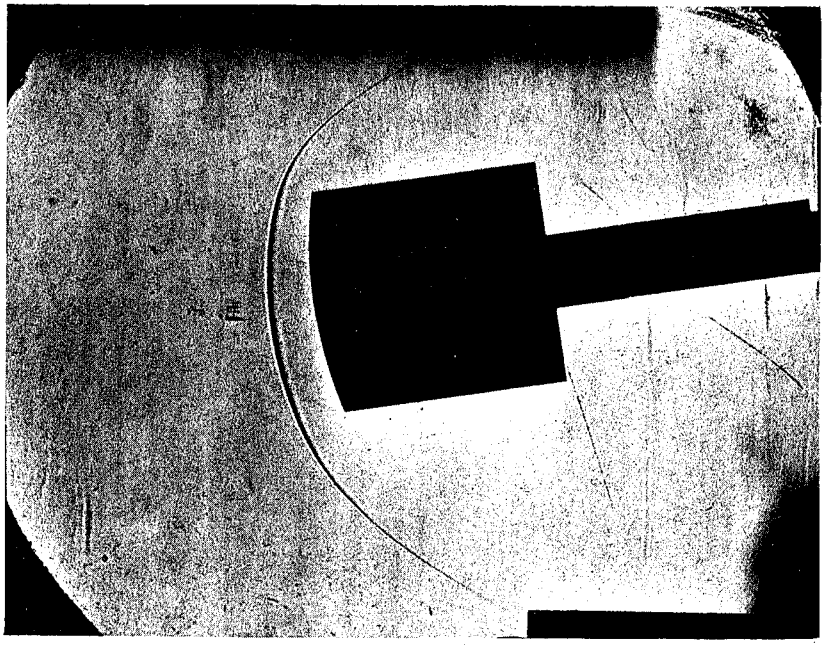

FIG. 34

SCHLIEREN PHOTOGRAPH OF ROUND NOSED BLUNT BODY (R/D = 1.907) AT 8 DEGREES ANGLE OF YAW, M = 5.8.

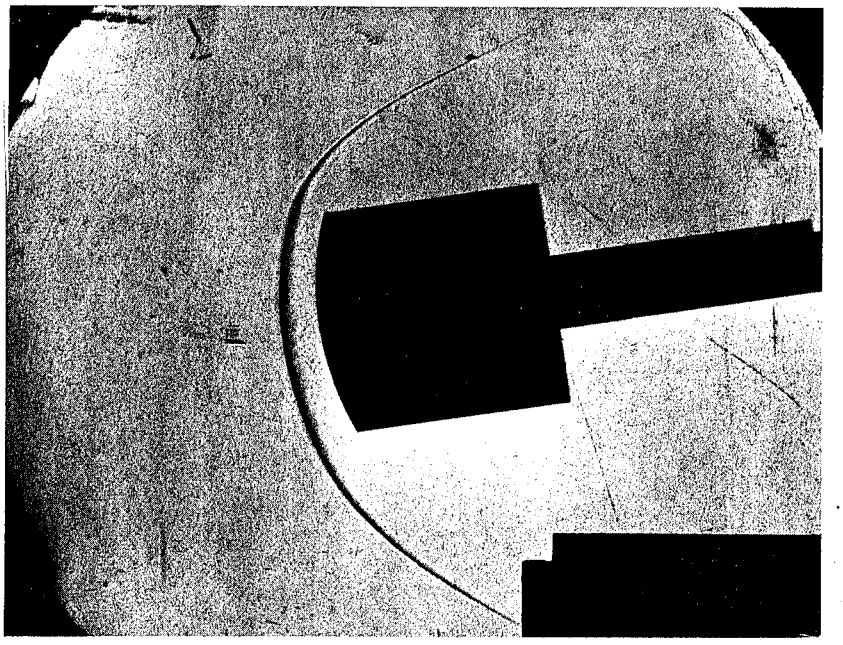

FIG. 35

SCHLIEREN PHOTOGRAPH OF ROUND NOSED BLUNT BODY (R/D = 1.300) AT 8 DEGREES ANGLE OF YAW, M = 5.8.

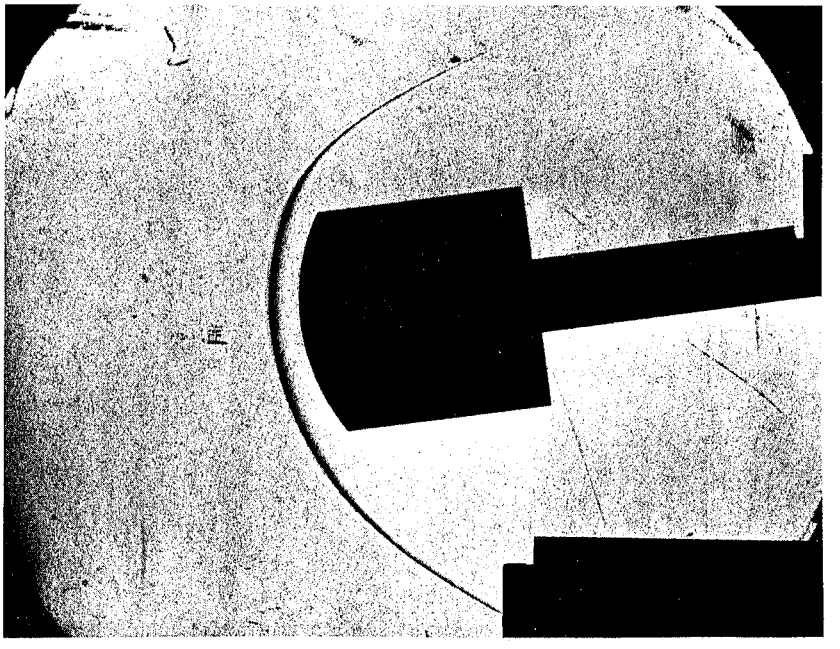

FIG. 36

SCHLIEREN PHOTOGRAPH OF ROUND NOSED BLUNT BODY (R/D = 0.920) AT 8 DEGREES ANGLE OF YAW, M = 5.8.

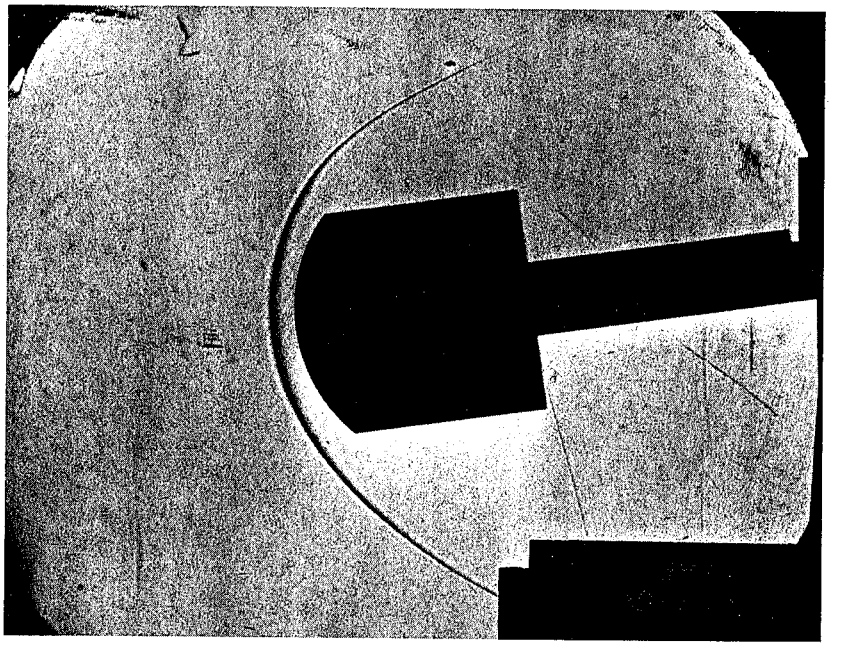

FIG. 37

SCHLIEREN PHOTOGRAPH OF ROUND NOSED BLUNT BODY (R/D = 0.727) AT 8 DEGREES ANGLE OF YAW, M = 5.8.

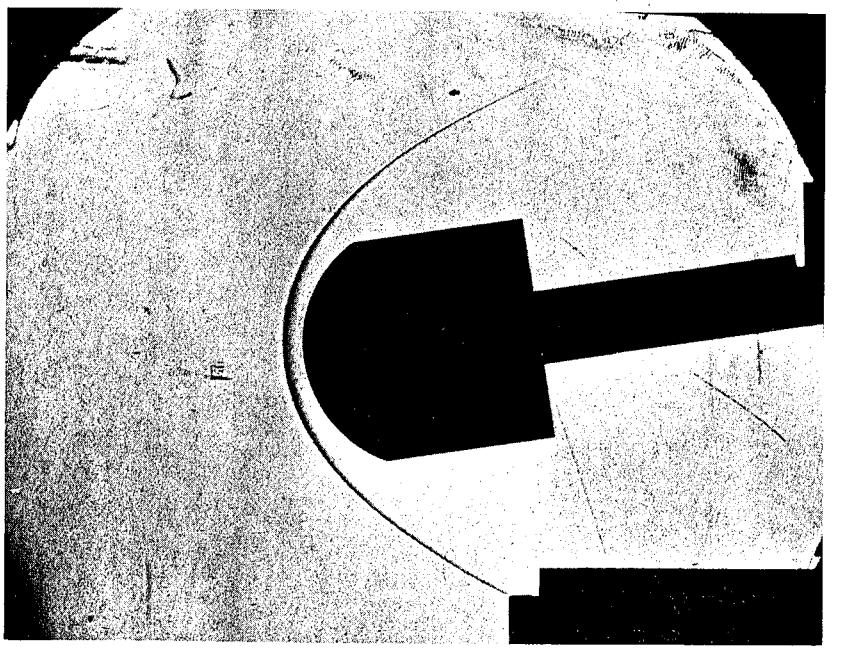

FIG. 38

SCHLIEREN PHOTOGRAPH OF ROUND NOSED BLUNT BODY (R/D = 0.567) AT 8 DEGREES ANGLE OF YAW, M = 5.8.

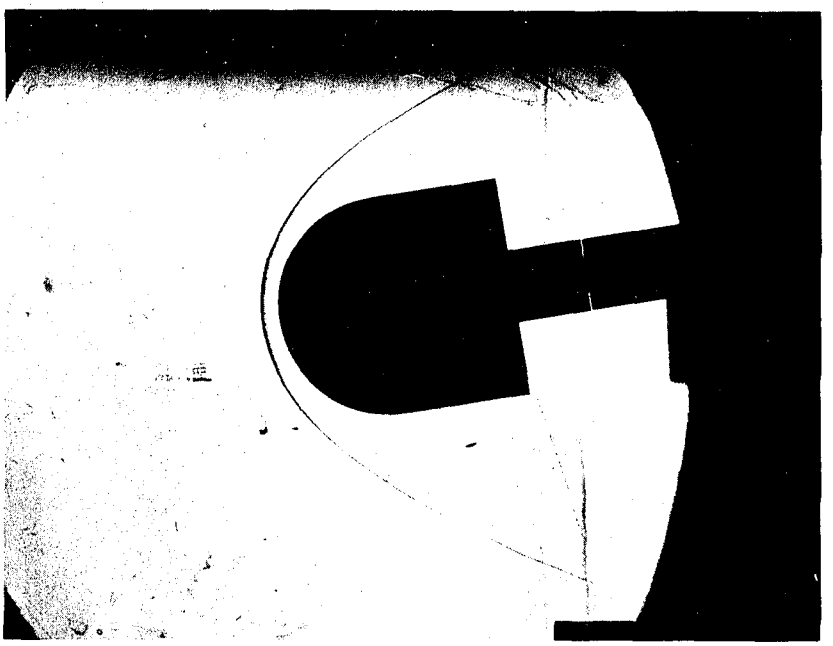

FIG. 39

SCHLIEREN PHOTOGRAPH OF ROUND NOSED BLUNT BODY (R/D = 0.500) (HEMISPHERE) AT 8 DEGREES ANGLE OF YAW M = 5.8.

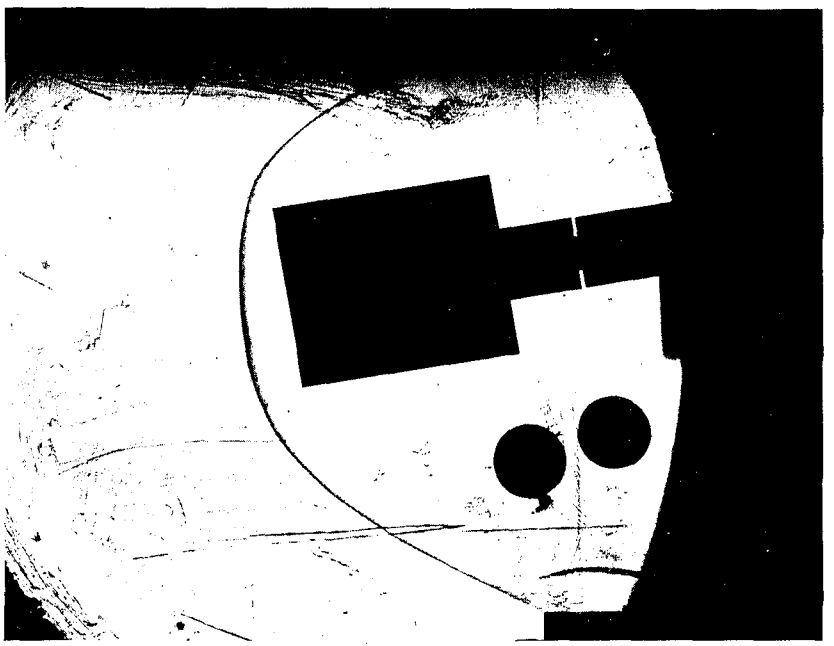

FIG. 40

SCHLIEREN PHOTOGRAPH OF CONCAVE NOSED BLUNT BODY (R/D = 0.800) AT 8 DEGREES ANGLE OF YAW, M = 5.8.

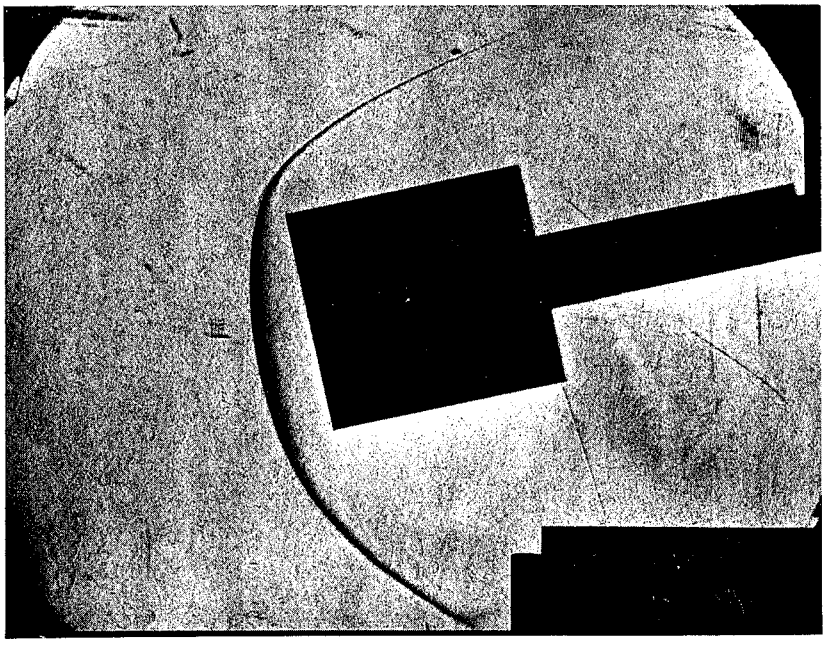

FIG. 41

SCHLIEREN PHOTOGRAPH OF FLAT FACED BLUNT BODY ($R/D = \infty$) AT 12 DEGREES ANGLE OF YAW, M = 5.8.

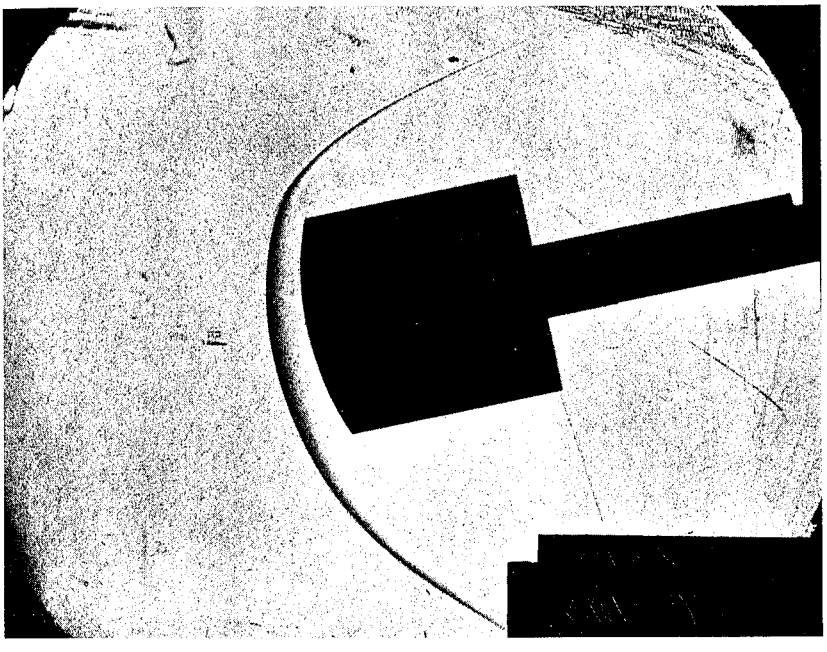

FIG. 42

SCHLIEREN PHOTOGRAPH OF ROUND NOSED BLUNT BODY (R/D) = 1.300 AT 12 DEGREES ANGLE OF YAW, M = 5.8.

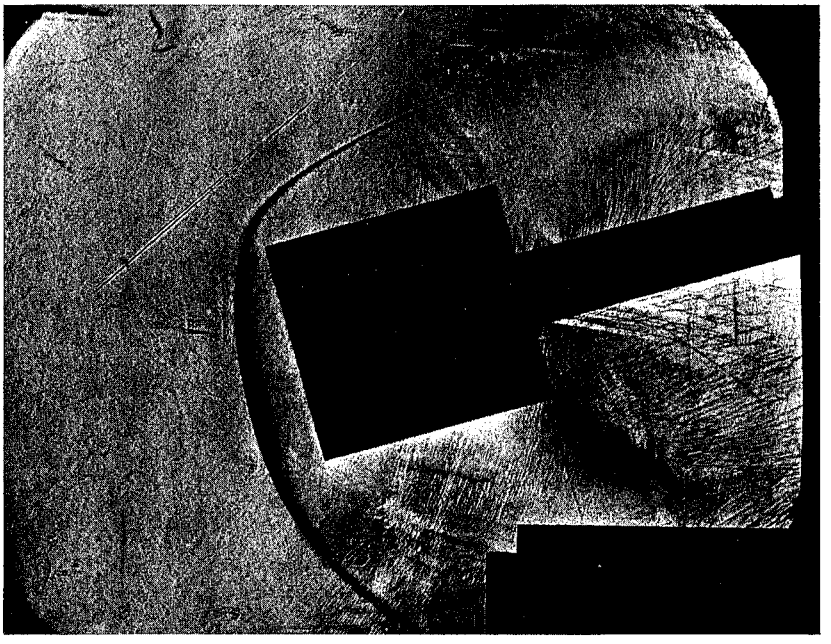

FIG. 43

SCHLIEREN PHOTOGRAPH OF FLAT FACED BLUNT BODY ($R/D = \infty$) AT 16 DEGREES ANGLE OF YAW, $M = 5.8$.

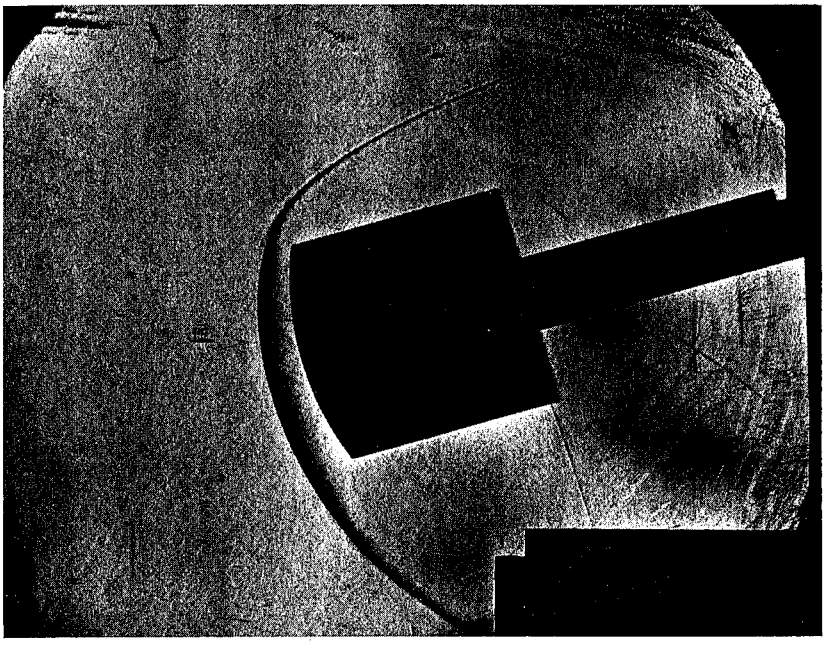

FIG. 44

SCHLIEREN PHOTOGRAPH OF ROUND NOSED BLUNT BODY ($R/D = 1.300$) AT 16 DEGREES ANGLE OF YAW, $M = 5.8$.

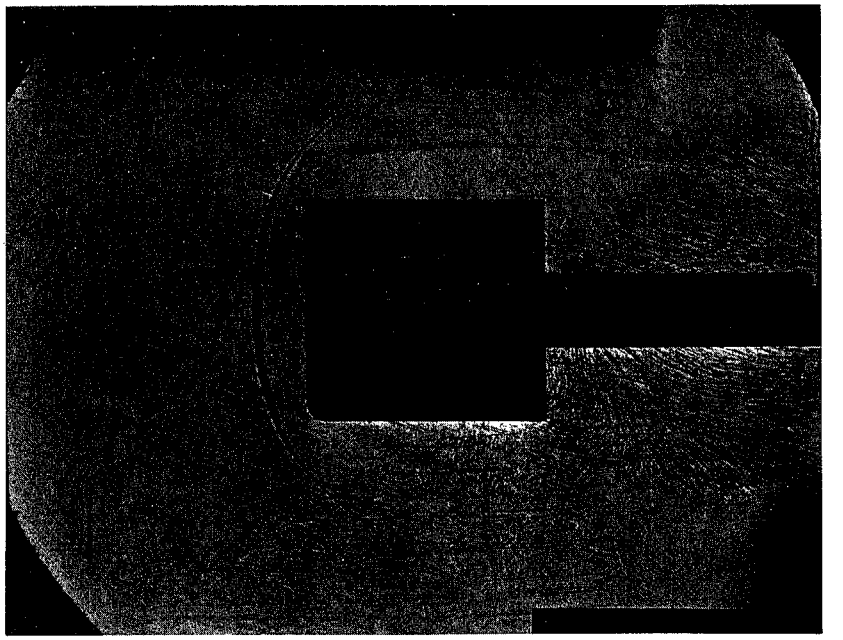

FIG. 45

SCHLIEREN PHOTOGRAPH OF FLAT FACED BLUNT BODY
(R/D = ∞) WITH 1/8 INCH ROUNDED SHOULDER (R/D = 0.083)
AT ZERO DEGREES ANGLE OF YAW, M = 5.8.

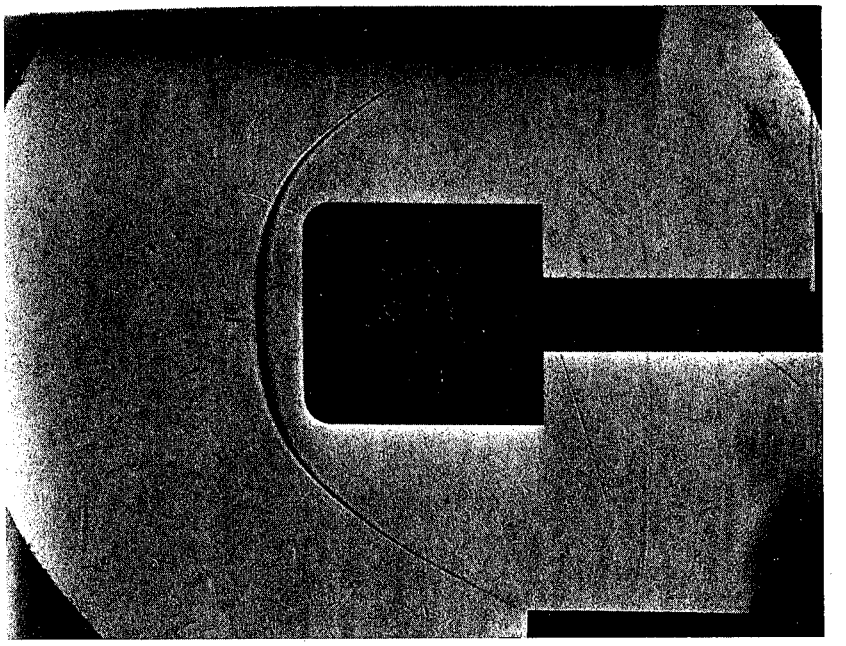

FIG. 46

SCHLIEREN PHOTOGRAPH OF FLAT FACED BLUNT BODY
(R/D = ∞) WITH 3/16 INCH ROUNDED SHOULDER (r/D = 0.125)
AT ZERO DEGREES ANGLE OF YAW, M = 5.8.

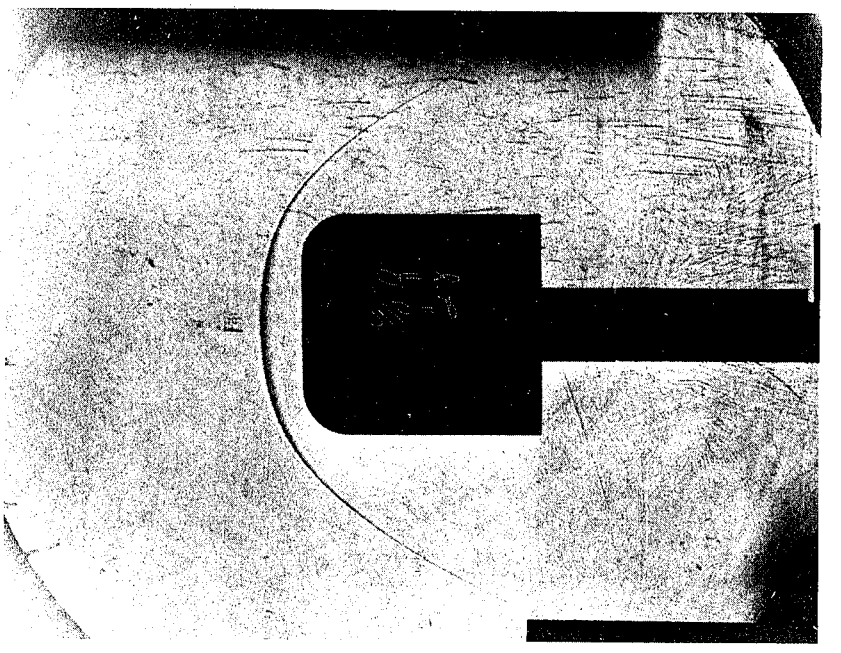

FIG. 47

SCHLIEREN PHOTOGRAPH OF FLAT FACED BLUNT BODY (R/D = ∞) WITH 5/16 INCH ROUNDED SHOULDER (r/D = 0.208) AT ZERO DEGREES ANGLE OF YAW, M = 5.8.

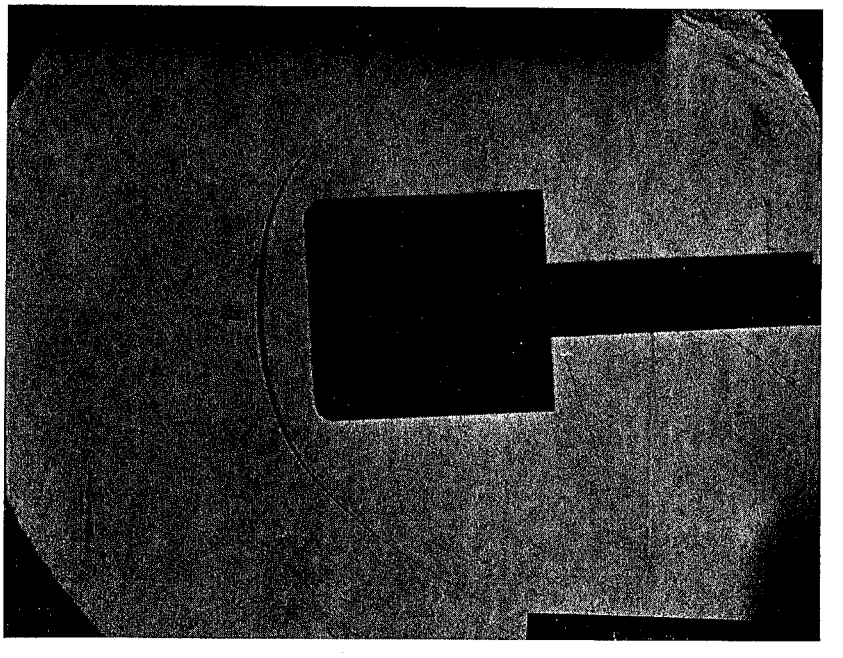

FIG. 48

SCHLIEREN PHOTOGRAPH OF FLAT FACED BLUNT BODY (R/D = ∞) WITH 1/8 INCH ROUNDED SHOULDER (r/D = 0.083) AT 4 DEGREES ANGLE OF YAW, M = 5.8.

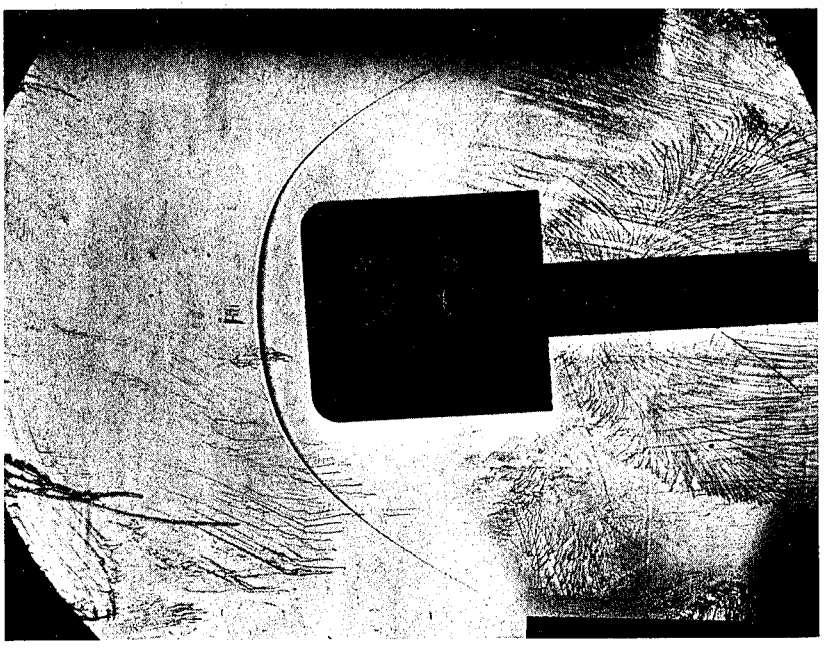

FIG. 49

SCHLIEREN PHOTOGRAPH OF FLAT FACED BLUNT BODY (R/D = ∞) WITH 3/16 INCH ROUNDED SHOULDER (r/D = 0.125) AT 4 DEGREES ANGLE OF YAW, M = 5.8.

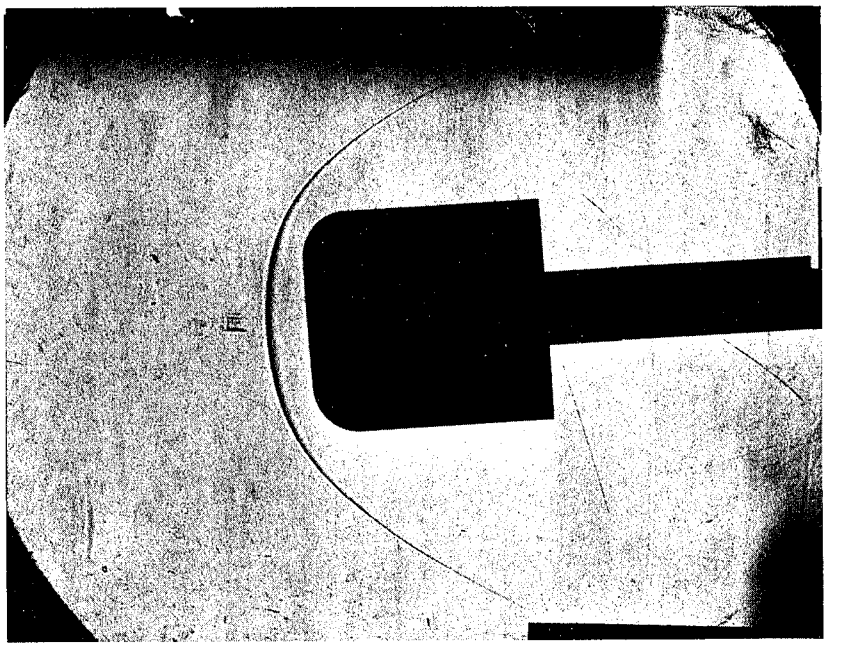

FIG. 50

SCHLIEREN PHOTOGRAPH OF FLAT FACED BLUNT BODY (R/D = ∞) WITH 5/16 INCH ROUNDED SHOULDER (r/D = 0.208) AT 4 DEGREES ANGLE OF YAW, M = 5.8.

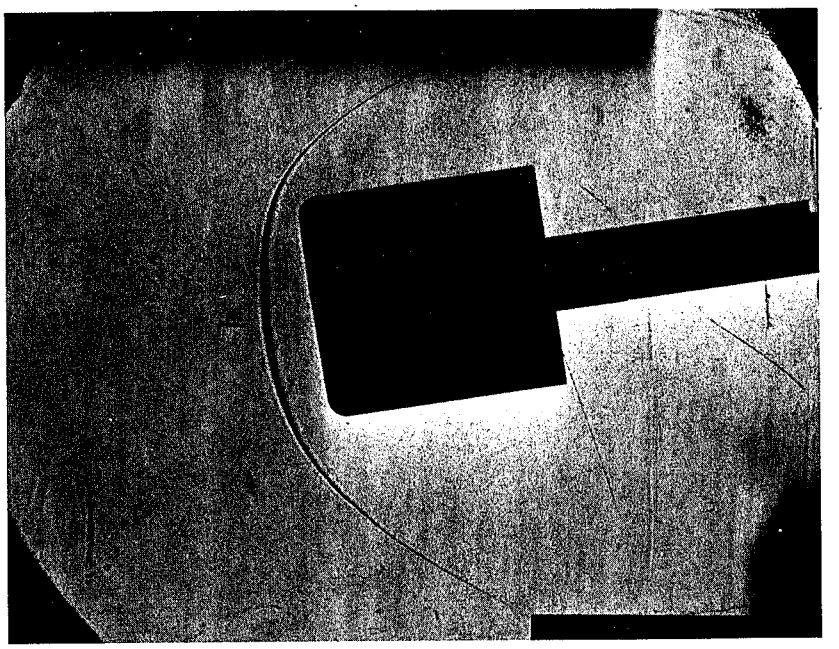

FIG. 51

SCHLIEREN PHOTOGRAPH OF FLAT FACED BLUNT BODY
(R/D = ∞) WITH 1/8 INCH ROUNDED SHOULDER (r/D = 0.083)
AT 8 DEGREES ANGLE OF YAW, M = 5.8.

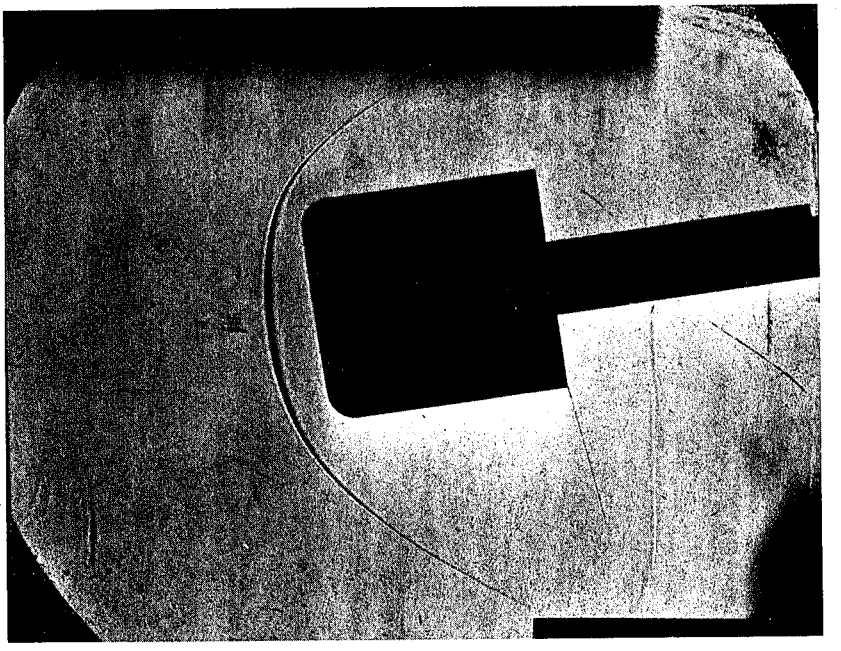

FIG. 52

SCHLIEREN PHOTOGRAPH OF FLAT FACED BLUNT BODY
(R/D = ∞) WITH 3/16 INCH ROUNDED SHOULDER (r/D = 0.125)
AT 8 DEGREES ANGLE OF YAW, M = 5.8.

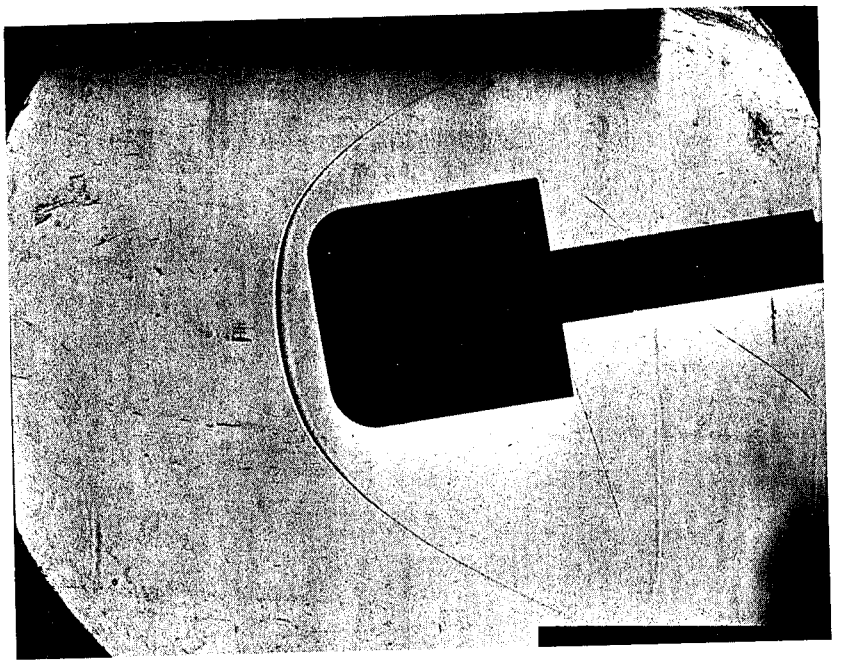

FIG. 53

SCHLIEREN PHOTOGRAPH OF FLAT FACED BLUNT BODY ($R/D = \infty$) WITH 5/16 INCH ROUNDED SHOULDER ($r/D = 0.208$) AT 8 DEGREES ANGLE OF YAW, $M = 5.8$.

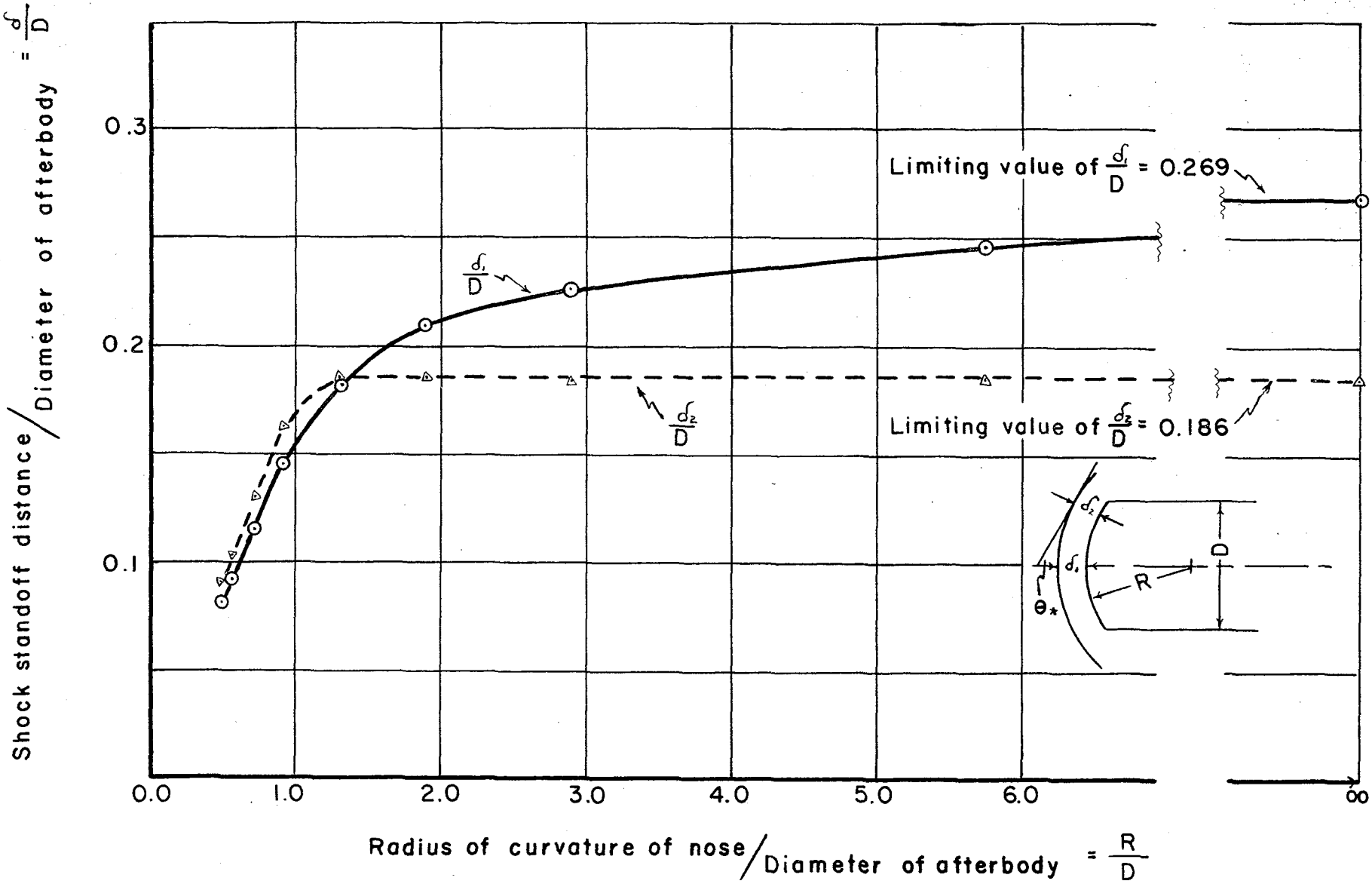

FIG. 54. SHOCK STANDOFF DISTANCE vs. NOSE RADIUS

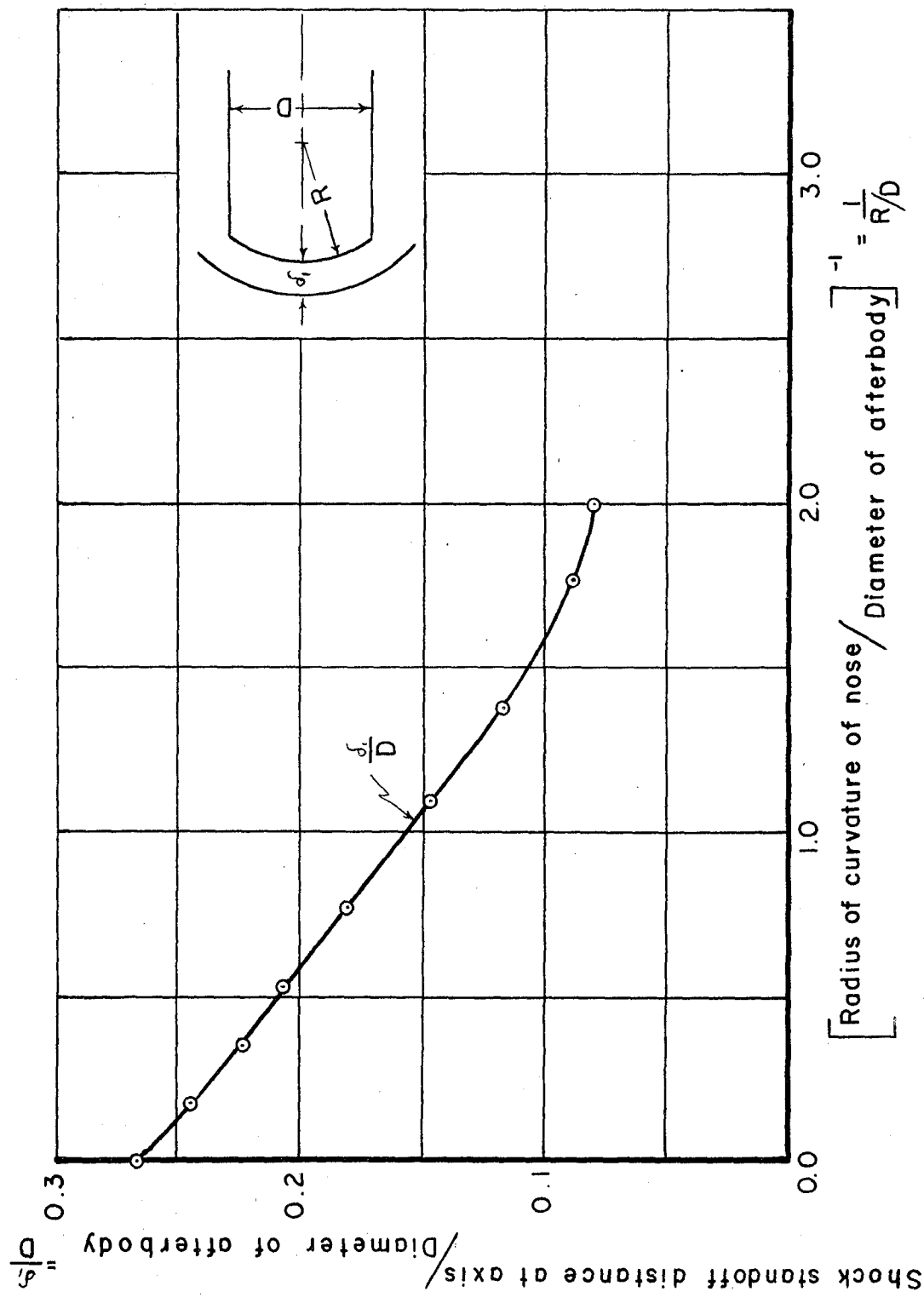

FIG.55. SHOCK STANDOFF DISTANCE vs. RECIPROCAL OF NOSE RADIUS

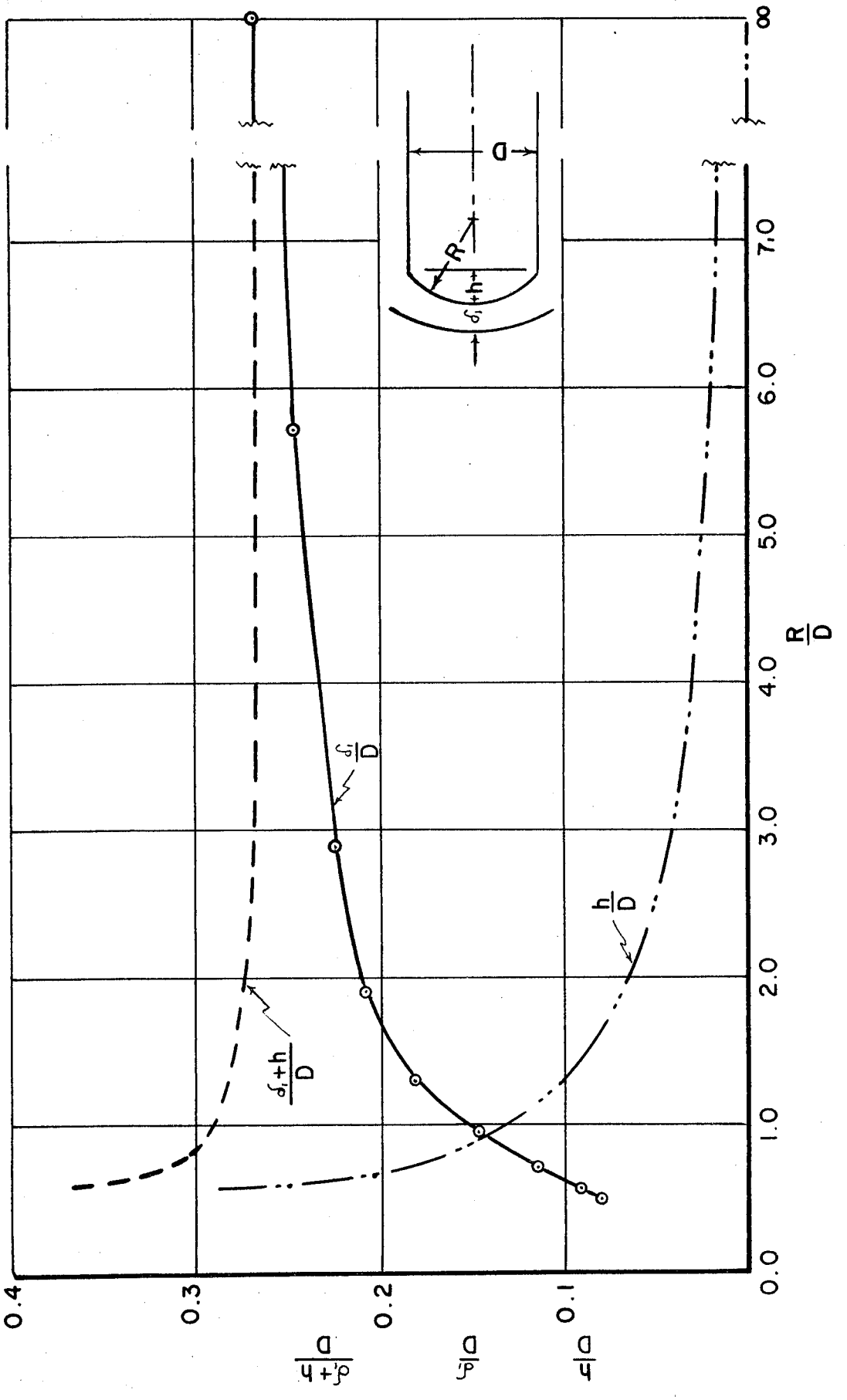

FIG. 56. EFFECT OF ADDING STANDOFF DISTANCE TO NOSE RISE

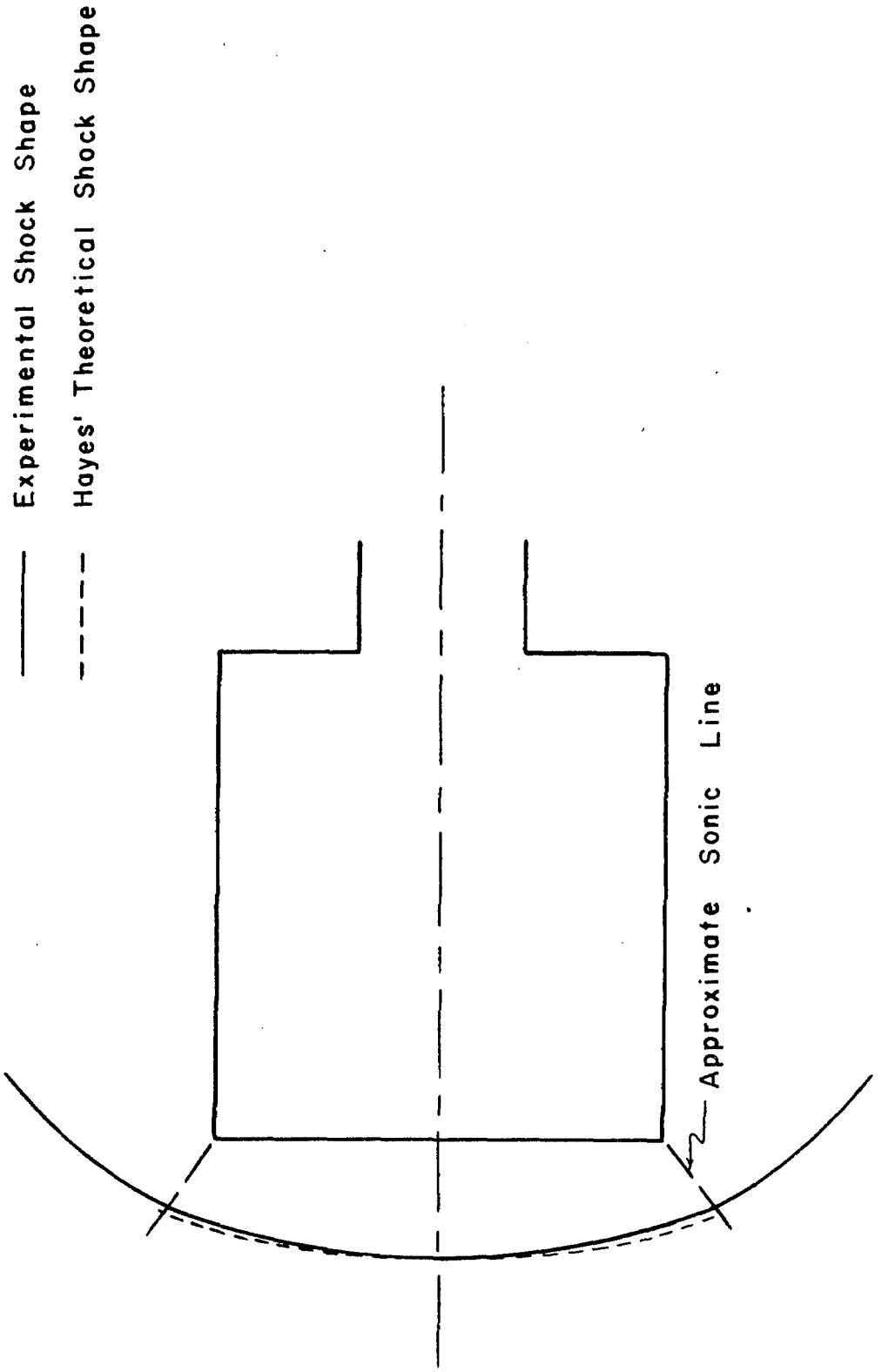

FIG. 57. COMPARISON OF EXPERIMENTAL SHOCK SHAPE WITH HAYES' THEORETICAL APPROXIMATION, $R/D=\infty$, $\alpha = 0$.

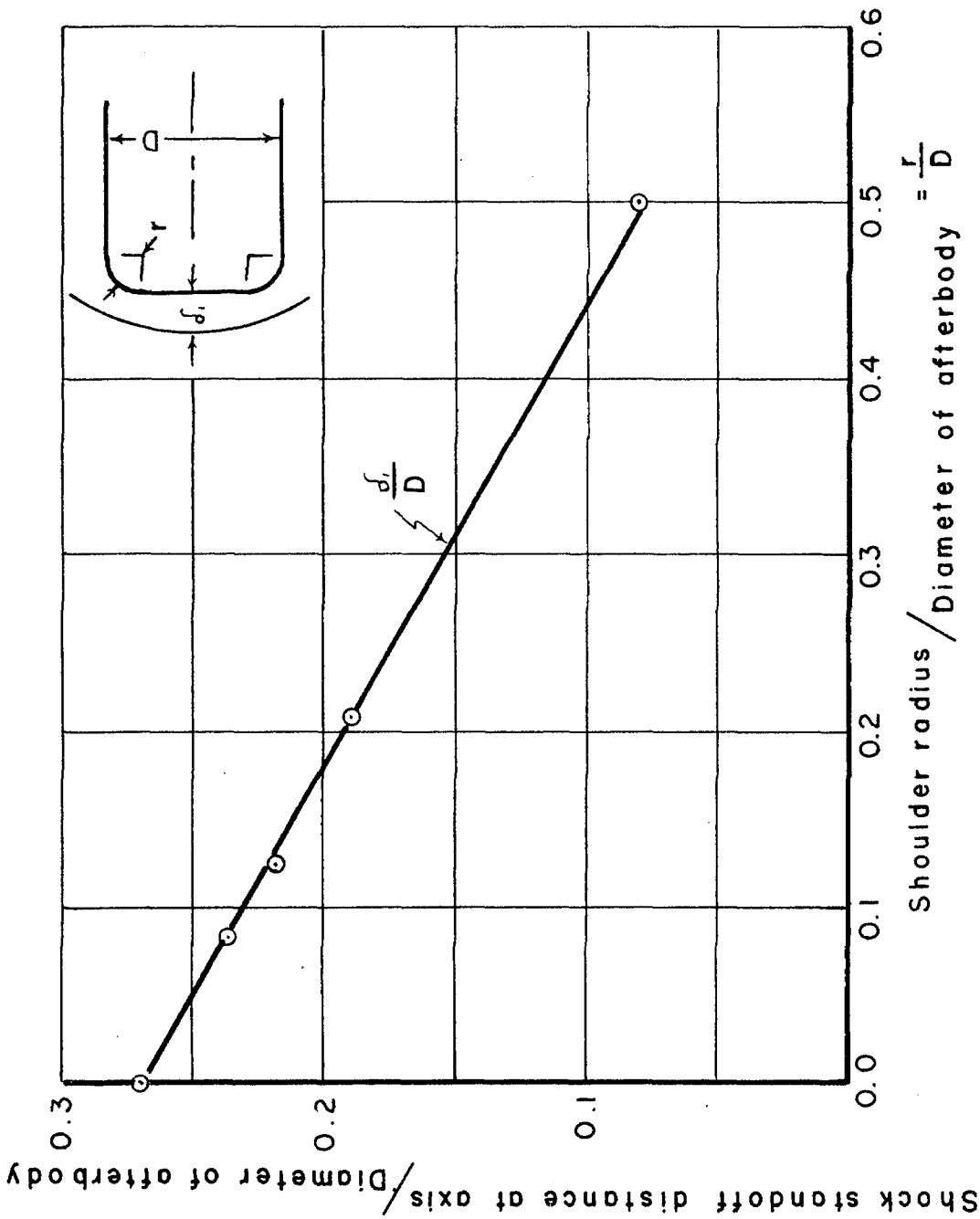

FIG.58. SHOCK STANDOFF DISTANCE vs. SHOULDER RADIUS

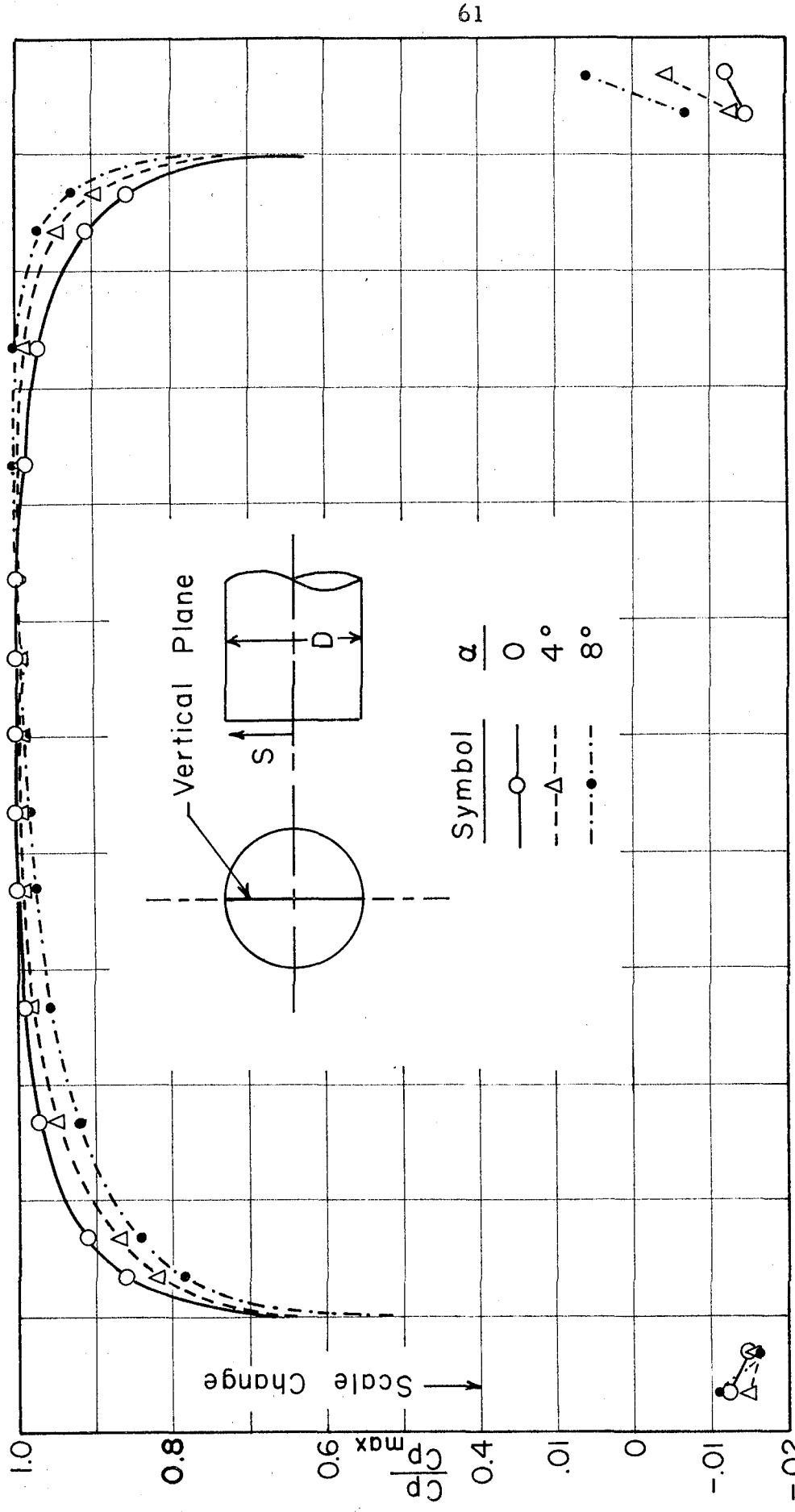

FIG. 59. SURFACE PRESSURE, VERTICAL PLANE, $\frac{R}{D} = \infty$, $\alpha = 0, 4°, 8°$.

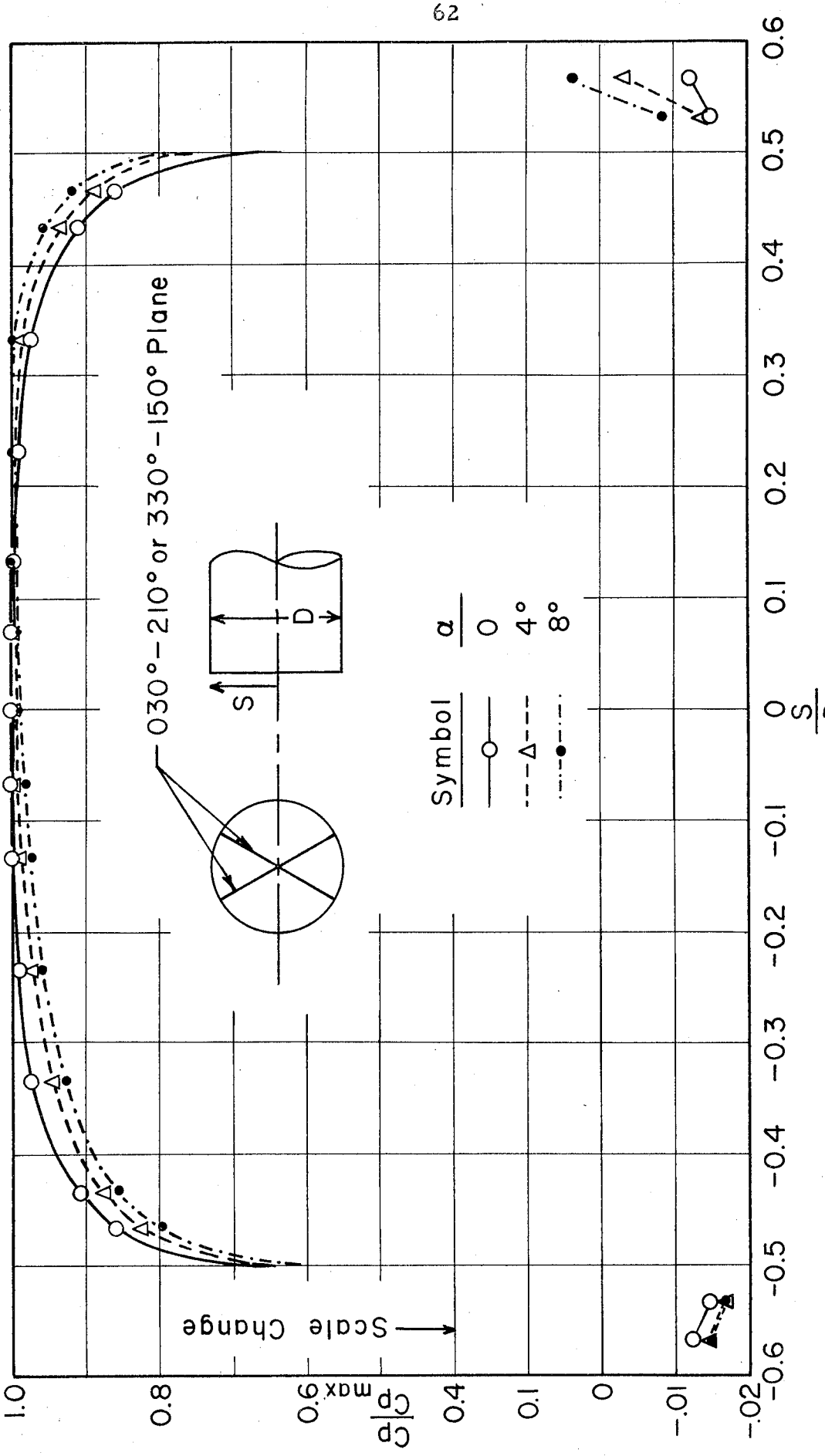

FIG. 60. SURFACE PRESSURE 030°–210° PLANE, $\frac{R}{D} = \infty$, $\alpha = 0, 4°, 8°$.

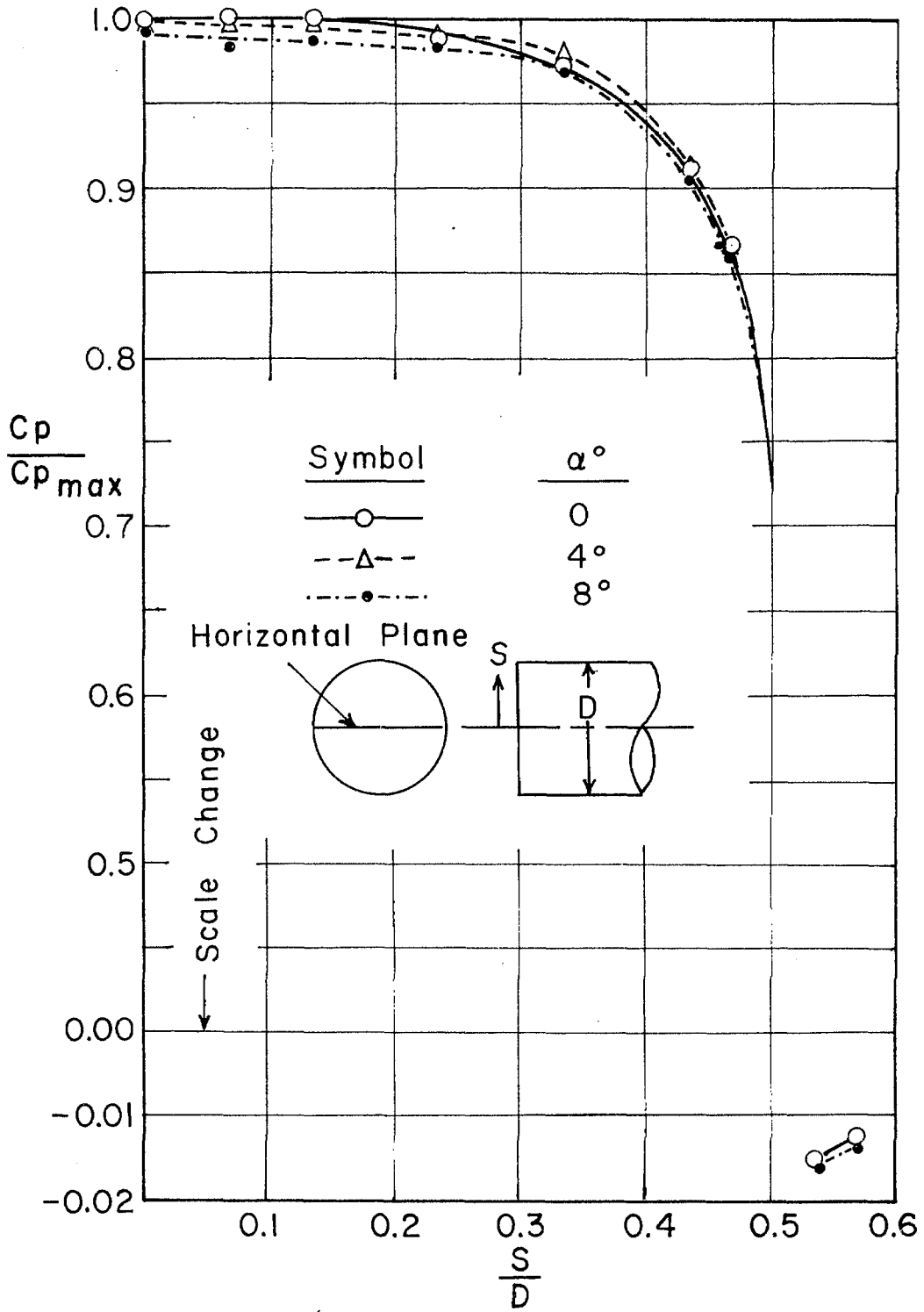

FIG. 61. SURFACE PRESSURES, HORIZONTAL PLANE, R/D = ∞, α = 0°, 4° & 8°.

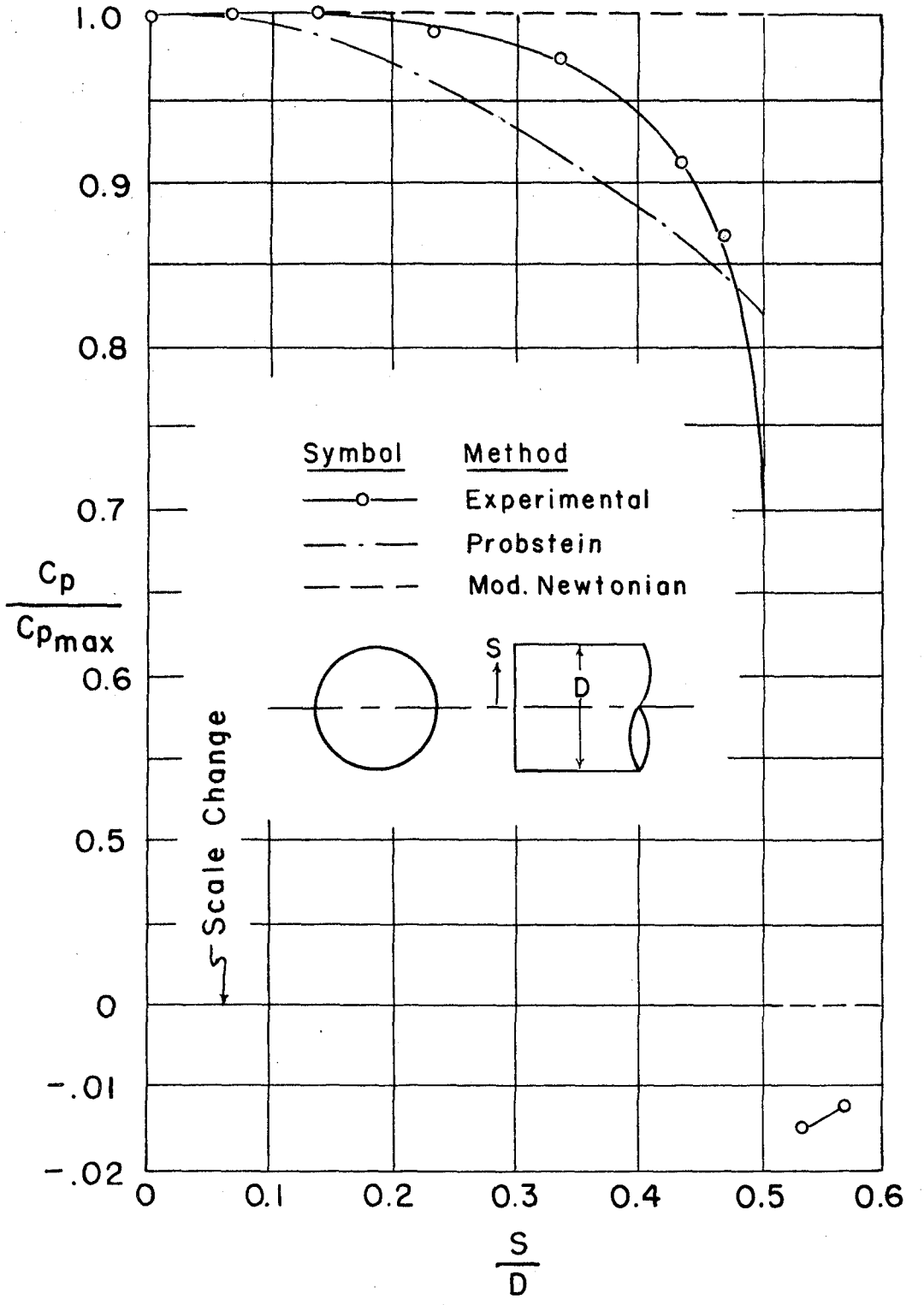

FIG. 62. COMPARISON OF EXPERIMENTAL SURFACE PRESSURE DISTRIBUTION WITH THEORETICAL APPROXIMATIONS, $R/D = \infty$, $\alpha = 0$.

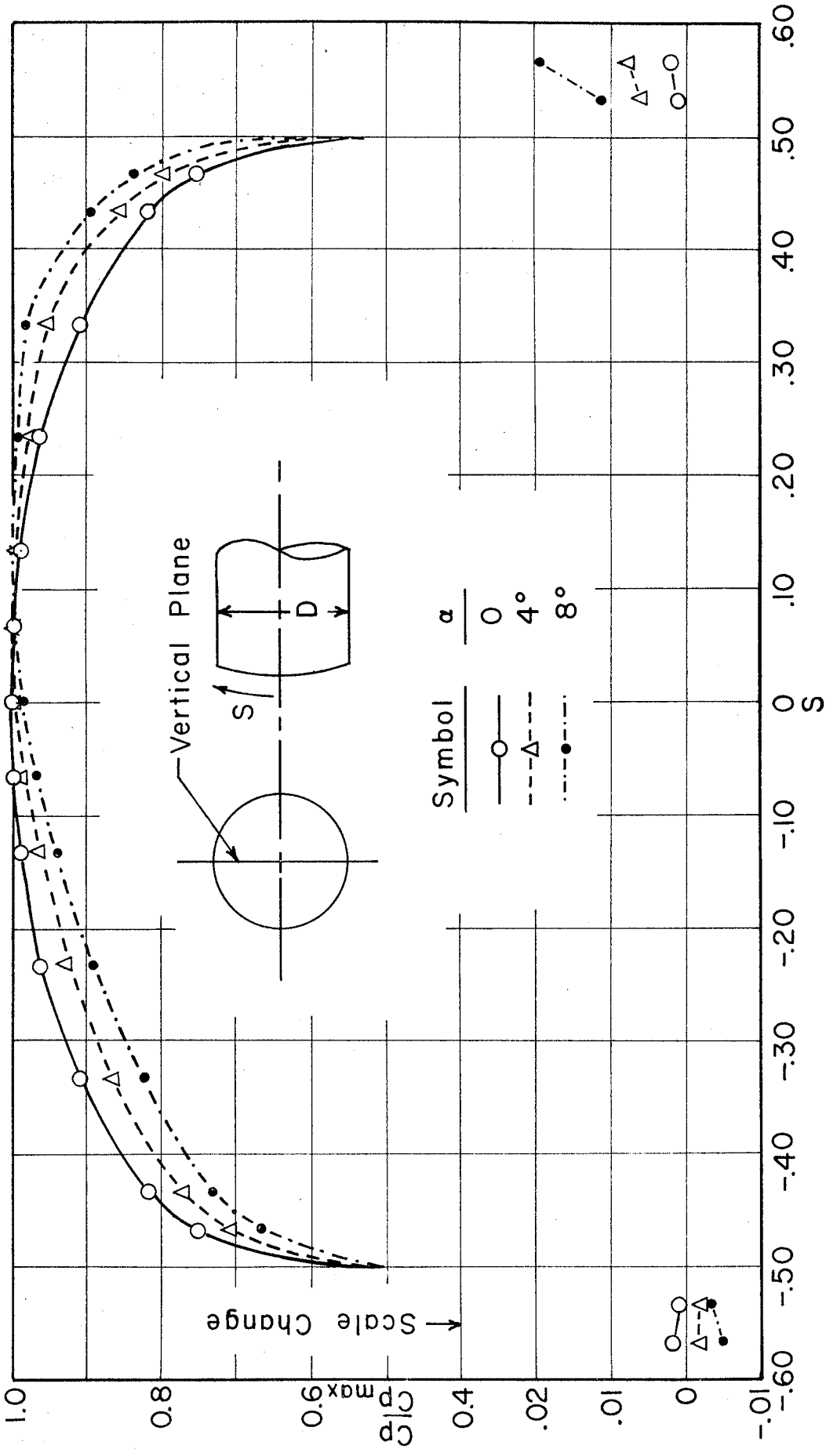

FIG. 63. SURFACE PRESSURE, VERTICAL PLANE, $\frac{R}{D} = 1.3$, $\alpha = 0, 4°, 8°$

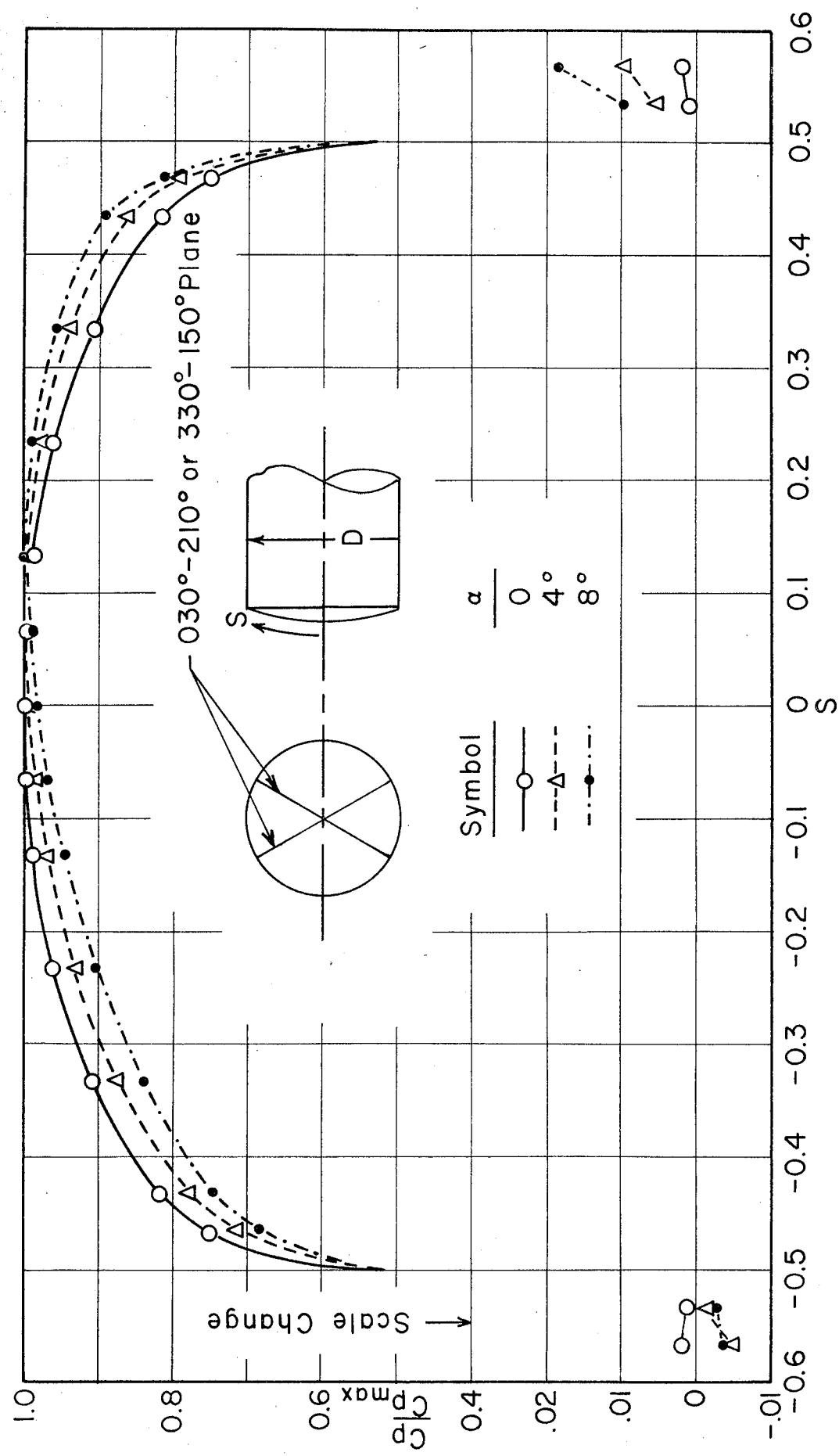

FIG. 64. SURFACE PRESSURES 030° – 210°, $\frac{R}{D}$ = 1.30, α = 0, 4°, 8°

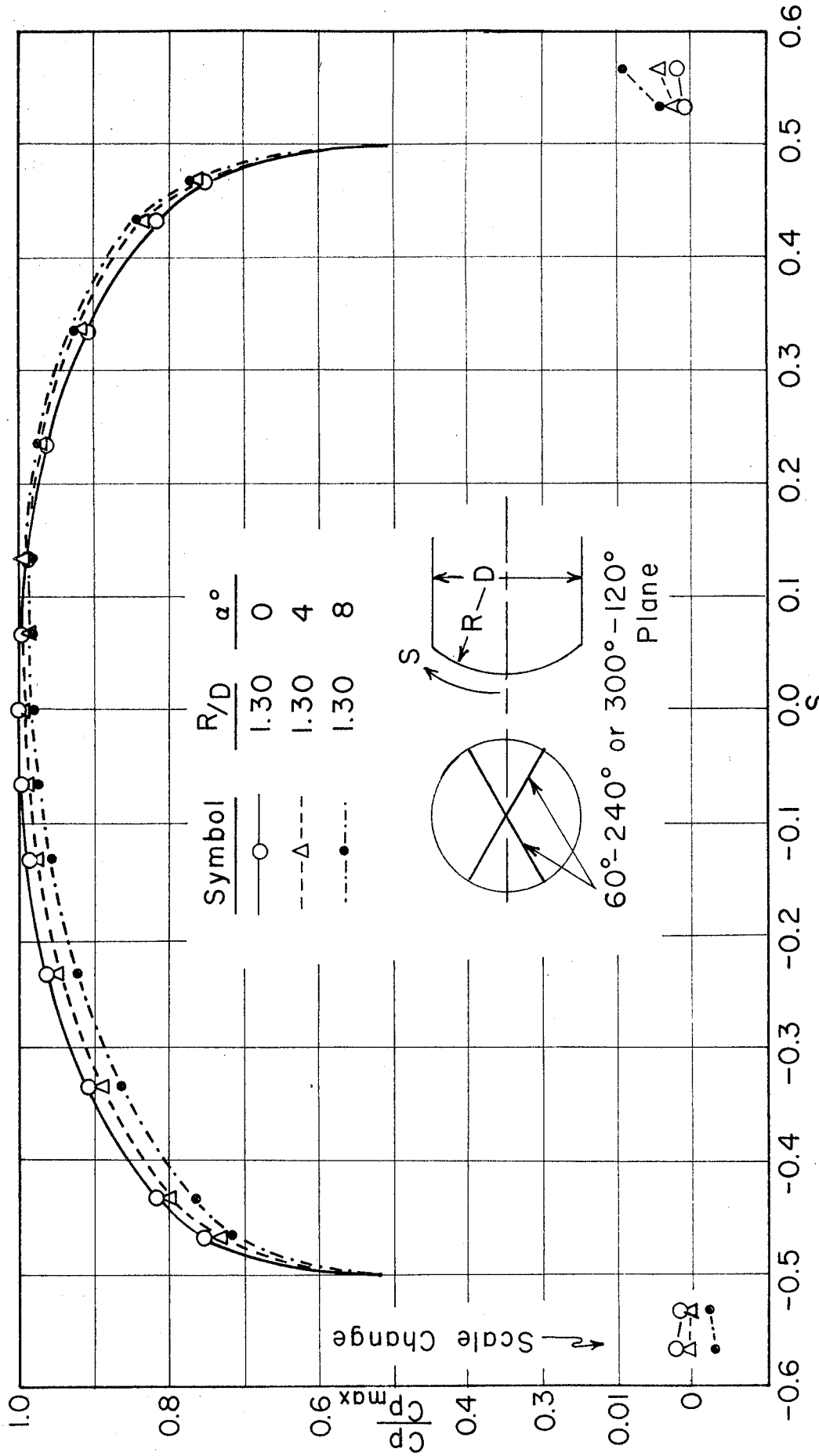

FIG. 65. SURFACE PRESSURES, 60°-240° PLANE, $\frac{R}{D} = 1.30$, $\alpha = 0°, 4° \& 8°$

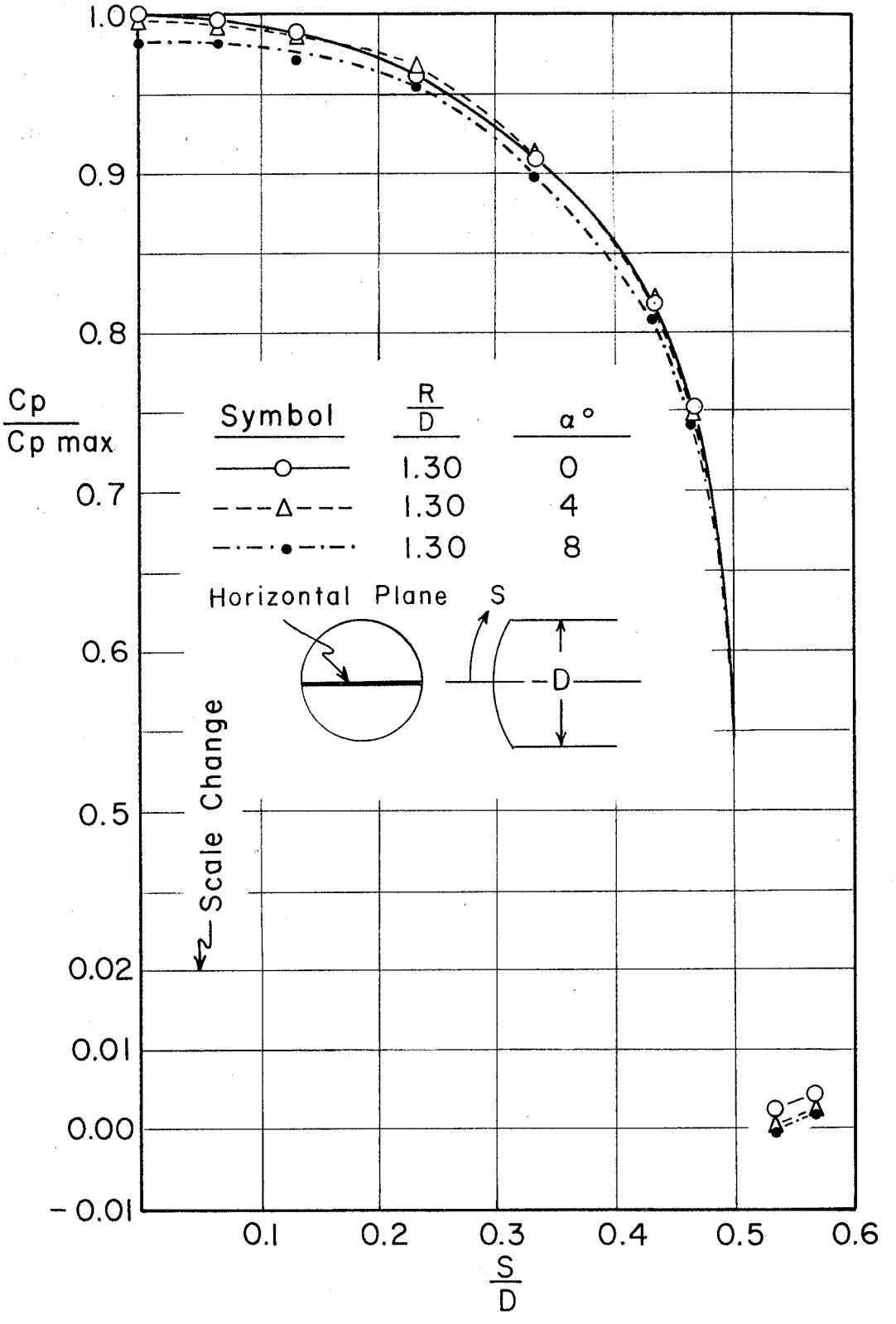

FIG. 66. SURFACE PRESSURE, HORIZONTAL PLANE, R/D = 1.30, α = 0°, 4° & 8°

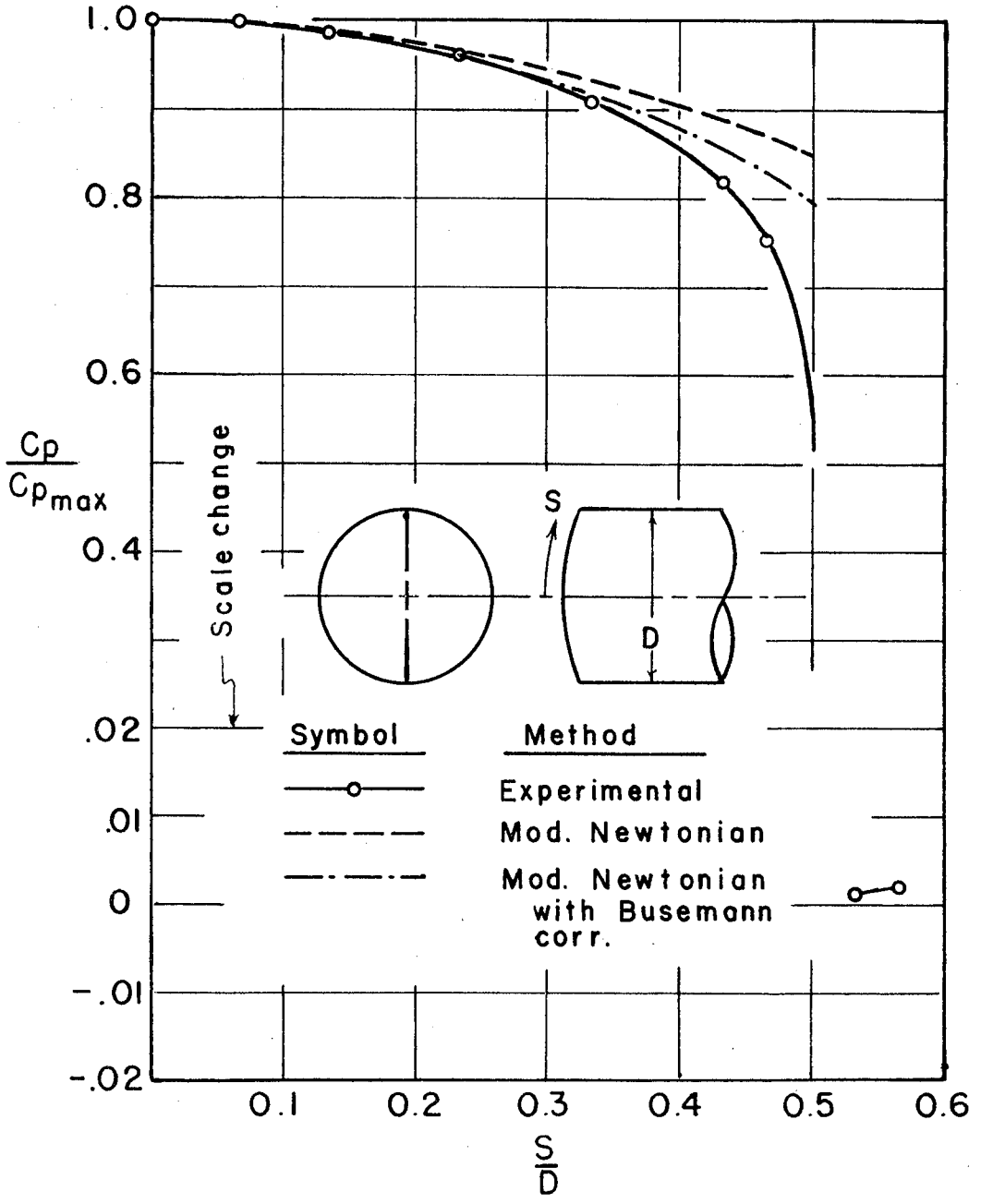

FIG. 67. COMPARISON OF EXPERIMENTAL SURFACE PRESSURE DISTRIBUTION WITH THEORETICAL APPROXIMATIONS, $\frac{R}{D}=1.30$, $\alpha=0$.

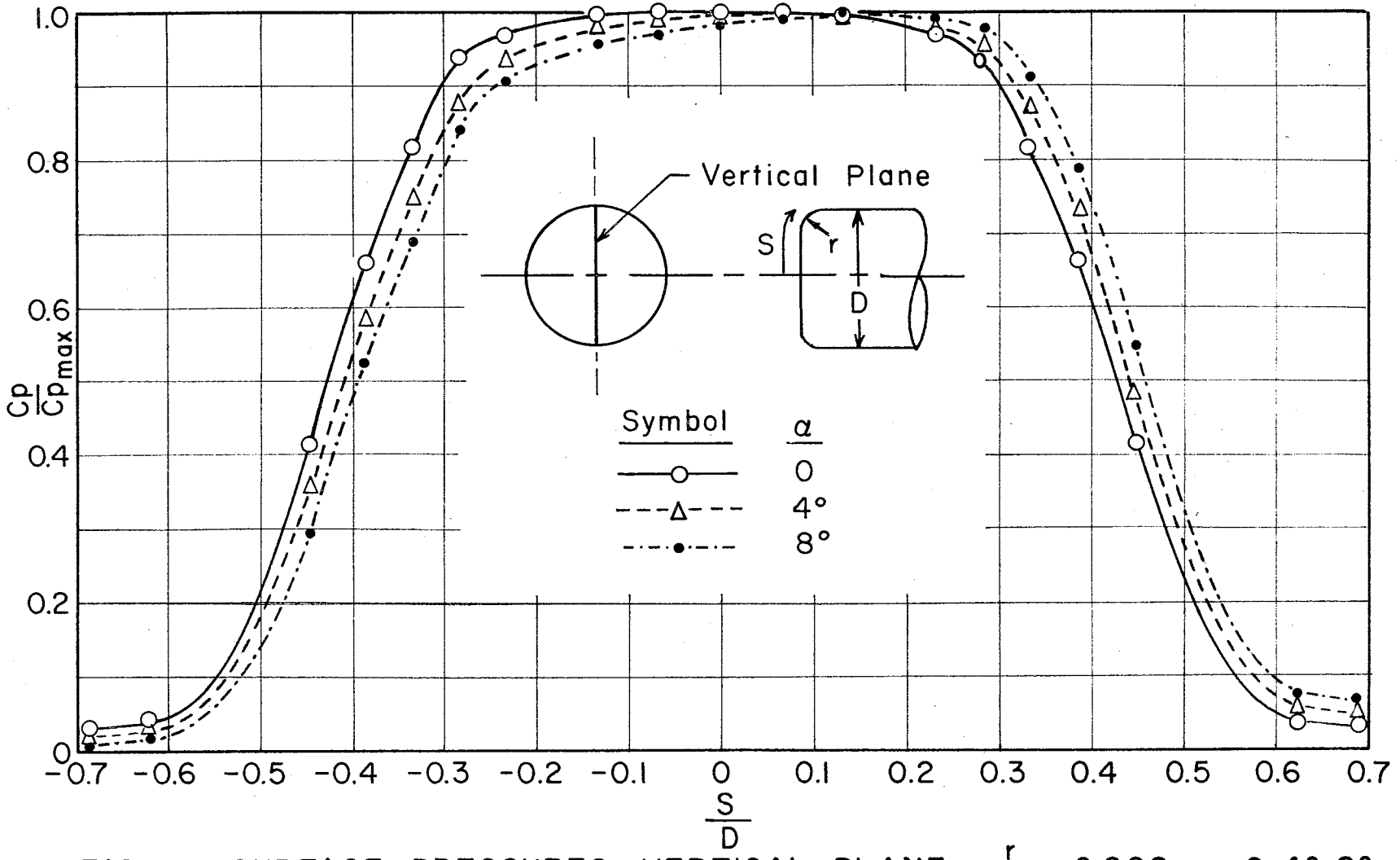

FIG. 68. SURFACE PRESSURES, VERTICAL PLANE, $\frac{r}{D} = 0.208, \alpha = 0, 4°, 8°$.

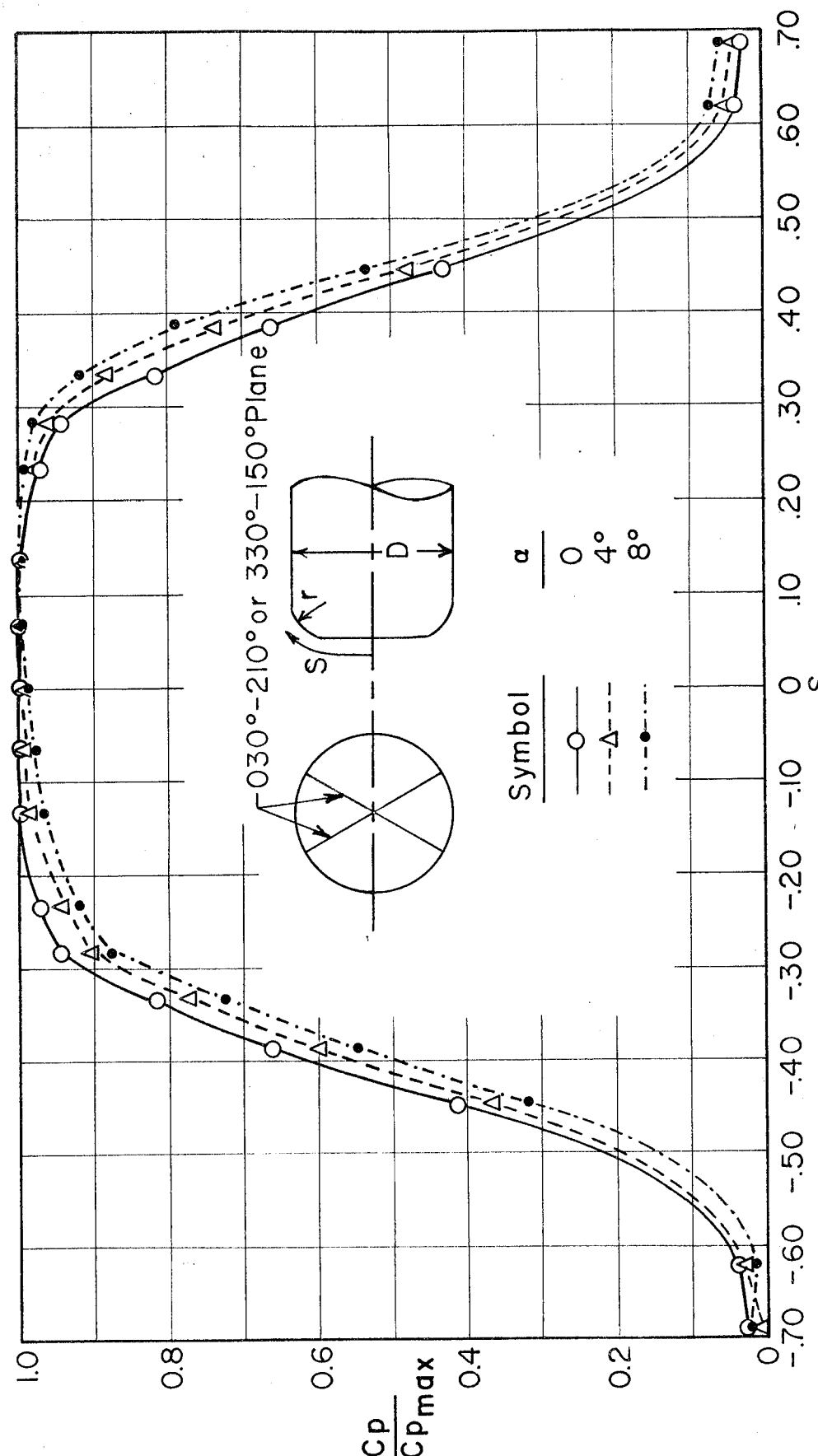

FIG.69. SURFACE PRESSURES 030°–210° PLANE, $\frac{R}{D}$, $\alpha = 0, 4°, 8°$

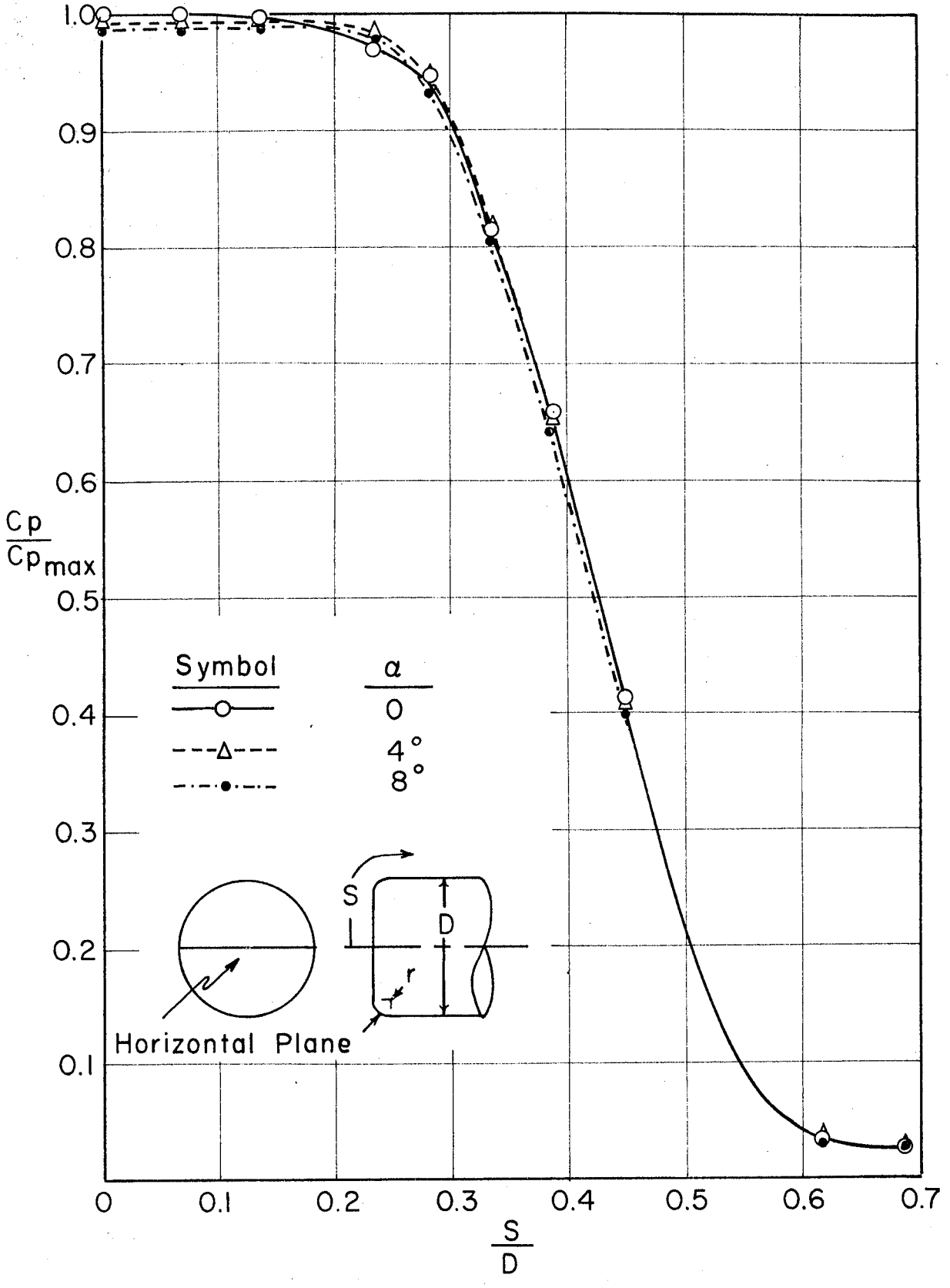

FIG. 70. SURFACE PRESSURES, HORIZONTAL PLANE, $\frac{R}{D} = \infty$, $\frac{r}{D} = 0.208$, $\alpha = 0°, 4°, 8°$.

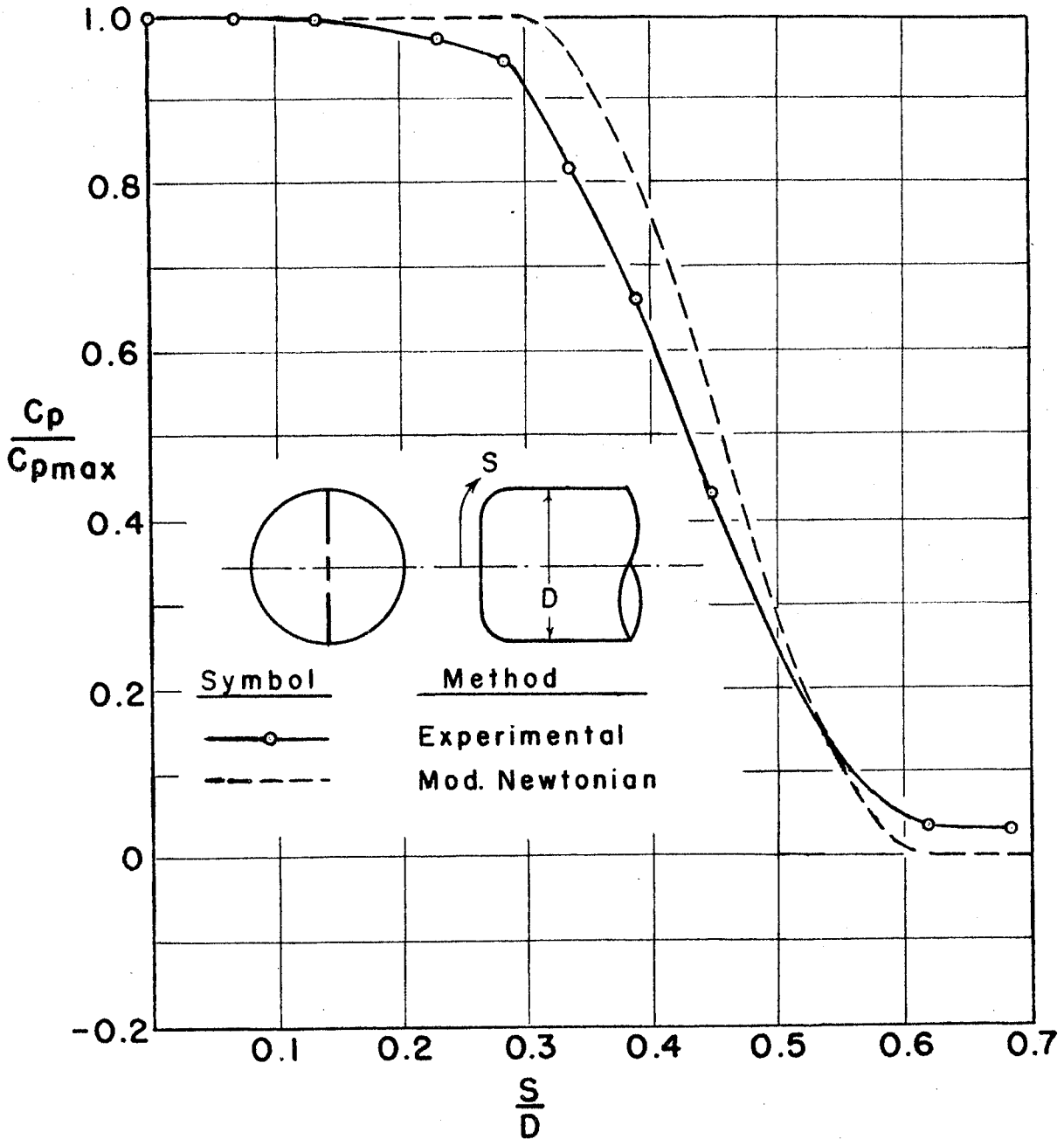

FIG. 71. COMPARISON OF EXPERIMENTAL SURFACE PRESSURE DISTRIBUTION WITH THEORETICAL APPROXIMATIONS, $r/D = 0.208$, $\alpha = 0$.

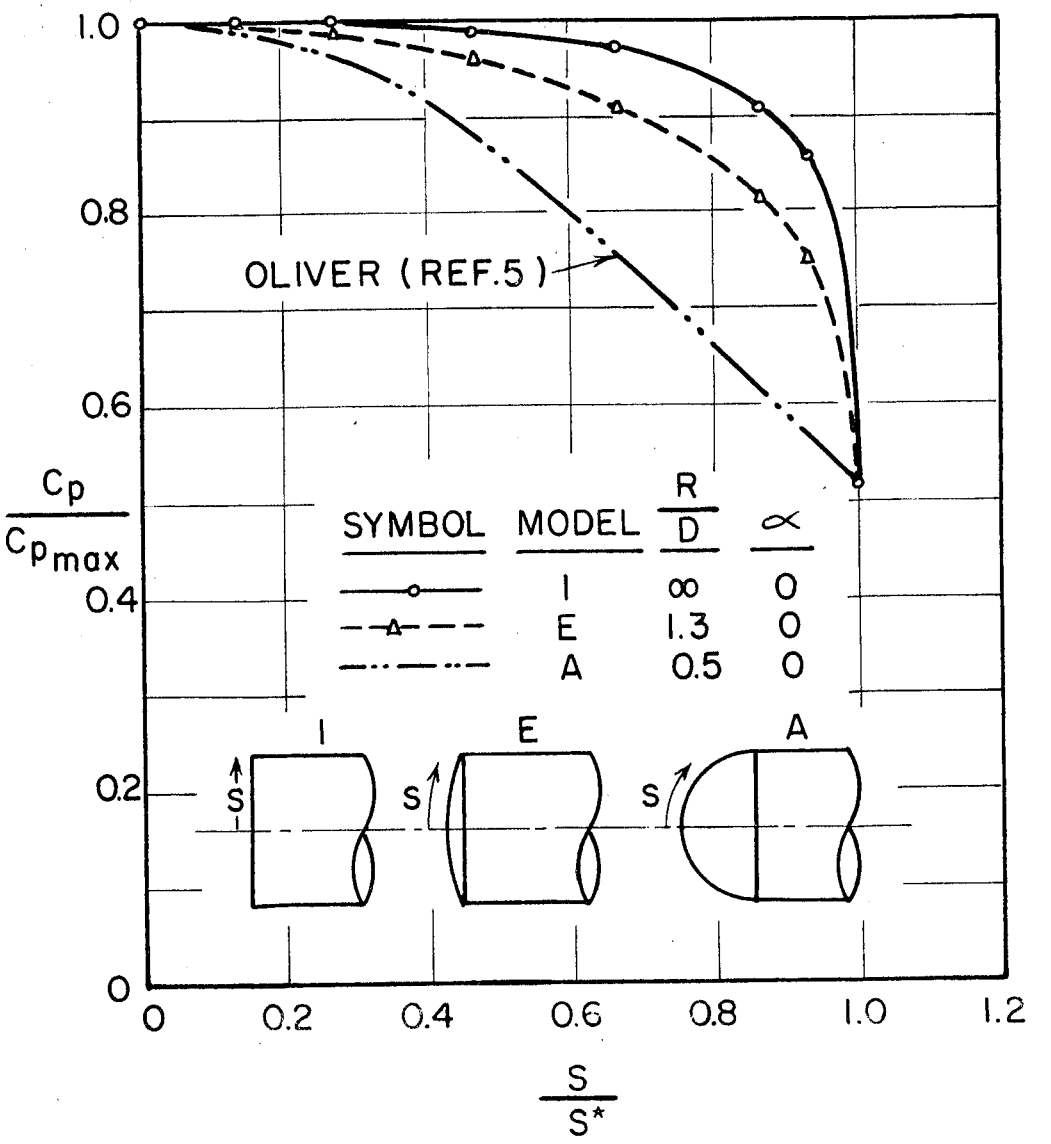

FIG. 72. COMPARISON OF SURFACE PRESSURE DISTRIBUTIONS ON SEVERAL BLUNT NOSED BODIES, M = 5.8.

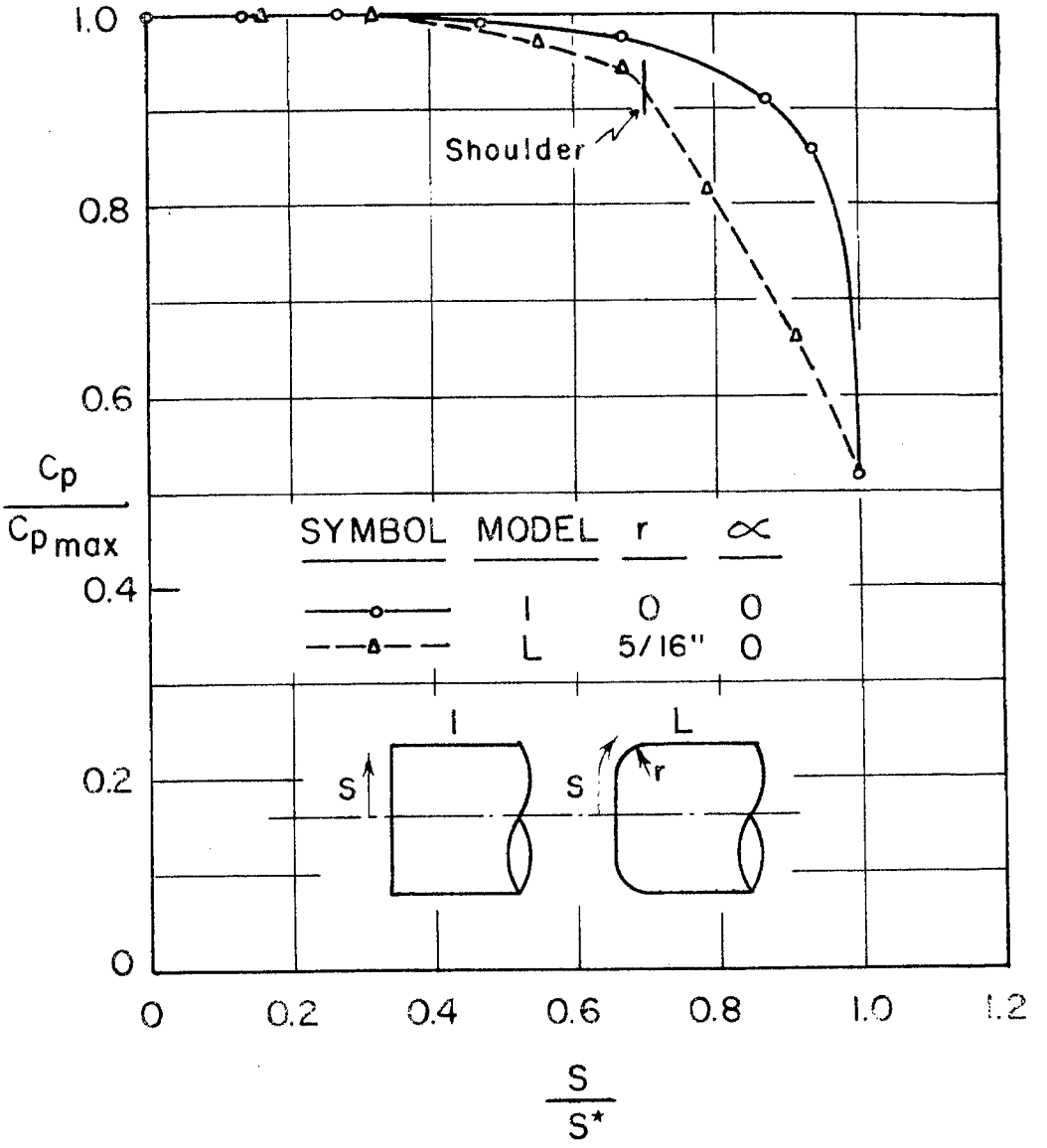

FIG. 73. COMPARISON OF SURFACE PRESSURE DISTRIBUTIONS SHOWING EFFECT OF ROUNDED SHOULDER.